A MEASUREMENT OF THE ISOVECTOR AXIAL AND STRANGE MAGNETIC FORM FACTORS OF THE NUCLEON

BY

RICHARD DARWIN HASTY

B.S., Centenary College of Louisiana, 1998

THESIS

Submitted in partial fulfillment of the requirements
for the degree of Doctor of Philosophy in Physics
in the Graduate College of the
University of Illinois at Urbana-Champaign, 2003

Urbana, Illinois

A MEASUREMENT OF THE ISOVECTOR AXIAL AND STRANGE MAGNETIC FORM FACTORS OF THE NUCLEON

Richard Darwin Hasty, Ph.D.
Department of Physics
University of Illinois at Urbana-Champaign, 2003
Douglas H. Beck, Advisor

The measurement of the parity-violating asymmetry in the scattering of electrons from the deuteron at a momentum transfer of 0.1 $(GeV/c)^2$ and average scattering angle on 145° is described in this work. It is measured to be

$$A_d = -7.74 \pm 0.71 \pm 0.60\ ppm$$

This asymmetry can be related to the isovector axial form factor of the nucleon as well as the strange quark contribution to the magnetic form factor of the nucleon. When combined with a previous measurement of the parity-violating asymmetry in the elastic scattering of electrons from protons, this measurement allows the experimental determination of the strange quark form factor,

$$G_M^s = 0.22 \pm 0.35 \pm 0.39 \pm 0.03\ n.m.$$

and the isovector axial form factor of the proton,

$$G_A^e(T=1) = 0.51 \pm 0.55 \pm 0.48 \pm 0.12\ n.m.$$

at the momentum transfer of the experiment. The updated analysis of the experiment presented here puts the measurement of $G_A^e(T=1)$ into agreement with the theoretical prediction, in contrast with a previous publication.

Acknowledgements

The knowledge, skills and effort of the entire cast of SAMPLE collaborators and MIT Bates Linear Accelerator Center staff contributed to the successful completion of the SAMPLE experiments. I was fortunate to work with this talented and dedicated group. Further, I would like to specifically acknowledge several people who played an important and positive role in my tenure as a graduate student on the SAMPLE experiment. I have greatly appreciated the guidance and support of my advisor, Doug Beck, who has been essential to my development as a physicist. The many discussions I have had with Betsy Beise have helped me to better understand the SAMPLE experiment. Takeyasu Ito made the long hours setting up the 125 MeV SAMPLE run enjoyable, and our conversations were enlightening. I also learned a great deal from Bill Franklin, Manouch Farkondeh and Genya Tsentalovich while working on the polarized source at Bates.

I would also like to thank my family and friends, who have supported me in this endeavor. My parents have encouraged my life long love of learning; without their support I could not have made it this far. The many friends I have lived with at the Brooks Co-op have broadened my experience as a graduate student. Their varied fields and interests have continuously engaged my curiosity.

This material is based on work supported by the National Science Foundation Grants PHY 04-20787 and PHY 02-44889.

Contents

List of Tables

List of Figures

Chapter 1

Theory

1.1 Introduction

One of the central aims of nuclear physics is to provide an explanation of the properties the nucleons. In the context of the standard model of particle physics, this means the development of an explanation for the properties of the nucleon in terms of quarks and gluons. Quantum chromodynamics (QCD) is thought to give the correct description of the strong force which binds the quarks into hadrons; in this theory quarks with color charge interact through gluon exchange. At high energy scales the coupling constant (α_s) for the strong force is small enough that calculations can be expanded into converging series of higher order interactions; this familiar procedure from the electroweak interactions is successful for QCD in this regime as well. However, at the lower energy scales relevant for the binding of quarks into hadrons α_s is too large for this procedure to succeed. It is an understanding of the strong force in this non-perturbative regime that needs to be developed to understand the properties of the nucleon.

A first principles approach, lattice QCD, uses numerical simulations to determine nucleon properties. However, practitioners of lattice QCD still say the technique is in its early stages and that significantly more computational power is needed to

address outstanding issues. Low energy effective theories incorporate the symmetries of QCD, but calculations in these theories require low energy constants which must be measured. Phenomenological models, often inspired by the symmetries of QCD, are also used to describe the nucleon and predict its properties. Experimental constraints on nucleon properties are needed to guide the development of all of these approaches.

In the simplest non-relativistic constituent quark model, the proton is composed of two up quarks and a down quark which do not interact strongly; this model predicts a value for the proton magnetic moment quite close to the measured value. However, evidence from deep-inelastic scattering indicates that a sea of $q\bar{q}$ pairs and gluons plays an important role in the nucleon; half of the nucleon momentum appears to be carried by the gluons, which are the source of the $q\bar{q}$ sea. This is consistent with the QCD theory of the quarks interacting strongly through the exchange of gluons. Because strange quarks are only present in the sea, measuring strange contributions to nucleon properties provides information about the sea. This is the primary reason the strange quark properties are of interest.

The determination of the strange quark contribution to the magnetic form factor (G_M^s) at low momentum transfer is the original and the ultimate goal of the SAMPLE collaboration and this work[1]. It is also appealing to estimate from this measurement the contribution of the various quark flavors to the magnetic moment of the proton (μ_p) since the measurement of μ_p was the first indication that the proton is not a fundamental particle [1] [2].

1.1.1 Strange Quark Contributions

Previous experiments have suggested a strange quark contribution to the nucleon properties. An analysis of the hyperon masses and pion–nucleon scattering data

[1]In the limit of zero momentum transfer, G_M^s is the strange quark contribution to the magnetic moment.

suggests that the strange quarks contribute to the mass of the nucleon. The idea behind the analysis is that if quarks were massless the nucleons would have still have a mass, M_0, coming from the binding energy. When quark masses are considered the nucleon mass receives contributions from the three light quarks:

$$M_N = M_0 + m_s + m_{ud} \tag{1.1}$$

where M_N is the mass of the nucleon, m_s is the contribution from the strange quark mass and m_{ud} is the contribution to the mass from the up and down quarks. The data from pion–nucleon can be related to m_{ud} by extrapolation into an off-shell region [3]. By examining the hyperon masses, the total contribution from the quark masses can be determined. The disagreement between these two analyses using only uU and d quarks is an indication of the strange quark content of the nucleon. In the analysis of reference [3], the strange content is given by

$$\frac{\langle N \mid \bar{s}s \mid N \rangle}{\langle N \mid \bar{u}u + \bar{d}d + \bar{s}s \mid N \rangle} \simeq 0.1 \tag{1.2}$$

which suggests the the strange quark contribution to the the mass is $m_s \simeq 120\ MeV$. However, recent analyses of this kind using new π–N scattering data indicate an implausibly large strange mass contribution; work continues to explain the discrepancy [4].

Polarized deep-inelastic scattering (DIS) can probe Δq, the quark spin contribution to the nucleon . The Ellis-Jaffe sum rule connects the polarized structure functions measured in polarized DIS to the spin contributions of the up and down quarks. A generalized version of the Ellis-Jaffe sum rule which includes strange sea quarks can be used to determine the sum of the strange and anti-strange contributions , $\Delta s + \Delta \bar{s} = -0.14 \pm 03$ [5]. This analysis is somewhat uncertain because it requires the use of SU(3) flavor symmetry.

The approach used in the SAMPLE experiment investigates strange effects with very little theoretical uncertainty. By comparing the neutral weak vector and elec-

tromagnetic properties of the nucleons, the contributions from each of the three light quark flavors can be determined. Because the electromagnetic properties of the nucleons have been measured previously [6], only a measurement of the weak properties of the nucleon is needed in order to determine the flavor composition of the magnetic form factor of the nucleon. Parity-violating (PV) electron scattering from the proton can be used to make this measurement [7] [8] [9]. However, the PV cross section asymmetry in $e^- - N$ scattering is also sensitive to the axial vector interaction between the electron and the nucleon; an additional measurement of the PV asymmetry in electron scattering from the deuteron is used to provide an experimental constraint for the axial form factor as well [10]. The main focus of this dissertation is the experimental determination of the PV cross section asymmetry in $e^- - d$ scattering, and its use in the determination of of G_M^s.

1.2 Formalism

This section illuminates the theoretical framework necessary for the interpretation of the experiment. The form factors used to describe the nucleons, the composition of the form factors in terms of their quark contributions and the PV $e^- - p$ asymmetry are discussed at the lowest order, or tree level, in Sections 1.2.1-1.2.3. Electroweak radiative corrections to the tree level discussion are presented in Section 1.2.4.

1.2.1 Nucleon Form Factors and Quark Currents

The SAMPLE experiment uses the electro-weak interaction to probe the structure of the nucleon with scattered electrons. The first order interactions are the exchange of either a photon (γ) or a neutral weak boson (Z), as shown in Figure 1.1. The invariant amplitudes for the two Feynman diagrams are calculated from the leptonic vector and axial currents (l^μ and $l^{\mu 5}$) and the nucleon vector and axial currents (J_μ^Z

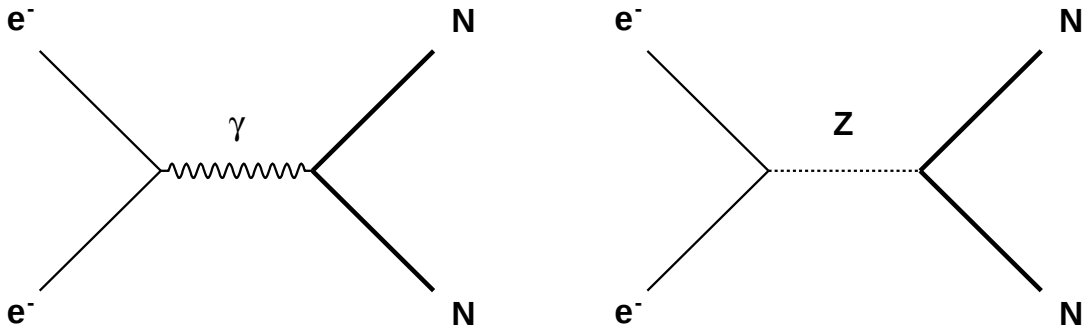

a) Photon exchange b) Neutral weak boson exchange

Figure 1.1: Tree level weak and EM Feynman diagrams in $e^- - N$ scattering: a) Photon exchange, b) Neutral weak boson exchange.

and $J^Z_{\mu 5}$):

$$\mathcal{M}_\gamma = -\frac{4\pi\alpha}{Q^2} e_i l^\mu J^\gamma_\mu \tag{1.3}$$

$$\mathcal{M}_Z = \frac{G_F}{2\sqrt{2}} \left(g^i_V l^\mu + g^i_A l^{\mu 5}\right) \left(J^Z_\mu + + J^Z_{\mu 5}\right) \tag{1.4}$$

where α is the EM coupling constant, G_F is the Fermi constant, Q^2 is the magnitude of the four-momentum transferred from the electron to the nucleon, e_i is the EM charge of the incident electron, $g^l_{V(A)}$ is the weak vector(axial) charge[2]. The charges of the fermions are given in Table 1.1. The Fermi constant is given by

$$G_F = \frac{g^2}{4\sqrt{2}\, M^2_W} \tag{1.5}$$

where g is the weak coupling and M_W is the mass of the charged weak vector boson. The leptonic currents can be written down in terms of the spinor familiar from the free particle solution of the Dirac equation, u_l, and its Hermitian conjugate $\bar{u}_l$. The vector current and axial currents are respectively given by

$$l^\mu \equiv u_l \gamma^\mu u_l \tag{1.6}$$

$$l^{\mu 5} \equiv u_l \gamma^\mu \gamma_5 u_l \tag{1.7}$$

[2]The Q^2 dependence of the Z propagator has been neglected because the rest energy of the Z is much higher than energy scales in this experiment.

Table 1.1: Fermion electromagnetic and weak charges.

The electromagnetic (e_i), weak vector (g_V^i), and weak axial (g_A^i) charges of the lighter fermions.

	e_i	g_V^i	g_A^i
e	1	$-1+4\sin^2\theta_W$	1
u	$\frac{2}{3}$	$1-\frac{8}{3}\sin^2\theta_W$	-1
d	$-\frac{1}{3}$	$-1+\frac{4}{3}\sin^2\theta_W$	1
s	$-\frac{1}{3}$	$-1+\frac{4}{3}\sin^2\theta_W$	1

In contrast to the free leptons, nucleons are composite objects which are not fully understood. Consequently, the EM and weak currents of the nucleon are described with form factors that provide a phenomenological description of the most general possible interaction. The EM interaction is a vector interaction, and the associated current is given by

$$J_\mu^\gamma = \bar{U}_N \left[F_1^\gamma(Q^2)\gamma^\mu + F_2^\gamma(Q^2)\frac{i\sigma^{\mu\nu}q_\nu}{2M} \right] U_N \tag{1.8}$$

where U_N is the nucleon spinor, $F_{1(2)}^\gamma$ is the Dirac(Pauli) form factor[3], and M is the mass of the nucleon. The Sachs form factors, which are linear combinations of the Dirac and Pauli form factors, provide a more intuitive description of the nucleon in terms of an electric and a magnetic form factor:

$$G_E^\gamma(Q^2) = F_1^\gamma(Q^2) + F_2^\gamma(Q^2) \tag{1.9}$$

$$G_M^\gamma(Q^2) = F_1^\gamma(Q^2) - \tau F_2^\gamma(Q^2) \tag{1.10}$$

$$\tau = \frac{Q^2}{4M} \tag{1.11}$$

In the Breit frame, $G_E^\gamma(Q^2)$ is the Fourier transform of the charge distribution and $G_M^\gamma(Q^2)$ is the Fourier transform of the momentum distribution. In the limit of zero

[3] All the form factors discussed in this work have a dependence on Q^2. This dependence is omitted except where necessary for clarity.

momentum transfer, the Sachs form factors give the electric charge and magnetic moment of the nucleon,

$$G_E^{\gamma,N}(Q^2 \to 0) = e_N \tag{1.12}$$

$$G_M^{\gamma,N}(Q^2 \to 0) = \mu_N \tag{1.13}$$

where N represents the nucleon (p for the proton or n for the neutron), e_N is the electric charge of the nucleon and μ_N is its magnetic moment.

The neutral weak current has both a vector component and an axial component. The vector component is similar the EM current:

$$J_\mu^Z = \bar{U}_N \left[F_1^Z \gamma^\mu + F_2^Z \frac{i\sigma^{\mu\nu} q_\nu}{2M_N} \right] U_N \tag{1.14}$$

where F_1^Z and F_1^Z are the Dirac and Pauli form factors for the weak vector interaction. The vector weak form factors can also be arranged into Sachs form factors, completely analogous to the EM form factors:

$$G_E^Z = F_1^Z + F_2^Z \tag{1.15}$$

$$G_M^Z = F_1^Z - \tau F_2^Z \tag{1.16}$$

The description of axial component of the weak interaction requires another form factor, the neutral weak axial form factor. The axial current is given by:

$$J_{\mu 5}^Z = \bar{U}_N G_A^e \gamma^\mu \gamma^5 U_N \tag{1.17}$$

where G_A^e is the neutral weak axial form factor.

Because the neutral weak boson can have both vector and axial vector interactions, the amplitude for Z exchange has a parity-violating (PV) component. A quantity that is parity conserving remains the same under spatial inversion. Vectors change sign under spatial inversion, while axial vectors remain the same under spatial inversion.

The Z amplitude can also be separated into parity-conserving (PC) and PV parts. The parity violation in the weak interaction is important for the observation of the

weak form factors described in Section 1.2.3. A PC quantity remains the same under spatial inversion. The PV terms of $\mathcal{M}_Z$ have vectors multiplied with axial vectors,

$$\mathcal{M}_Z^{PV} = \frac{G_F}{2\sqrt{2}} \left(g_V^i l^\mu J_{\mu 5}^Z + g_A^i l^{\mu 5} J_\mu^Z \right) \tag{1.18}$$

while the PC terms purely vector or purely axial vector,

$$\mathcal{M}_Z^{PC} = \frac{G_F}{2\sqrt{2}} \left(g_V^i l^\mu J_\mu^Z + g_A^i l^{\mu 5} J_{\mu 5}^Z \right) \tag{1.19}$$

1.2.2 Quark Components

The nucleons are composed of quarks, and because the electroweak interaction with quarks is point-like, the properties of the nucleons (both the general currents and the form factors introduced above) can be written down as linear combinations of contributions from the individual quarks. The current operators can be expressed as sums of quark currents [11]

$$\hat{J}_\mu^\gamma = \sum_q e_q u_l \gamma^\mu u_l \tag{1.20}$$

$$\hat{J}_\mu^Z = \sum_q g_V^q u_l \gamma^\mu u_l \tag{1.21}$$

$$\hat{J}_{\mu 5}^Z = \sum_q g_A^q u_l \gamma^\mu \gamma^5 u_l \tag{1.22}$$

The sums are taken only over the light quarks lightest three quarks, u, d and s. The EM and weak nucleon currents can then be written in terms of the quark current operators as:

$$J_\mu^\gamma = \sum_q e_q \langle N | u_l \gamma^\mu u_l | N \rangle \tag{1.23}$$

$$J_\mu^Z = \sum_q g_V^q \langle N | u_l \gamma^\mu u_l | N \rangle \tag{1.24}$$

$$J_{\mu 5}^Z = \sum_q g_A^q \langle N | u_l \gamma^\mu \gamma^5 u_l | N \rangle \tag{1.25}$$

The EM and weak vector currents are different linear combinations of the same quark contributions to the nucleon current. Consequently, when the nucleon form factors

are expressed as linear combinations of the quark components, the EM and weak vector form factors of the nucleon are different linear combinations of the same quark components:

$$G_{E(M)}^{\gamma,N} = \sum_q e_q G_{E(M)}^{q,N} \tag{1.26}$$

$$G_{E(M)}^{Z,N} = \sum_q g_V^q G_{E(M)}^{q,N} \tag{1.27}$$

$$G_A^{Z,N} = \sum_q g_A^q G_A^{q,N} \tag{1.28}$$

where $G_{E(M)}^{q,N}$ is the contribution of quark q to the electric (magnetic) form factor of the nucleon and $G_A^{q,N}$ is the contribution of quark q to the neutral weak axial form factor. The quark form factors include the net contribution of both the quarks and the anti-quarks. For example, if the distributions of s and $\bar{s}$ quarks were identical in the proton their contributions to the proton electric form factor would have the same magnitude but opposite sign. In this situation $G_E^{s,p}$ would be zero.

Charge symmetry relates the quark form factors of the neutron to those of the proton, allowing the determination of of the quark form factors from the values of $G_{E(M)}^{\gamma,p}$,$G_{E(M)}^{\gamma,n}$ and $G_{E(M)}^{Z,p}$. Under charge symmetry, the u quark form factors in the neutron are the same as the d quark from factors in the proton. Similarly, the d quarks in the neutron are taken to have the same distribution as the u quarks in the proton. The strange quarks are taken to behave identically on both the proton and the neutron. Charge symmetry is broken by the differences in the EM interactions and masses of the up and down quarks, but the effect of the symmetry breaking on the extraction of nucleon form factors is negligible compared to the experimental uncertainties in this work [12]. Using charge symmetry, the quark form factors are defined in terms of the proton quark form factors:

$$
\begin{aligned}
G^{u}_{E(M)} &\equiv G^{u,p}_{E(M)} = G^{d,n}_{E(M)} \\
G^{d}_{E(M)} &\equiv G^{d,p}_{E(M)} = G^{u,n}_{E(M)} \\
G^{s}_{E(M)} &\equiv G^{s,p}_{E(M)} = G^{u,n}_{E(M)}
\end{aligned}
$$

With these definitions, the vector quark form factors can be determined from the EM and weak vector form factors of the nucleons:

$$G^{u}_{E(M)} = (3 - 4\sin^2\theta_W)G^{\gamma,p}_{E(M)} + G^{Z,p}_{E(M)} \tag{1.29}$$

$$G^{d}_{E(M)} = (2 - 4\sin^2\theta_W)G^{\gamma,p}_{E(M)} + G^{\gamma,n}_{E(M)} - G^{Z,p}_{E(M)} \tag{1.30}$$

$$G^{s}_{E(M)} = (1 - 4\sin^2\theta_W)G^{\gamma,p}_{E(M)} - G^{\gamma,n}_{E(M)} - G^{Z,p}_{E(M)} \tag{1.31}$$

Because the EM form factors have been measured previously, only a measurement of $G^{Z,p}_{M}$ is needed to determine the strange quark contribution to the proton magnetic form factor, G^{s}_{M} (to which this experiment is most sensitive).

As with the vector form factors, the axial vector quark form factors for the nucleon are defined in terms of the proton's quark form factors:

$$
\begin{aligned}
G^{u}_{A} &\equiv G^{u,p}_{A} = G^{d,n}_{A} \\
G^{d}_{A} &\equiv G^{d,p}_{A} = G^{u,n}_{A} \\
G^{s}_{A} &\equiv G^{s,p}_{A} = G^{u,n}_{A}
\end{aligned}
$$

Isospin symmetry allows for the axial nucleon form factors to be written in terms of isovector and isoscalar components. In terms of individual quark form factors, the nucleon form factor are given by:

$$G^{e,p}_{A} = -(G^{u}_{A} - G^{d}_{A}) + G^{s}_{A} \tag{1.32}$$

$$G^{e,n}_{A} = (G^{u}_{A} - G^{d}_{A}) + G^{s}_{A} \tag{1.33}$$

The isovector component, $G_A^u - G_A^d$, changes between the proton and the neutron isospin states, while the isoscalar component remains the same. With this identification, the axial form factor can be written in terms of the isospin state of the nucleon,

$$G_A^e = -G_A\tau_3 + G_A^s \tag{1.34}$$

where $G_A \equiv G_A^u - G_A^d$, and τ_3 is 1(-1) for the proton (neutron). The isoscalar term can be determined through deep inelastic scattering, and the isovector term can be measured with hyperon beta decay. However, the higher order electroweak corrections to G_A for electron scattering are considerable. It is the uncertainty in the electroweak corrections to G_A that make the experimental determination of G_A desirable.

1.2.3 The PV Asymmetry in Elastic $e^- - N$ Scattering

Because the EM interaction is much stronger than the weak interaction, the neutral weak form factor is difficult to observe. It is the PV nature of the weak interaction that allows it to be seen against the PC electromagnetic interaction. Further, the PV weak amplitude is enhanced through interference with the PC electromagnetic amplitude, putting the weak effects in a practically observable range. The PV asymmetry in the scattering longitudinally polarized electrons from unpolarized nucleons is sensitive to the neutral weak vector form factor [13],[14] and[15].

The PV weak interaction is revealed by comparing an experiment with its mirror image. In PV electron scattering, the cross section for electrons with positive helicity is compared with that for negative helicity electrons. The helicity of the electrons is given by the dot product of the spin direction ($\hat{s}$) with the momentum direction($\hat{k}$):

$$h \equiv \vec{s} \cdot \vec{k} \tag{1.35}$$

When the spin is along the direction of the beam the helicity is plus one. When the polarization is in the opposite direction of the momentum the helicity is minus

one. Because the spin is an axial vector and the momentum is a vector, the parity operator takes the positive helicity state to the negative helicity state (helicity being a pseudoscaler quantity), and comparing the positive and negative helicity cross section is comparing an experiment with its mirror image.

The comparison is done using the cross section asymmetry for longitudinally polarized electrons, defined by:

$$A \equiv \frac{\sigma^+ - \sigma^-}{\sigma^+ + \sigma^-} \tag{1.36}$$

where $\sigma^{+(-)}$ is the cross section for positive(negative) helicity electrons scattered from a nucleon. Because the cross section is proportional to the square of the summed invariant amplitudes, $\sigma^{+(-)}$ can be replaced by $\left|\mathcal{M}_\gamma^{+(-)} + \mathcal{M}_Z^{+(-)}\right|^2$. Only the PV part of $\mathcal{M}_Z$ changes for the different helicity states, therefore the asymmetry can be written

$$A = \frac{\left|\mathcal{M}_\gamma + \mathcal{M}_Z^{PC} + \mathcal{M}_Z^{PV}\right|^2 - \left|\mathcal{M}_\gamma + \mathcal{M}_Z^{PC} - \mathcal{M}_Z^{PV}\right|^2}{\left|\mathcal{M}_\gamma + \mathcal{M}_Z^{PC} + \mathcal{M}_Z^{PV}\right|^2 - \left|\mathcal{M}_\gamma + \mathcal{M}_Z^{PC} - \mathcal{M}_Z^{PV}\right|^2} \tag{1.37}$$

$$A \approx \frac{2\mathcal{M}_\gamma^* \mathcal{M}_Z^{PV}}{\left|\mathcal{M}_\gamma\right|^2} \tag{1.38}$$

Written in terms of the nucleon from factors, the asymmetry is given by

$$A = \left(\frac{G_F Q^2}{4\sqrt{2}\,\pi\alpha}\right) \frac{\epsilon G_E^\gamma G_E^Z + \tau G_M^\gamma G_M^Z - (1 - 4\sin^2\theta_W)\epsilon\prime G_M^\gamma G_A^e}{\epsilon (G_E^\gamma)^2 + \tau (G_M^\gamma)^2} \tag{1.39}$$

where the kinematic factors ϵ and ϵ' are given by

$$\epsilon = \frac{1}{1 + 2(1+\tau)\tan^2\frac{\theta}{2}} \tag{1.40}$$

$$\epsilon' = \sqrt{\tau(1+\tau)(1-\epsilon^2)} \tag{1.41}$$

The kinematic factors give a different angular dependence to the form factor combinations. As the scattering angle approaches 180° the dependence on the electric form factors vanishes. By measuring the asymmetry for backward scattered electrons, the SAMPLE experiment is only sensitive to the magnetic and axial form factors. Ideally a measurement of the PV asymmetry in polarized electron scattering from both proton and neutron targets could be used to constrain both G_M^s and G_A^e. However, free

neutron targets are not practical. Quasi-elastic scattering from the deuteron is used to provide a constraint on a different linear combination of G_M^s and G_A^e. Section 1.5 discusses the determination of single nucleon form factors from quasi-elastic $e^- - d$ scattering.

1.2.4 Radiative Corrections

The form factors and asymmetries developed above include only the tree level, or first order, diagrams shown in Figure 1.1. The contributions from additional diagrams must also be considered. These contributions to the weak form factors can be broken down into two broad categories: those that can be calculated within the electroweak theory and those that involve strong interactions. The purely electroweak corrections can be calculated with little uncertainty, while the corrections involving the strong interaction are more uncertain.

The corrections that can be calculated with only the electroweak theory involve only one quark in the target. These corrections will be called "one-quark" corrections. The one-quark corrections are independent of the target and can be thought of as renormalizations of the current operators in equations 1.26-1.28. Examples of diagrams contributing to the one-quark corrections are shown in Figure 1.2.

In contrast, the corrections involving the strong force come from diagrams where photon or Z interact with several quarks. These "many-quark" corrections are target specific and modify the hadronic matrix elements. These corrections are more difficult to calculate; they must be addressed with phenomenological models that bring considerable uncertainty. Examples of diagrams included used in calculating the many quark corrections are shown in Figure 1.3.

When the electroweak radiative corrections are taken into account, the weak vector

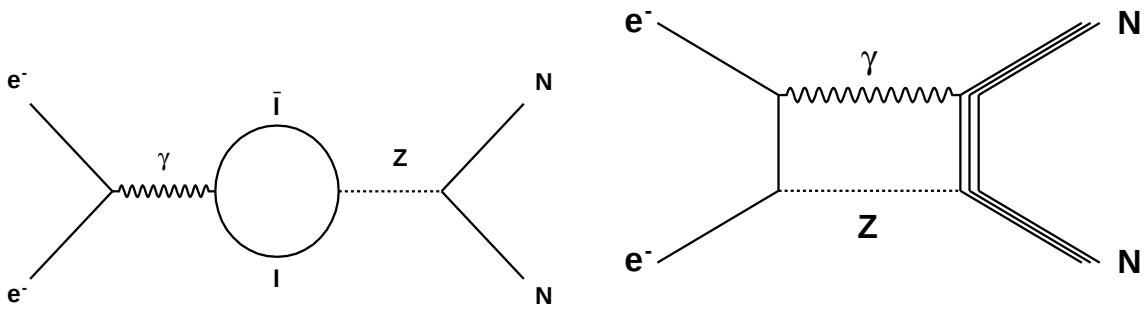

a) b)

Figure 1.2: Examples of Feynman diagrams representing "one-quark" radiative corrections. a) Vacuum polarization, which is a one-quark diagram when l represents a lepton. b) $\gamma - Z$ box diagram.

form factors are given by:

$$G^{z,p}_{E(M)} = (1-4\sin^2\theta_W)(1+R^p_V)G^{\gamma,p}_{E(M)} - (1+R^n_V)G^{\gamma,n}_{E(M)} \quad (1.42)$$
$$-(1+R^{(0)}_V)G^{s,p}_{E(M)}$$

$$G^{z,n}_{E(M)} = -(1+R^p_V)G^{\gamma,p}_{E(M)} + (1-4\sin^2\theta_W)(1+R^n_V)G^{\gamma,n}_{E(M)} \quad (1.43)$$
$$-(1+R^{(0)}_V)G^{s,p}_{E(M)}$$

$$G^e_A = -(1+R^1_A)G_A\tau_3 + R^0_A + (1+R^{(0)}_A)G^s_A \quad (1.44)$$

where R^p_V, R^n_V and $R^{(0)}_V$ are the corrections to the vector form factors; and R^1_A, R^0_A and $R^{(0)}_A$ are the axial vector corrections. The vector corrections were calculated by Marciano and Rosner in reference [16] and translated into the $\bar{M}S$ scheme by Musolf *et al.*[11]. The axial corrections have also been calculated, but they are larger and more uncertain; these are discussed further in Section 1.3. In addition, there are small corrections which come from ignoring the heavier quarks; these corrections are much smaller than the one-quark and many-quark corrections [17]. The corrections are listed in Table 1.2.

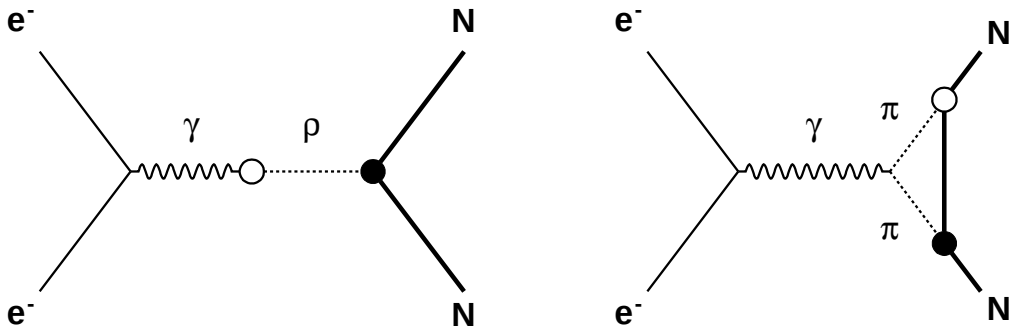

a) b)

Figure 1.3: Examples of Feynman diagrams representing "many-quark" radiative corrections. The filled circles represents an axial couplings and the unfilled circles represents a vector coupling. a) Rho meson pole b) Pion loop

Table 1.2: Electroweak radiative corrections.

The corrections to the vector and axial vector weak form factors are split into one-quark and many-quark contributions. The vector nucleon corrections R_V^N are in the $\bar{M}S$ renormalization scheme [11]. The axial vector corrections were calculated in reference [18], and cast into the $\bar{M}S$ scheme in reference [19]. Calculations for $R_{V,A}^{(0)}$ are not available; these corrections are absorbed into the reported values of $G_A^e(T=1)$ and G_M^s.

	one-quark	many-quark	heavy-quark	total
R_V^p	-0.054	± 0.033	$< 10^{-4}$	0.054 ± 0.033
R_V^n	-0.0143	± 0.0004	$< 10^{-4}$	-0.0143 ± 0.0004
R_A^1	-0.187	-0.04 ± 0.24		-0.227 ± 0.24
R_A^0	0.072	0.01 ± 0.14	0.02	$-.102 \pm 0.14$

1.3 The Axial Form Factor

While axial matrix elements can be determined experimentally in other experiments, the axial form factor seen in $e^- - N$ scattering is subject to corrections not present in these methods. In addition, the tree level contribution to the axial form factor seen in PV electron scattering is suppressed. The corrections unique to $e^- - N$ scattering and the suppression of the tree level interaction make the experimental determination of G_A^e desirable for the determination of G_M^s. The axial correction is also interesting in that it can be related to the anapole moment (AM) of the nucleon [18].

Typically, electroweak radiative corrections are expected to be $\mathcal{O}(\alpha)$, but the suppression of the tree level interaction in PV $e^- - N$ scattering makes the correction to the axial form factor much more significant. In order for the interaction depicted in Figure 1.1b to violate parity, one coupling to the Z must be axial vector and the other must be vector. When contributions to the from the axial form factor of the nucleon are considered, the weak coupling to the electron must be vector. The vector coupling to the electron is small, ($g_V^e = 1 - 4\sin^2\theta_W$). Higher order diagrams do not necessarily contain the small vector weak coupling of the electron, therefore their contributions can be large compared to the tree level.

The many-quark corrections to G_A^e discussed in the previous section include contributions from the nucleon anapole moment (AM). An anapole moment involves an effective PV coupling of a photon. The AM was first described by Zeldovich [20]. An AM can be generated classically by a solenoid bent into a toroidal shape. Because the magnetic field generated by a current in a toroidal solenoid winding is confined to the interior of the toroid, a torque can be generated only by current which passes through the toroid. As might be expected from this classical model, the AM vanishes for real photons.

The nucleon anapole moment can be seen as analogous to the anapole moment of the nucleus, observed by Wood *et al.* in Cesium [21]. The nuclear AM comes from the

PV interactions of nucleons, while the AM of a nucleon comes from PV interactions between quarks. These PV interactions between nucleons generate a longitudinal component to the nucleon spin, and this moving dipole component can generate the solenoidal field described by Zeldovich [22]. Analogous interactions between quarks can generate the nucleon anapole moment. Flambaum and Khriplovich first realized that the AM of a large nucleus might be observable [23]; they observed that the nuclear AM grows as $A^{\frac{2}{3}}$ while the parity violation from the $\gamma - Z$ interference stays roughly constant. In large nuclei like Cesium, the AM can grow large enough to dominate over the $\gamma - Z$ interference.

The one-quark and many-quark corrections to G_A^e have been calculated by Zhu *et al.* [18]. They calculate both isovector and isoscalar corrections. The one-quark corrections contain diagrams like the ones shown in Figure 1.2. The many quark corrections are calculated in terms of the nucleon AM. The anapole interaction is given by

$$\mathcal{L}^{AM} = \frac{e}{\Lambda_\chi^2}\bar{N}(a_s + a_v\tau_3)\gamma_\mu\gamma_5 N\partial_\nu F^{\nu\mu} \tag{1.45}$$

where Λ_χ^2 gives the scale of chiral symmetry breaking, a_s represents isoscalar contributions and a_v represents isovector contributions. The calculations of the diagrams contributing to $a_{s,v}$ are done in heavy baryon chiral perturbation theory. The calculations depends on the PV hadronic couplings of the theory, which must be determined experimentally; the large uncertainty in the axial corrections reflects uncertainty in the determining the couplings. In addition, diagrams with excited intermediate nucleon states — which are not included in the calculation of reference [18] — might have significant contributions (e.g. the diagram in Figure 1.3b when the intermediate state is not a ground state nucleon). The uncertainty in the axial corrections is large enough that the experimental determination of the axial form factor is desirable.

The calculation by Zhu *et al.* is for the anapole moment, i.e. at zero momentum transfer. In order to compare the corrections to G_A^e with experiment, they must be

evolved to the momentum transfer of the experiment. Particularly in the case of the anapole contributions, where the interaction is a contact interaction, deviation from the dipole form factor might be expected. The Q^2 evolution of the anapole contributions has been examined by Maekewa *et al.* in chiral perturbation theory to next to leading order [24]. For the natural ranges of the coupling constants, a change of approximately twenty percent is found for the momentum transfer at the SAMPLE experiment. This change is small compared to the theoretical uncertainty in the anapole contributions.

1.4 Model Predictions of μ_s

The predictions of the strange quark contribution to the magnetic form factor generally rely on phenomenological models of the nucleon. While chiral perturbation theory, a low energy effective field theory of QCD, can be used to approach the calculation of strange matrix elements, the coupling constants for the effective fields cannot be calculated without resorting to models. Most predictions are made in the limit of zero momentum transfer, while the experiment must be done at finite momentum transfer. While the momentum transfer dependence of G_M^s is not precisely known, the uncertainty in the extrapolation needed to compare the two appears to be small compared to the uncertainty in the current measurement of G_M^s. This extrapolation is discussed with the results in Section 4.2.

1.4.1 Kaon Loops

Conceptually the simplest, the kaon loop models are based on the fluctuations of the nucleon to a strange meson and baryon. For example, the proton (quark content uud) can fluctuate to a Λ (uds) and a $K(u\bar{s})$. In the classical analogy, the lighter charged kaon will orbit farther from the common center of mass of the system, leading to a

net contribution to the strange magnetic moment. Several models of the nucleons have been used in kaon loop calculations.

Koepf, Henley and Pollock used two different nucleon models to calculate the contributions of the kaon loops [25]. They used a cloudy bag model and a non-relativistic constituent quark model. The cloudy bag model (CBM) takes the nucleon to be three light quarks confined in a bag and surrounded by a cloud of mesons. The size of the bag is determined by ratios of the charge radii and magnetic moments of the nucleons, and determines the nucleon form factor used in calculating μ_s. The non-relativistic constituent quark model takes the nucleon to be three "heavy" quarks (each with mass $\frac{1}{3}M_N$), and has a characteristic length determined the same way as the bag size in the CBM. The resulting form factors are nearly identical, leading to very similar predictions of $\mu_s \simeq 0.03$ n.m..

Other kaon loop models use different models. Musolf and Burkardt based their nucleon model on the baryon-baryon scattering and quark model estimates [26]; their prediction for μ_s is a factor of ten larger than the CBM prediction. In contrast with the previous kaon loop calculation, they did not adjust the parameters of their model to reproduce the nucleon's EM form factors. In addition, they include "seagull" diagrams needed to preserve the Ward-Takashi identities, which are a generalized version of current conservation. Their work was later revisited with an updated nucleon model [27], though the resulting prediction for μ_s was not greatly changed. Geiger and Isgur include the contributions from all of the OZI-allowed strange baryon and meson states [28]. A simple quark model is used for the excited states. Geiger and Isgur calculate a value of μ_s similar to that in reference [25], but they note that the small value results from cancellations of large contributions.

1.4.2 Vector Dominance

The vector dominance models calculate the strange quarks effects under the assumption that the coupling to isoscalar mesons dominates over the bare photon coupling. The vector mesons are composed of slightly mixed strange and non-strange base states

$$\begin{aligned} \mid \omega\rangle &= \cos\eta\frac{1}{2}\left(\mid \bar{u}u\rangle + \mid \bar{d}d\rangle\right) - \sin\eta \mid \bar{s}s\rangle \\ \mid \phi\rangle &= \sin\eta\frac{1}{2}\left(\mid \bar{u}u\rangle + \mid \bar{d}d\rangle\right) + \cos\eta \mid \bar{s}s\rangle \end{aligned}$$

where the mixing between the strange and non-strange states is small ($\eta = 0.053 \pm .005$ [29]). Dispersion analysis is then used to determine the isoscalar form factor of the nucleon. The isoscalar Dirac and Pauli form factors $F_i^{T=0} \equiv (F_i^p + F_i^n)$ are given by fitting the experimental data to a linear combination of some number of (mono-)poles. At least two such poles are required to reproduce the dipole description of the nucleon form factors; these two poles are identified as the ϕ and ω meson poles. Additional poles can be included to improve the fit. However, constraints from the high momentum transfer limits of the form factors are needed to calculate strange quark matrix elements when additional poles are used in the fit.

Calculations using this method differ in the number of poles used to fit the experimental data and the assumptions about the asymptotic behavior of the form factors. Jaffe used a three pole fit and assumed that F_1 vanishes as $1/Q^2$ and F_2 vanishes as $1/Q^4$ [30]. Mergell, Hammer, Meissner and Drechsel used the same approach as Jaffe, but included more recent data in their three pole fit [31][32]. In addition, they took the large momentum transfer limits from perturbative QCD. Forkel implemented three, four and and six pole fits to meet different possible constraints from QCD [33]. Musolf and Ito used only the ϕ and ω poles in their fit; they argue that the inclusion of additional poles is necessary only to describe the high momentum transfer behavior and is not as important for determining the low momentum transfer properties. With the exception of the last prediction, all of the poles models give values of μ_s between

-0.3 and -0.1 n.m..

1.4.3 Lattice QCD

As its name suggests, lattice QCD implements the rules of QCD on a lattice of points in space time. While this approach proceeds from first principles, it is not possible to implement all of the necessary physical processes. In particular, the lattice QCD equivalent of including $q\bar{q}$ loops in Feynman diagrams is too computationally expensive. As a consequence, the lattice QCD calculations are without these loops (i.e. in the quenched approximation). Dong, Liu and Williams have made a quenched lattice QCD calculation [34].

Additional approaches have been inspired by lattice QCD. Leinwiber and Thomas have made the most current prediction in a technique called QCD equalities [35]. This technique develops sum rules based on the symmetries of lattice QCD which relate the octet-baryon magnetic moments to individual flavor contributions. Lewis, Wilcox and Woloshyn combine chiral perturbation theory with lattice QCD [36]. Chiral perturbation theory is a low energy effective field theory of QCD. It exploits the chiral symmetry present in QCD in the limit of massless quarks. However, as indicated earlier, there are coupling constants in the theory that must in general be determined from independent experiments. Lewis, Wilcox and Woloshyn used a quenched lattice QCD calculation to estimate these low energy coupling constants and make a prediction for G_M^s at finite momentum transfer.

1.4.4 Summary

The calculations of the strange contribution to the magnetic moment lie between -0.5 μ_N and 0.5 μ_N. For the most part, the authors do not make ambitious claims for their predictions, citing neglected contributions and other difficulties. For example, Geiger and Isgur state that cancellations in relatively large individual contributions

from the intermediate states are responsible for their small prediction; therefore they note that contributions from the OZI-suppressed states they did not consider could be significant. In the vector dominance models, uncertainty in the appropriate limits of the high momentum transfer behavior contributes to the difficulty of making a solid prediction. Results from the calculations discussed above and from additional approaches not discussed here are listed in Table 1.3.

1.5 The Parity-Violating Asymmetry in Quasi-elastic $e^- - d$ Scattering

Quasi-elastic(QE) scattering from the deuteron can be used to provide the additional constraint needed to determine both the weak vector magnetic and axial form factors. In the static approximation, the QE PV asymmetry from the deuteron is given by

$$A_{QE} \approx \frac{\sigma_p A_p + \sigma_n A_n}{\sigma_n + \sigma_p} \tag{1.46}$$

where $\sigma_p(n)$ is the cross section for elastic scattering form the proton(neutron) and $A_{p(n)}$ is the PV asymmetry in polarized electron proton(nucleon) scattering. This approximation must be corrected for final state interactions between the nucleons. In addition, there is a small elastic scattering cross section from the deuteron. When the final state interactions and elastic scattering are taken into account, the PV asymmetry in scattering from the deuteron becomes

$$A_d = \frac{A_{QE}\sigma_{QE} + A_E\sigma_E}{\sigma_{QE} + \sigma_E} \tag{1.47}$$

where A_{QE} and σ_{QE} are the asymmetry and cross section for QE scattering of the electron from the deuteron and A_E and σ_E are the asymmetry and cross section for elastic scattering from the deuteron. The correction for final state interactions is small, and can be made with little uncertainty.

Table 1.3: Predictions of μ_s.

Predictions of the net strange quark contribution to the magnetic form factor of the nucleons. With the exception of the QCD and chiral perturbation theory prediction by Lewis, Wilcox and Woloshown — which is for the same momentum transfer as the SAMPLE experiment — the predictions of G_M^s are for the limit $Q^2 \to 0$.

Model	μ_s (n.m.)
Loops (cloudy bag) [25]	-0.0260
Loops (constituent quark) [25]	-0.0324
Loops [26]	-0.31 $\to$ -0.40
Loops [27]	-0.25
Loops [37]	0.010
Loops [28]	0.035
Poles (3) [30]	-0.24 $\to$ -0.41
Poles (3) [31]	-0.24 $\pm$ 0.03
Poles (2) [27]	1.85 $\pm$ 2.2
Poles (3) [33]	-0.26
Poles (4) [33]	-0.18
Poles (6) [33]	-0.114
Lattice QCD [34]	-0.36 $\pm$ 0.20
QCD Equalities [35]	-0.16 $\pm$ 0.18
QCD+Chiral Perturbation [36]	-0.05 $\pm$ 0.06
Skyrme [38]	-0.13
Skyrme [38]	-0.33
Chiral Hyperbag [39]	0.42 $\pm$ 0.30
Chiral Hyperbag [40]	0.37
Chiral Color Dielectric [41]	-0.030 $\to$ -0.20
NJL Soliton [42]	-0.05 $\to$ 0.25

Hadjimichael, Poulis and Donnelly have examined the suitability of QE scattering from the deuteron for determining single nucleon form factors [43]. They found that the modification of the deuteron asymmetry from the final state interactions is small and relatively independent of the nucleon-nucleon(NN) interaction model for backwards angle scattering near SAMPLE's kinematics. In this work, the static approximation is compared to two extreme NN interaction models. One model has strong short and medium range interactions while the other model is a soft-core model with weaker short and medium range interactions. Realistic NN potentials should fall between the two potentials used. The modification of the asymmetry by final state interactions was found to be approximately one percent for electrons scattered at an angle of 170° when one-body currents are taken into account.

More recent calculations specifically for the kinematics of the SAMPLE experiment confirm that the corrections for final state interactions are small and independent of the model used for the NN potential. Diaconsescu, Schiavilla and van Kolck calculated the PV asymmetry including both one and two-body currents with realistic NN potentials [44]. This work was to extended to include PV interactions between the nucleons and anapole couplings of the photons [45]. The inclusion of two-body effects, including PV NN interactions changes the asymmetry at approximately the one percent level. These studies confirm that the correction to the static approximation is small, and that QE $e^- - d$ can be used as probe of single nucleon form factors.

Pollock has calculated the PV asymmetry in elastic $e^- - d$ scattering [46]. Based on his calculation, the asymmetry is estimated to be:

$$A_{el} = \frac{G_F Q^2}{\pi\alpha\sqrt{2}} \sin^2\theta_W \left(1 + 2G_M^s \frac{F_T}{m u_d}\right) \tag{1.48}$$

where F_T is the fraction of the elastic cross section due to magnetic scattering and μ_d is the magnetic moment of the deuteron. The elastic asymmetry is comparable in size the the quasi-elastic asymmetry, but the cross section is only two percent of the quasi-elastic asymmetry. Because the cross sections is small, uncertainty in the elastic

asymmetry will not be a significant factor in the determination of single nucleon form factors from the PV asymmetry $e^- - d$ scattering. The calculations discussed in this section are used to determine the dependence of the asymmetry in $e^- - d$ scattering on single nucleon form factors in Chapter 4.

Chapter 2

Experimental Technique and Apparatus

In order to determine G_M^s and G_A^e, the experiment measures the asymmetry in the cross sections for positive and negative helicity electrons scattered elastically or quasi-elastically from unpolarized hydrogen and deuterium. The asymmetry is defined as

$$A_{physics} = \frac{\sigma^+ - \sigma^-}{\sigma^+ + \sigma^-} \tag{2.1}$$

where $\sigma^{+(-)}$ is the cross section for quasi-elastic scattering of positive(negative) helicity electrons. The asymmetry is easier to measure than the absolute cross sections because σ^+ and σ^- are both directly proportional to the detector gain and acceptance. The cross sections can all be replaced by Y, the detector yield, which is simply the signal in the detector divided by the incident beam charge. This gives the measured raw asymmetry

$$A_{raw} = \frac{Y^+ - Y^-}{Y^+ + Y^-} \tag{2.2}$$

which is proportional to the physics asymmetry. The constant of proportionality involves primarily the polarization, signal to background ratio and radiative corrections. The determination of these constants of proportionality is discussed in detail in Chapter 3.

The aim of this experiment is to determine the asymmetry to 0.2 parts per million. This level of accuracy requires approximately 1000 hours of beam on target to get the necessary statistical uncertainty, and precise understanding of systematic effects. Experimental runs using substantially the same apparatus have been performed on Hydrogen in 1997 [47] and 1998 [48].

In principle, one could measure Y^+ for one month then measure Y^- for another month. The asymmetry could be determined from the combination of two very precise yield measurements. However, the stability of the detector and beam properties would have to be good enough that the signal would not vary by more 0.1 ppm for many weeks. This level of control over detector gain and beam properties is not practical.

In practice, the necessary 10^9 separate asymmetry measurements are made out of opposite helicity beam pulses separated by only $\frac{1}{60}$ s. Individual asymmetry measurements have a standard deviation of approximately 0.3 percent. Therefore even instabilities in the apparatus that cause a variation in the detector signal of 1 part in a thousand over $\frac{1}{60}$ s will not perturb the measurement, provided that they are not correlated with the beam helicity. Gain, backgrounds, target thickness and beam properties can all vary over the course of the experiment. As long as the variation is not correlated with beam helicity and is slow compared to the time it takes to form an asymmetry measurement, the average and standard deviation of the measured asymmetry will not be significantly affected.

The requirement that the plus and minus helicity states of the beam have the same properties is still challenging, but the Bates Linear Accelerators Center can meet the stringent requirements for the polarized beam using the polarized source (Section 2.1). The technique for generating polarized electrons uses electro-optic components to quickly switch the polarization of light hitting a GaAs photocathode. The polarization of the light determines the polarization of the resulting electron beam. The technique used to change the helicity also introduces small helicity correlated changes in the

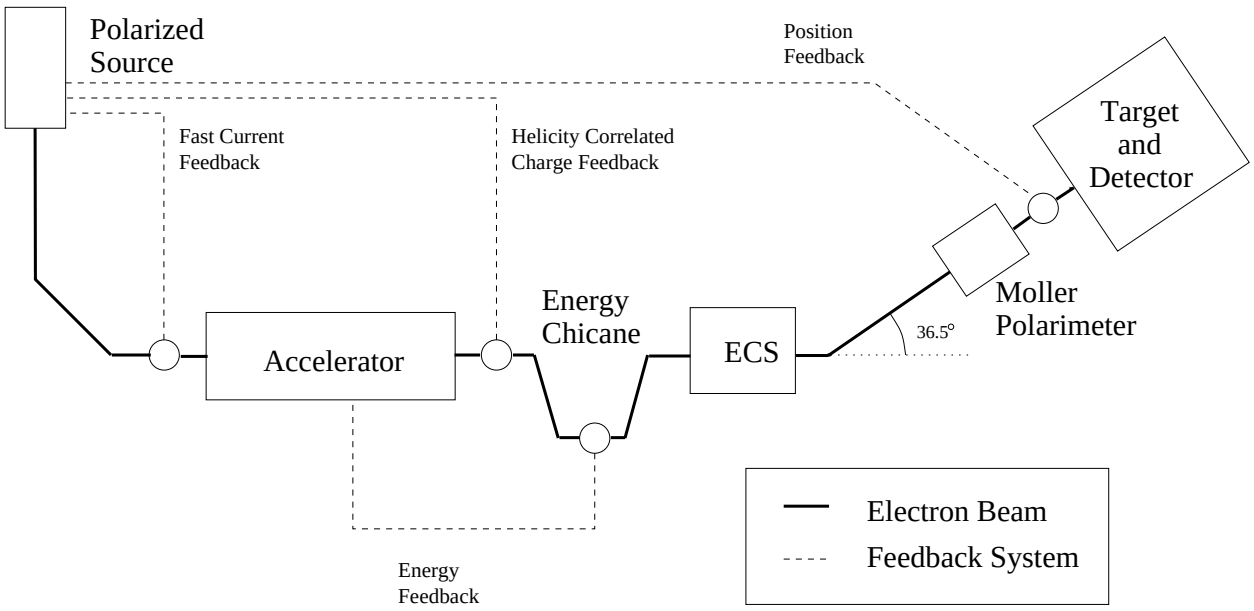

Figure 2.1: Experimental schematic. The major elements in the apparatus are shown, with the feedback mechanisms used to stabilize the position, intensity and energy of the electron beam.

position and intensity of the laser beam. Feedback systems are used to correct for these helicity correlated differences. A schematic representation of the experiment is shown in figure 2.1, including the feedback systems used to stabilize the electron beam.

The linear accelerator boosts the electrons up to the 200 MeV energy used in the experiment. The accelerator is a pulsed machine capable of delivering electrons between 100 MeV and 1 GeV in pulses of 25 μs at 600 Hz. The acceleration is accomplished with 6 transmitters powered by 12 klystrons , only some of which are needed to provide the 200 MeV electrons used in the SAMPLE experiment.

The polarization of the beam is measured by a Møller polarimeter placed after the bend into the North Hall. The Møller polarimeter is based on the asymmetry in polarized e^-—e^- scattering. In addition to measuring the magnitude of the polarization, the Møller polarimeter is used in setting the direction of the polarization. The placement after the bend into the experimental hall puts the polarimeter after all the elements which can rotate the polarization.

The target (Section 2.5) and detector (Section 2.6) were custom built for the experiment. The target is a cryogenic liquid cell. It is designed to take a 500 W heat load from the beam without significant density fluctuations, and to minimize changes in target path length with changes in beam position. The detector is a 1.5 steradian air Cerenkov detector centered around the 180° scattering angle. The backscattered electrons emit Cerenkov light in air and mirrors focus the light onto phototubes. The detector is integrated over each beam pulse in its normal operating mode, requiring that the signal to background ratio be determined separately.

2.1 Polarized Source

The polarized source generates polarized electrons from circularly polarized light incident on a GaAs photocathode. The method for switching the polarization of the light uses an electrically reversible $\lambda/4$ plate to turn linearly polarized laser light into either left or right circularly polarized light. The theoretical maximum polarization for the emitted electrons from a bulk GaAs crystal is 50%, but some depolarization occurs in the transport to the crystal's surface [49][1]. Additional active elements in the laser line are used to stabilize the electron beam current within a pulse and the helicity correlated differences in current and position. The laser and optical elements are described in Section 2.1.1. Feedback systems used to correct for helicity correlated beam differences are described in Sections 2.1.2 and 2.1.3.

The pattern of beam pulse helicities is most important method used to minimize systematic effects on the beam. The accelerator operates at 600 Hz, locked to the 60 Hz from the AC power. Ten pulses occur within one cycle of the line frequency, and the pulses are divided into ten "timeslots". The first timeslot is locked to the zero

[1]Strained GaAs crystals can provide higher polarization electrons, but they introduce additional difficulties. A high polarization source for the Bates Linear Accelerator Center which utilizes a strained GaAs crystal is described in Appendix A.

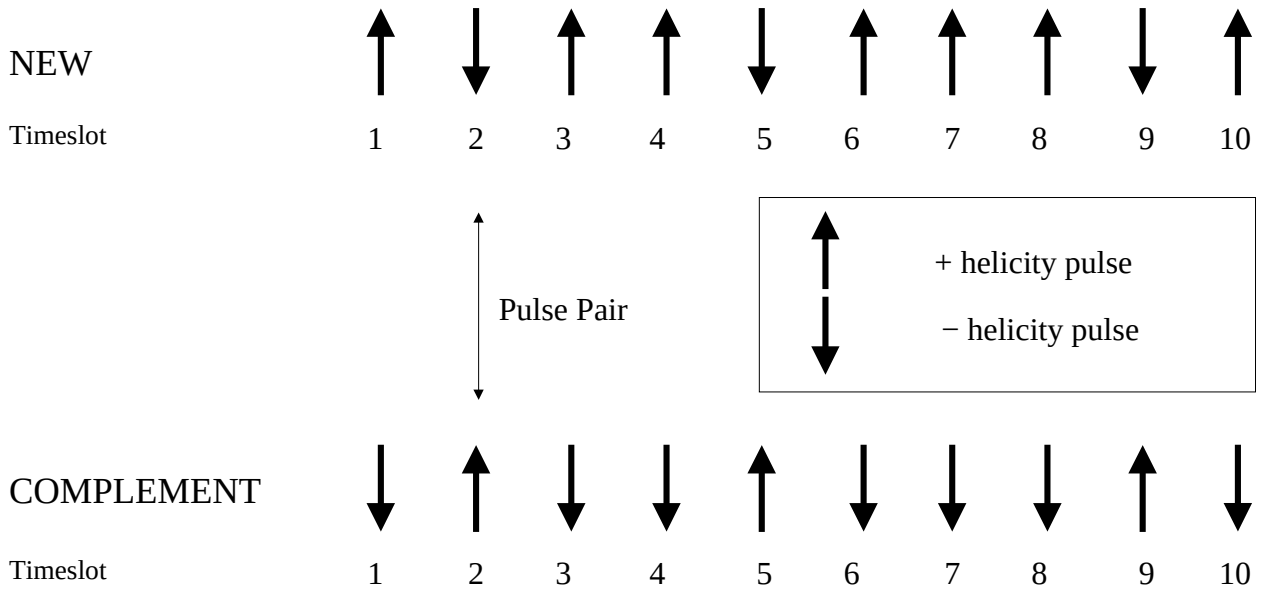

Figure 2.2: Helicity pattern. The NEW sequence is a pseudo-random sequence of helicities generated in the source computer. Then NEW sequence is followed by the COMPLEMENT sequence, in which each time slot has the opposite helicity of the corresponding NEW time slot. Asymmetry pairs are formed from pulses 10 time slots ($\frac{1}{60}$ s) apart.

crossing of the line voltage. The source computer chooses a pseudo-random sequence of helicities for a NEW sequence of ten pulses. The next sequence of ten pulses is the called the COMPLEMENT sequence. The helicity of a pulse in a timeslot in the COMPLEMENT sequence is the opposite of the corresponding time slot in the NEW sequence. Asymmetry pairs are formed from the same time slot in the NEW and COMPLEMENT cycle, as shown in Figure 2.2.

This pattern of helicities cancels out two broad classes of potential systematic errors. First, the effects of 60 Hz line noise on both the beam and the measurement electronics are canceled out. Additionally, since the positive helicity pulse occurs first in half of the asymmetry pairs the average time difference between the positive and negative pulses is zero. This means that any slow time drifts in the apparatus average out in the asymmetry measurement.

2.1.1 Laser and Optical Elements

A 30 W continuous wave argon laser drives a Ti-sapphire laser to generate the linearly polarized light. A mechanical chopper wheel is used to reduce the thermal load on the Ti-sapphire crystal. The Ti-sapphire laser can generate a peak power of 8 W at approximately 750 nm. The laser is followed by several elements used to modulate and polarize the light, shown in Figure 2.3. After the laser beam has passed through all the polarizing and modulating optics, a peak power of 3 W is available at the photocathode.

The circular polarization and most of the intensity modulation of the laser beam is accomplished using Pockels cells. A Pockels cell is a crystal which can be made birefringent by the application of a voltage along one axis [50]. The index of refraction for light polarized along this axis varies linearly with the applied voltage. For the correct voltage, light polarized along one axis will develop a phase difference of $\frac{\pi}{2}$ relative to the light polarized along the other axis as it traverses the crystal. The axis with the higher index of refraction is called the slow axis, while the axis with the lower index of refraction is called the fast axis. Light with a linear polarization 45° away from the crystal axes will be turned into circularly polarized light. Reversing the voltage on the Pockels cell reverses the phase difference, changing the handedness of the light. The Helicity Pockels Cell (HPC) is operated this way. The polarization rotation caused by Pockels cells can be used with a linear polarizer to modulate the intensity of the beam.

The HPC also introduces helicity correlated differences in beam position and intensity. Because the piezoelectric effect occurs in crystals with the same symmetry classes as those that exhibit the Pockels effect (crystals which lack a center of symmetry [50]), the HPC also exhibits piezoelectric shape changes. These shape changes can in turn change the angle of the beam slightly, making helicity correlated differences in the laser beam position at the crystal. These position differences are corrected

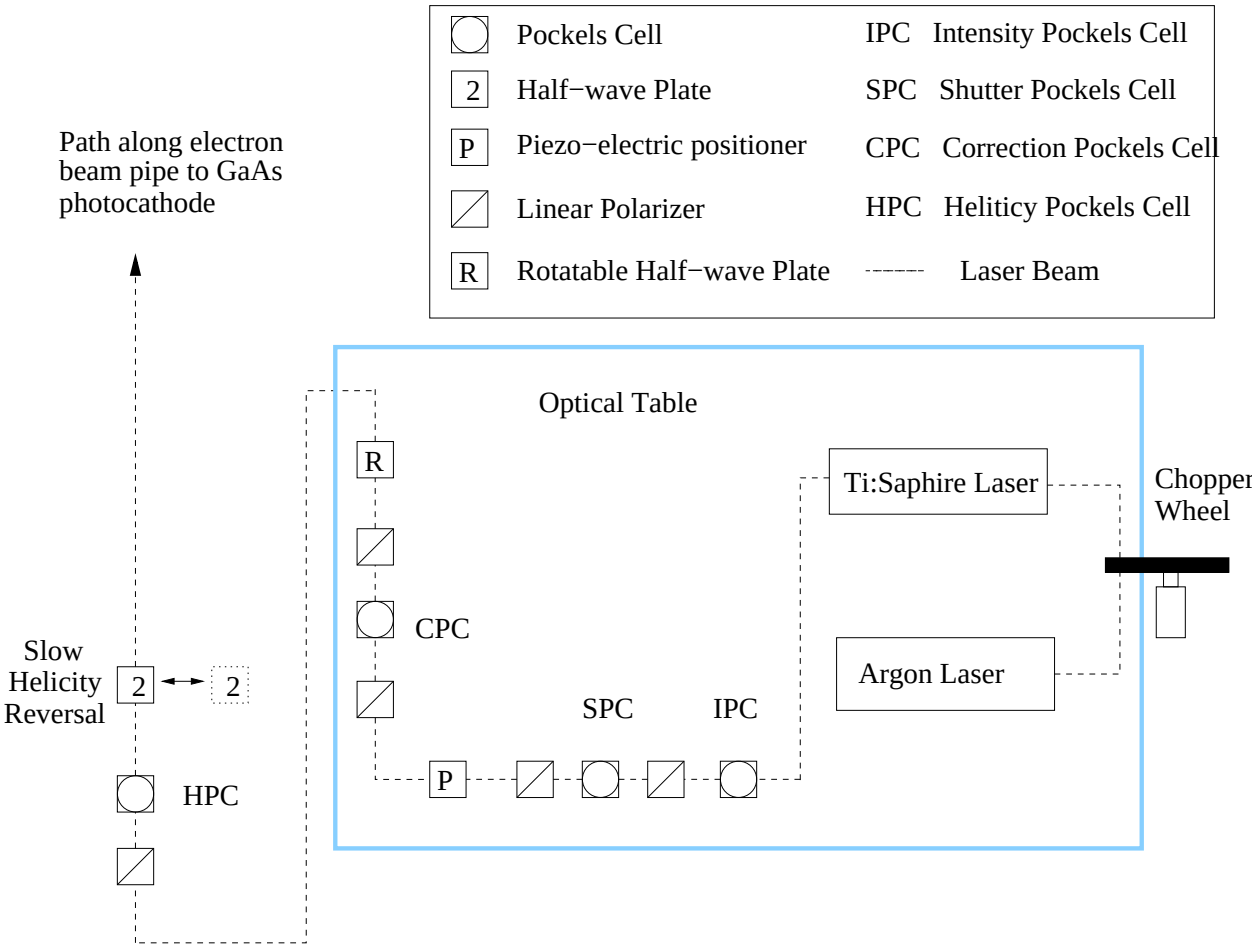

Figure 2.3: Laser beam line and optics. The optical elements in the beam line are shown in order. Most of the elements are on an optical table in the source room, with two exceptions. The chopper wheel is mounted on the floor to reduce the vibrations on the optical table. The HPC is located in the accelerator vault underneath the source room, after all the mirrors. This position, as close as possible to the photocathode, minimizes the position differences and PITA effect.

using a feedback system described in Section 2.1.2. Imperfections in the crystal and its alignment can also leave a residual linear polarization in the laser beam, which is affected by the voltage on the Pockels cell. Because linear polarization affects the transmission and reflection at surfaces, the changing residual linear polarization leads to an intensity asymmetry at the crystal. This Polarization Induced Transmission Asymmetry (PITA) effect in the laser beam makes a helicity correlated charge difference in the electron beam. Another feedback system, described in Section 2.1.3, modulates the laser beam intensity to correct this effect.

Pockels cells sandwiched between linear polarizers are used to modulate the intensity of the laser beam. The Shutter Pockels Cell (SPC) can rotate the polarization 90° using a phase shift of π between the fast and slow axis of the crystal. The incident light must be polarized 45° from the crystals axes, as is the case when a Pockels cell is used to generate circularly polarized light. The SPC is between two crossed polarizers, so when the voltage is applied and the polarization is rotated the light can pass through the second polarizer.

The Intensity Pockels Cell (IPC) and the Correction Pockels Cell (CPC) are used to make small changes in the intensity of the laser beam. They are both sandwiched between parallel linear polarizers. The Pockels cell is set to a voltage which provides a small phase shift between the fast and slow axes. This creates elliptically polarized light from linearly polarized light incident on the Pockels cell. Increasing the voltage makes the light more circularly polarized, which causes more light to be lost on the second polarizer. Decreasing the voltage makes the light more linearly polarized allowing more of it to pass through the second polarizer. The IPC is used to stabilize the current of the electron beam within a pulse (independent of helicity) while the CPC is used to correct for the PITA effect (necessarily a helicity correlated correction).

2.1.2 Position Feedback

The position feedback corrects position differences caused by the HPC by displacing the laser beam in a helicity correlated way. The deformation the HPC experiences when the voltage is changed causes small angular displacements in the laser beam which results in a position difference at the crystal. A quartz optical flat mounted on piezoelectric actuators is used to correct for these helicity correlated position differences by displacing the beam so that position differences are nulled. The optical flat is mounted so that the laser beam is perpendicular to the plane of the optical flat, and small tilts will result in a displacement of the laser beam. The piezo actuators are set to a different position for each helicity state, correcting the position differences observed at the target. Even though the measurements are made at the target, the correction is made in the laser beam; this minimizes secondary effects that could occur through the electron beam scraping on apertures in a helicity correlated way.

Software on the source computer is used to control the piezo electric actuators. The three actuators in the mount are capable of tilting the flat in two directions independently, allowing both horizontal and vertical positions differences to be corrected. The polarized source data acquisition and control system sets the position of the actuator for each helicity state. The slope is measured by setting the piezo actuators to make large position differences and measuring the response of the electron beam at the target. Generally the axes of the electron beam position measurements are linear combinations the axes of the piezo movements, therefore a system of two linear equations must be solved to determine the appropriate settings to null out the position differences. The system is described in greater detail in [51].

The system greatly reduces helicity correlated beam motion with a relatively minor overhead in running time. The slope must be measured every time the changes are made to the polarized source; inserting or removing the half-wave plate for example. Measuring the slopes takes about an hour and is necessary only once every several

days. It take about eight hours to collect a enough statistics to make a change in the position correction, but this can be done while taking data. The end result is a reduction in the average helicity correlated position difference from hundreds of manometers to tens of nanometers.

2.1.3 PITA Correction

The PITA effect arises from imperfections in the circularly polarized light. A residual linear component remains even after the light passes through the HPC. This linear component is generally different for the different helicity states of the beam. The different linear polarizations have different transmission through the surfaces between the HPC and the crystal, resulting in different intensity at the crystal. This leads to a charge asymmetry in the electron beam as large as 100 ppm, which could lead to false asymmetries. The PITA correction system reduces the average charge asymmetry to a typical value of only a few ppm.

A charge difference between the two helicity states could lead to a false asymmetry in several ways. Nonlinearities in the detector are the most direct route. Changes in other beam properties caused by a charge asymmetry could also lead to false asymmetries. Helicity correlated energy, position and background differences could be caused by a charge asymmetry at the accelerator. In pulsed accelerators an effect called beam loading occurs because a bunch of electrons passing through the RF cavities reduces the intensity of the RF field. A bunch with more electrons reduces the field more, leading to less energy per electron. Since the scattering cross section for $e^- - d$ collisions varies with energy, this would lead to a false asymmetry. The beam loading could also change the background by making the beam pass closer to a collimating edge in the beam line, (e.g. the energy defining slits in the Energy Compression System).

By dramatically reducing the charge asymmetry at the end of the accelerator,

the PITA correction system reduces these potential sources of false asymmetries to acceptable levels. The PITA correction system uses the source computer to monitor the charge asymmetry at the end of the accelerator and adjust the voltage on the CPC to remove the charge asymmetry. An interface box uses the set voltage from the computer to apply a different voltage to the CPC for the two helicity states. The computer averages the charge asymmetry over approximately three minutes to determine a new setting. The charge asymmetry responds linearly to the voltage applied to the CPC over a range of several hundred ppm. The slope of the response is measured by setting the voltage difference on the CPC to its maximum and minimum values and measuring the resulting charge asymmetry at the end of the accelerator. Because the slope is typically stable for weeks at a time the system uses very little beam time.

2.2 Electron Beam Transport and Acceleration

After the electrons are emitted from the photocathode, they are accelerated by a 60 kV potential to a Wien filter which is used to set the direction of the electron beam polarization. An additional 300 kV potential is used to raise the energy of the electrons for injection into the accelerator. Dipole magnets are used to bend the electron path 90° into the accelerator.

The accelerator uses a series of RF cavities operating at 2856 MHz to accelerate the beam to 200 MeV. An RF chopper, prebuncher and buncher separate the continuous 25 μs electron pulse into packets with a phase spread of only a few degrees. The phase in the accelerator cavities is set so that the electron packets reach the cavities while the field strength is at a maximum. Setting the phase on the peak makes the energy less sensitive to small drifts in the phase of the accelerator cavities since the derivative at the peak is zero. Immediately following the accelerator is the Energy

Compression System (ECS), which reduces the spread of electron energies. The ECS system includes a dispersive region which is used to measure the beam energy. Finally, dipole magnets in the beam switch-yard bend the beam 36.5° into the experimental hall.

2.2.1 Polarization Direction and the Wien Filter

The primary use of the Wien filter is to set the electron beam polarization to be longitudinal at the target. The electrons are emitted from the photocathode with longitudinal polarization, but the $g-2$ precession of the electrons in the final bend into the experimental hall puts the polarization 16.6° relative to the momentum vector. The Wien filter uses crossed electric and magnetic fields to set the polarization $-16.6°$ away from the momentum so the the polarization is longitudinal at the target. The $g-2$ precession in the 90° bend before accelerator is negligible because the electron energy is only 360 keV at that point. The electric field is set so that it balances the Lorentz force from the magnetic field, so that the only effect on the electron beam is the rotation of the spin.

Setting the spin is complicated by the solenoid magnets used to focus the beam, which can rotate the transverse component of the polarization out of the plane of the bend into the experimental hall. During the setup for the run, a combination of solenoid settings is found that produces acceptable electron beam optics and puts the transverse component in the bend plane at the bending magnets in the switch-yard. These solenoids are set at fixed values throughout the run and closely monitored. A few additional sets of solenoids avoid spin rotation by having the field direction reversed in adjacent solenoids. This allows focus adjustments to be made during the run without disturbing the polarization direction. The calibration of the Wien filter and the solenoid setting is described in Section 2.4.2.

2.2.2 Energy Compression System and Energy Measurement

The Energy Compression System (ECS) is used to narrow the spread of the beam energy. It reduces the energy spread within a beam pulse as well as between pulses. The ECS has two major parts, a dispersive region and an RF cavity. The dispersive region of the beam line spreads out the beam in space and time according to energy. The RF cavity exploits the time separation to narrow the spread in beam energy, while collimators and position monitors exploit the spatial separation to limit and measure the beam energy.

A dispersive region is created using two dipole magnets bending in opposite directions and displacing the beam parallel to its original path. Because higher energy electrons are bent less by magnetic fields, the higher energy electrons travel closer to the original path. The position in the chicane is proportional to the energy. A water cooled collimator in this region is used to limit the electron beam energy variations to within plus or minus $\frac{1}{2}$ % of the nominal value, and a beam position monitor is used to measure the beam energy. Two more dipole magnets bend the beam back onto its original path, which removes the spatial separation. However, because the lower energy electrons travel a longer path it takes them longer to traverse the chicane.

The RF cavity after the chicane compresses the beam energy. This is accomplished by setting the phase of the RF so that it has a zero crossing at the middle of the phase packet. The higher energy electrons lose energy in the cavity and lower energy electrons arrive after the zero crossing and gain energy. The beam energy within a pulse is narrowed by a factor of ten, from 1.4% to .14%.

2.2.3 Energy Feedback

The energy feedback system at Bates was implemented to reduce the variation between time slots and over long time scales. Variation in energy that is too large will cause scraping on energy limiting slits in the ECS chicane. Scraping on the slits can

lead to backgrounds in the experimental hall which are unstable enough to disturb the asymmetry measurement; this effect of energy variation led to the development of the energy feedback system. The variation in energy comes from two types of sources, slow drifts in accelerator RF phase and noise from the AC power cycle on the different time slots. The main source of slow drifts in RF phase is the temperature of the cooling water for the RF cavities. The feedback system addresses both types of variation by measuring and correcting each time slot separately. The energy feedback system reduces the energy fluctuations from 0.4% to .02% [52].

The energy for each time slot is measured at the ECS chicane and corrected independently using a fast phase shifter on an accelerator RF cavity The source computer averages the energy measurements made in the ECS chicane over several seconds, collecting the average energy in each time slot. The phase shifts needed to correct the measured energies — one for each time slot — are computed and sent to the phase shifter. The RF cavity used to correct the energy is similar to the other cavities used to accelerate the beam, but it is operated off peak so phase adjustment can increase or decrease the energy of the beam.

2.3 Electron Beamline Instrumentation

The beamline instrumentation measures the properties of electron beam to provide information about beam quality to the accelerator operators and to provide data about helicity correlated differences in the beam for correction. The instruments used to monitor helicity correlated beam differences can be used without affecting the beam and are recorded continuously while data is being taken. Non-invasive instruments are available for measuring the charge and position of each beam pulse, as well as background levels in the hall. The beam profile can also be measured, but the instrument to do this sweeps wires through the electron beam.

Table 2.1: Instrumentation and shielding locations.

Instrumentation and shielding locations. Location is given relative to the center of the target.

Name	Description	Location (in)
Lead Wall	4" thick	104
NH2X(Y)	SLAC-style BPMs	172
HA1(2)X(Y)	four halo monitors	249
NH1X(Y)	SLAC-style BPMs	334
SSS2H	horizontal steering coil	445
SSS2Y	vertical steering coil	468
SSS1H	horizontal steering coil	591
SSS1Y	vertical steering coil	638

The charge measurement is performed with instruments called toroids; these are wire wrapped mu-metal toruses around the beam pipe. The voltage induced in the toroid is proportional to derivative of the beam current. An ideal beam pulse which had a sharp turn on followed by a constant current and a sharp turn off would produce a spike on the toroid current at the beginning of the beam pulse and a spike of the opposite sign when the pulse ended. Integrating the the signal from a toroids gives a signal which is proportional to the current in the toroid at any given time. This signal is then integrated over the duration of a beam pulse in order make a signal which is proportional to the total charge in a beam pulse. Calibration is performed by sending a known amount of charge through a loop of wire that goes through the toroid.

The charge monitors are used for monitoring beam quality, charge normalization and helicity correlated corrections. There are many charge monitors along the beam line. These allow the accelerator and experiment personnel to determine if any of the

electron beam is being lost and whether or not there is helicity correlated loss. Many other instruments give signals which are proportional to the beam charge, including the main SAMPLE Cerenkov detector and the beam position monitors. This makes the charge monitors near the detector important for determining both the position of the beam and the normalized detector yield.

Two types of beam position monitors (BPMs) are used in the beamline. The beam position near the target is measured by SLAC-style beam position monitors. These BPMs are cavities tuned to the 2856 MHz accelerator frequency. The interference between the signal generated by the cavity and the klystron drive frequency is proportional to both the beam current and the distance of the beam pulse from the center of the cavity. NIKHEF-style BPMs are used in the linear accelerator.

The beam position monitors are used both to monitor the beam quality and correct for helicity correlated differences. The energy measurement is also performed using a BPM in a dispersive region of the beam line. Beam position monitors just before the target allow for the position and angle of the beam at the target to be determined. The energy as well as the beam position and angle at the target are used for helicity correlated beam difference corrections. The BPMs can be calibrated by moving the beam with steering elements with known calibration.

A set of four 'halo' detectors monitors the background in the hall. These detectors are simple lucite cylinders attached to phototubes, and they monitor the charged particles background through the Cerenkov radiation created in the lucite. They are placed directly adjacent to the beam pipe and provide an indication of beam quality. When the beam is scraping on an aperture the signal in the halo monitors becomes large and more unstable.

Lutes and BeO flip targets are used to determine beam shape as well as position. Both work by placing material in the beam and cannot be used while the detectors are on. The lutes are wires attached to actuators that can be swept through the electron

beam. Secondary electron emission from the wire causes a current flow proportional to the current hitting the wire. When the lutes are swept through the beam a profile of the beam can be developed. These measurements are most useful for determining the size of the beam near apertures and at the target. The BeO flips targets are thin BeO foils than can be remotely flipped into the beam. Video cameras are then used to look at the shape and position of the beam. The BeO targets are most useful for making quick determinations of the beam position and shape, for example when the beam is steered into position for a Møller polarimeter measurement.

2.4 Møller Polarimeter

The Møller polarimeter is used to determine both the magnitude and direction of the polarization. The polarimeter is based on the asymmetry in Møller, or polarized $e^- - e^-$ scattering which is calculable in QED. The target particles are the electrons in a magnetically saturated thin metal foil. The detector is set up to detect electrons scattered at 90° in the center of mass frame. The asymmetry at a scattering angle of 90° in the center of mass frame is given by [53]

$$A_M = -\frac{7}{9}P_z^B P_z^T + \frac{1}{9}P_y^B P_y^T - \frac{1}{9}P_x^B P_x^T \tag{2.3}$$

where P_i^B is the beam polarization along coordinate i and P_i^T is the target polarization along coordinate i. The choice of the 90° scattering angle maximizes the asymmetry.

The target is a Supermendur foil which can be polarized longitudinally or vertically, and rotated about a vertical axis. The Supermendur foil is composed of 49% Co 49% Fe and 2% Va by weight and saturates in a magnetic field of $100\ G$. Two sets of Helmholtz coils, one perpendicular and one parallel to the beam path, can be used to saturate the target in different directions. The target polarization has been measured to be $8.02 \pm 0.12\%$ [54]. With this setup the target electrons can be set to have a non-zero spin projection along any axis, therefore, the polarimeter is capable

of measuring the direction as well as the magnitude of the beam polarization.

A spectrometer selects the electrons scattered at 90° in the CM frame. First a tungsten collimator at $4.041° \pm .011°$ in the lab frame limits the electrons to those scattered at 90° in the CM frame. Two magnets are then used to transport the electrons to the detector. First the electrons are bent to the side, then down into the detector. The current in the magnets determines the energy of the electrons which reach the detector.

The detector is a lucite Cerenkov detector and the data acquisition system uses the same electronics and computers as the normal data acquisition system. The signal in the Møller detector is integrated over a beam pulse and normalized by the charge measured in a nearby toroid. Asymmetries are formed between the positive and negative helicity pulse pairs and corrected for the dilution from the background.

2.4.1 Polarization Magnitude

Measurements of the polarization are performed every couple of days, when the state of the helicity reversing half wave plate is changed. A measurement with a statistical uncertainty of 1% of the polarization can be performed in less than one hour. For a measurement of the polarization, the foil is first saturated while it is perpendicular to the beam direction. The foil is then rotated to 30° for data collection; this puts a component of the target polarization along the beam bath while still presenting a thin target to the beam.

Measurements of the yield and asymmetry are performed at the Møller peak scattering energy of 100MeV and on both sides. This allows the background to be estimated so that the dilution of Møller asymmetry can be determined. The data from a typical measurement can be seen in figure 2.4. Most of the time is spent measuring the asymmetry at the peak, where the signal to background ratio is highest. The shape of the Møller yield was determined by a Monte Carlo simulation using GEANT

[54] and the background is assumed to be linear under the peak. The dilution factor for each asymmetry point is determined for each data point by the fit to the yield data; these dilution factors are used to determine the shape asymmetry as a function of scattering energy. Once this shape is determined, the magnitude of the asymmetry is determined by a fit to the data. If the direction of the beam polarization has already been determined the polarization can be determined with a single asymmetry measurement.

The polarization magnitude measurements were performed approximately every two days. The average of all the polarization measurements over the course of the run gives the beam polarization, $P_b = 35.7 \pm 1.4\%$. The uncertainty is due to the systematic error in the Møller asymmetry, which primarily comes from uncertainty in the target polarization and signal to background estimation.

2.4.2 Setting the Polarization Direction

Since the Moller target direction can be polarized in several direction, it is straightforward to determine the direction of the polarization using equation 2.3 and the known polarization of the target. The electron beam has a longitudinal polarization at the photocathode, but it can be rotated by the Wien filter, the solenoids and $g-2$ precession before it arrives at the polarimeter. The beam polarization at the deuterium target should be identical to the target polarization at the Møller polarimeter; there are no elements which should cause a spin rotation between the two. The direction of the beam polarization at the target can be described by

$$\begin{aligned} P_x^B &= P^B(\cos\theta_g \sin\theta_W \cos\phi + \sin\theta_g \cos\theta_W) \\ P_y^B &= P^B \sin\theta_g \sin\phi \\ P_z^B &= P^B(\cos\theta_g \cos\theta_W - \sin\theta_g \sin\theta_W \cos\phi) \end{aligned} \tag{2.4}$$

where $\theta_g = 16.57^\circ$ is the g-2 precession from the bend into the experimental hall, θ_W is the precession in the bend plane caused by the Wien filter and ϕ is the net

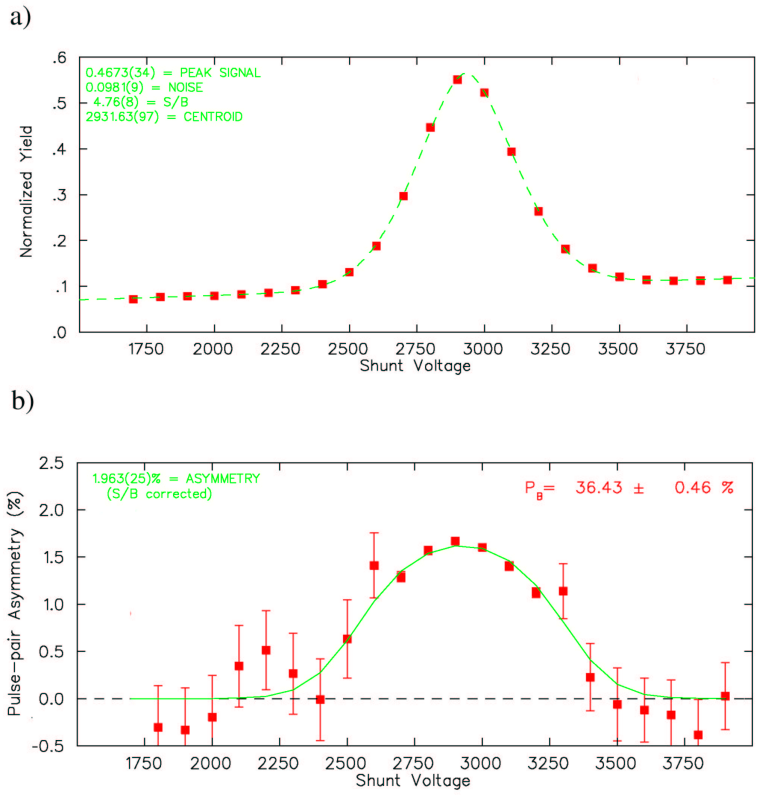

Figure 2.4: Data from a single polarization measurement a) The normalized yield as a function of shunt voltage on the spectrometer magnets. The shunt voltage is directly proportional to the scattering energy. The fit to the data is the dashed line. b) The asymmetry as a function of shunt voltage. The fit to the data is the solid line. The shape of the curve the asymmetry data is fit to is determined by dilution factors calculated from the fit to the yield curve. Points off the peak have larger error bars because less time is spent measuring the asymmetry where the background off the peak.

rotation caused by the solenoids. The typical procedure is to first calibrate the Wien filter, allowing θ_W to be set to a known value. After the Wien filter is calibrated, the solenoids are calibrated so that the net rotation can be set to zero.

The two set of Helmholtz coils can polarize the target vertically or longitudinally. When target is polarized with the longitudinal coils, the Møller asymmetry is given by

$$A_L = \frac{P^B P^T}{9} \times [(7\cos\theta_T \sin\theta_g - \sin\theta_T \cos\theta_g)\sin\theta_W \cos\phi - (7\cos\theta_T \cos\theta_g + \sin\theta_T \sin\theta_g)\cos\theta_W] \tag{2.5}$$

where θ_T is the angle from the beam direction and positive rotations move the downstream edge of the target beam left. When the target is polarized with the vertical coils, the Møller asymmetry is given by

$$A_T = \frac{P^B P^T}{9} \sin\theta_W \sin\phi \tag{2.6}$$

The calibration of the Wien filter is the first step because it can be performed independent of ϕ. The calibration is done using the longitudinal coils to polarize the target. When the target is set to $\theta_t = 64.6°$, known as the magic angle, the first term in equation 2.5 is zero and the asymmetries dependence on ϕ is eliminated. The measured Møller asymmetry as a function of the Wien filter setting is fit to the expression in equation 2.5 to determine the calibration. Previous measurements have found that $\theta_W = \alpha V$ where V is the voltage across the plates of the Wien filter and $\alpha = 17.10 \pm 0.27$ degrees per kV is the calibration constant.

The solenoids can be calibrated using either the longitudinal or vertical target coils. In either case, the asymmetry is maximized by setting $\theta_W = 90°$. When the target is polarized in the vertical direction, the Møller asymmetry is given by equation 2.6. Alternatively, the longitudinal coils can be used. The asymmetry for the longitudinal coils is maximized when the θ_T is set to $-25.6°$. The asymmetry is plotted as a function of the current in a group of solenoids, I. The rotation angle is

calibrated by making the substitution

$$\phi = \beta * I + \gamma \tag{2.7}$$

equation for the Moller asymmetry, where β is the spin rotation per unit current, and γ is the offset. The values of β and γ are determined by fitting the data.

The different target polarizations have different advantages. The asymmetry is a factor of two larger for the longitudinal target polarization, generally allowing more precise results. However, the vertical polarization may be preferred when determining γ because it is has a zero crossing at the desired value of $\phi = 0$. The zero crossing makes it easier to determine γ with only a few points, and its location at the desired value of ϕ reduces the amount of time spent tuning the beam to accommodate solenoid changes. Complete scans with both target polarizations have been performed, measuring β to be 55 degrees per Ampere.

Provided the beam is at the same energy, β will be constant for a set of solenoids. However, the offset may change when solenoids are used to tune the beam. Because the rotation changes when changes are made to any solenoids, the solenoid settings are all fixed once the spin direction is set. In the deuterium data taking run, the spin direction was fixed by locating the current setting for the zero crossing in the vertical target polarization asymmetry. When the polarization direction was checked during the run, the solenoid settings gave a value $\phi = 34.7°$, resulting in a transverse polarization at the target. The mis-calibration was corrected halfway through the experiment, and the spin rotation was found to be consistent with zero at the end of the experiment. The transverse component of the polarization can cause a parity conserving asymmetry in the target. The effect of the transverse component of the polarization is discussed in Section 3.4

2.5 Target

The target is a 40 cm cylinder containing liquid deuterium. It is identical to the target used in previous SAMPLE experiments with liquid hydrogen [55]. Only small changes in the operation of the target system are necessary to accommodate deuterium. Its key features are matching curvature for the entrance and exit windows, low target density fluctuations and high thermal power handling capacity. Typically the target is operated 1 K below the boiling point of the cryogenic liquid and at a pressure of approximately 2 atmospheres.

The target loop, shown in figure 2.5a, consists of a heat exchanger, target cell, heater and pump. During operation the entire loop is suspended in a vacuum chamber. The heat exchanger is cooled by helium gas supplied by a Process Systems International model 1620-S refrigerator. This system is able to absorb the 500 Watts deposited by the beam and maintain the target liquid below the boiling point. The heater is used to keep the heat load on the target constant. The heater is controlled by a computer running National Instruments' LabView and a custom designed monitoring program. The target heater is adjusted based on the beam current detected at the target. The target system is operated with 50 W on the target heater when the beam current is at its nominal maximum; this leaves room to adjust for fluctuations.

The changes to the operation of the target system to accommodate the deuterium liquid primarily involved the filling and emptying of the target. Since deuterium is expensive, large storage tanks were added on the roof of the experimental hall to collect the deuterium in the event of target loss. This also slightly altered the filling of the target, because when the target is filled from the storage tanks it is provided at a lower pressure than the deuterium gas bottles.

Small changes in operating temperatures from the hydrogen target are made because of the higher freezing and boiling points for deuterium. Additionally, the power deposited by the beam is about 20% higher than with hydrogen. These changes are

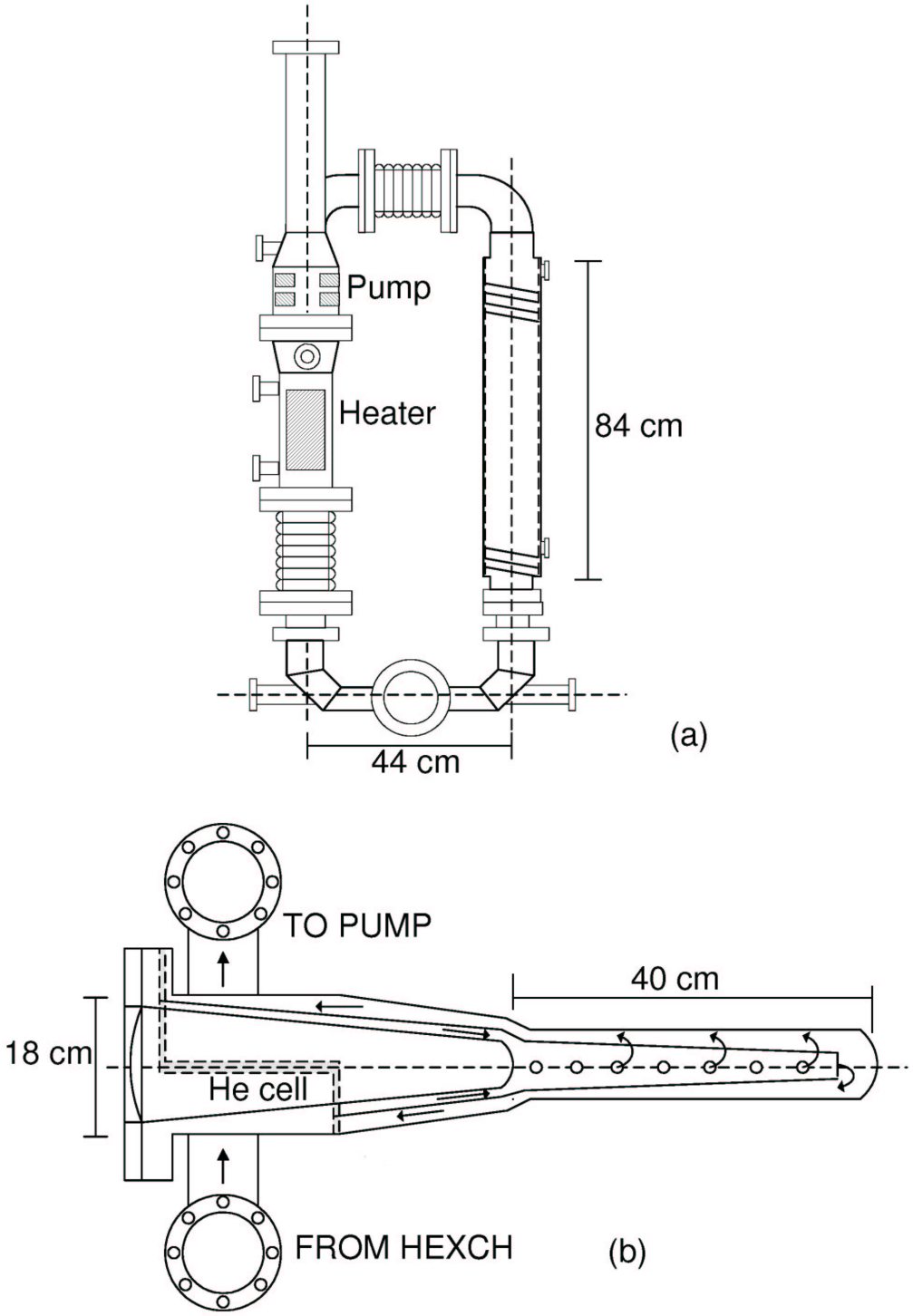

Figure 2.5: Target cell and loop a) The target loop is shown with the pump, heater, target cell and heat exchanger. b) The target cell is shown, including the helium backing cell.

easily accomplished in software.

The target system is intended to keep density fluctuations to levels which will not affect the experiment. Inside the target cell there is an inner baffle with perforations designed to introduce lateral flow into the liquid. The baffle also narrows at the end to keep the flow rate high. This arrangement moves fresh liquid into the beam path, minimizing density fluctuations. The success of the target at limiting density fluctuations can be seen in the relatively small correlation between detector segments.

The matching curvature on the entrance and exit windows is important to keep the path length of the target the same regardless of the beam position. The convex entrance window is matched by the concave exit window. In order to maintain the concave exit window, a cell containing helium gas is attached to the exit window and its pressure is forced to track the pressure of the target cell. Care must be taken in the operation of the target to ensure that the target cell is never at a higher pressure than the helium backing cell. A drawing of the target and backing cells can be seen in figure 2.5b.

2.6 Detector

The main SAMPLE detector is an air Cerenkov detector. It is a relatively simple device which focuses Cerenkov light from the scattered electrons onto photomultiplier tubes. The phototubes are protected by lead shielding and borated polyethylene neutron shielding to improve the signal to background ratio. Figure 2.6 illustrates the detection of an electron by a segment of the detector.

Cerenkov radiation is the process through which the quasi-elastically scattered electrons are detected, and its properties are important for understanding the detector design. Cerenkov radiation is emitted by charged particles moving faster than the speed of light in the medium they are traveling through, which corresponds to about

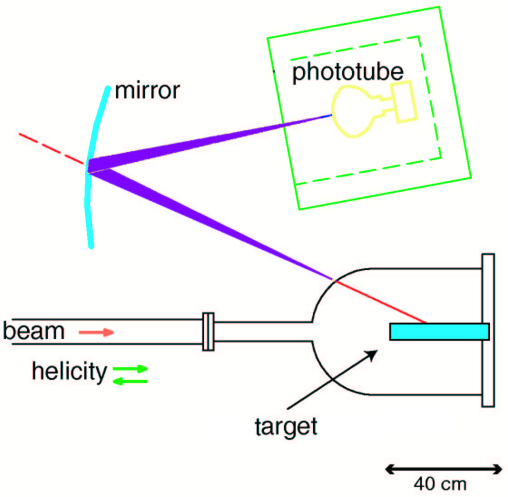

Figure 2.6: Illustration of the target and one detector segment. The electron begins emitting Cerenkov light after leaving the scattering chamber. The Cerenkov light is reflected to the phototube and the electron passes through the mirror. A thin lead sheet surrounding the scattering chamber reduces the bremsstrahlung from the target.

20 MeV for electrons traveling through air. Additionally, the radiation is emitted at an angle given by

$$\cos\theta_C = \frac{1}{\beta n(\lambda)} \tag{2.8}$$

where θ_C is angle relative to the direction of travel, β is $\frac{v}{c}$ for the electron and $n(\lambda)$ is the index of refraction for the wavelength of light. For the quasi-elastically scattered electrons in this experiment, the Cerenkov light is emitted in a cone with a half angle of only 1.5°. In Section 3.2.2 this directionality is used to separate the Cerenkov signal from the isotropic scintillation light.

Remotely operable shutters on the front of the lead cylinders help in determining the background for the detector. The signal in the detector is composed of the Cerenkov light from scattered electrons, scintillation light from backscattered bremsstrahlung radiation and low energy x-rays. The $\frac{1}{16}$ inch aluminum shutters block out both the Cerenkov light and the scintillation light (this combination is

know as the 'light'), but allow the low energy x-rays (the 'dark') to pass through. Approximately 20% of the beam time is spent measuring the dark background. The analysis of the relative contributions to the detector's signal is discussed in Section 3.2.

2.6.1 Acceptance

The mirrors are ellipsoidal sections designed to focus all of the rays emitted from the 40 cm target onto the phototubes. They cover approximately 1.5 steradians, with scattering angles ranging from 123° to 173°. The sections are formed from 62.6 cm squares of glass molded on an ellipsoidal form. The equation for the surface of each mirror is given by

$$\alpha_0 = \alpha_1 x^2 + \alpha_2 xy + \alpha_3 y^2 + \alpha_4 yz + \alpha_5 z^2 + \alpha_6 zx + \alpha_7 x + \alpha_8 y + \alpha_9 z \qquad (2.9)$$

where the constants for each mirror are given in table 2.2 and x,y and z are given in centimeters and the origin is the center of the target. The positive z axis is along the direction of the beam, the positive x axis points left of the beam and the y axis points up. The location and acceptance of each mirror is given in table 2.3.

The detector designed to be symmetric about reflection across both the x and y axes. The surface equations and locations of the mirrors show these axes of symmetry. The symmetry is important for reducing any false asymmetry from the Mott asymmetry. The Mott asymmetry is a parity conserving asymmetry that is observed when there is a transverse component to the beam polarization, and its contributions are discussed in Section 3.4.

2.6.2 Shielding

Several paths exist for background processes to cause a signal in the phototubes, and different types of shielding are used for each path. Bremsstrahlung radiation from

Table 2.2: Constants for mirror surface equations.

Constants for mirror surface equations. The constants for mirrors 3,6 and 7 are given by substituting $-x$ for x in the equations for mirrors 1,5 and 4 respectively. The equations for mirror 8,9 and 10 are given by substituting $-y$ for y in equations for mirrors 1,2 and 3 respectively.

Constant	Mirror 1	Mirror 2	Mirror 4	Mirror 5
α_0	8744.69	10907.8	9742.28	16133.4
α_1	0.887108	1	0.769435	0.890164
α_2	0.225785	0	0	0
α_3	0.887108	0.884132	1	1
α_4	0.153118	0.122945	0	0
α_5	0.948081	0.967386	0.965362	0.996057
α_6	-0.153118	0.000000	-0.178733	-0.041622
α_7	62.8397	0.000000	94.7888	84.1910
α_8	-62.8397	-71.1017	0	0
α_9	42.6155	37.7222	36.7398	15.9520

Table 2.3: Mirror location and acceptance.

Mirror location and acceptance. θ is measured from the positive z axis. ϕ is measured from the positive z axis, with positive values going towards the the y axis. The L is the length from the center of the target to the center of the mirror. Ω is the solid angle subtended by the mirror. Q^2 is the momentum transfer for an electron scattered from the center of the target to the center of the mirror. The total acceptance of the detector is 1.42 sr.

Mirror	θ(degrees)	ϕ(degrees)	$L(cm)$	$\Omega(sr)$	$Q^2(GeV^2)$
1	145.9	135.8	171.6	0.125	0.100
2	154.0	90.0	151.7	0.170	0.103
3	145.9	171.6	171.6	0.125	0.100
4	138.4	180.0	182.1	0.125	0.097
5	160.5	180.0	153.0	0.164	0.104
6	160.5	0.0	153.0	0.164	0.104
7	138.4	0.0	182.1	0.125	0.097
8	145.9	224.2	171.6	0.125	0.100
9	154.0	270.0	151.7	0.170	0.103
10	145.9	315.8	171.6	0.125	0.100

the electrons losing energy in the target can be backscattered towards the detector. The backscattered photons have an energy spectrum dominated be the 1 — 100 keV region. The phototubes are housed in 10 cm thick lead cylinders open only at the end opposite the target; this lead housing eliminates the direct path from the target to the phototubes. However, the brehmsstrahlung radiation can still cause a signal in the phototubes through scintillation in the air. Previous studies determined that this source of background could be reduced — without significantly degrading the scattered electron signal — by covering the scattering chamber with a 2 mm thick lead sheet [56].

Neutrons from the deuteron are a new source of background for the deuterium experiment. Borated polyethylene shielding was used to reduce this background. Previous studies with hydrogen found that neutron shielding did not reduce the signal, but with a deuteron target neutron shielding reduced the signal in the detector. This indicates that there is a neutron component to the background. An open box of borated polyethylene[2] was constructed between the target and the phototubes; it is six inches thick on the top and bottom and 8 inches thick on the sides. This reduced the dark background by approximately 30%.

2.7 Data Acquisition

The data acquisition system (DAQ) integrates the signal in each detector or monitor, digitizes the integrated voltage and writes the data to disk for each beam pulse. The counting rate, approximately 100 MHz during a beam pulse in each detector segment, is too high to count individual electrons in the main Cerenkov detector; instead the signal is integrated over a beam pulse. The same approach is used for all 40 of the instrumentation channels despite the differences devices read out.

[2]The borated polyethylene is 5% boron by weight

The DAQ system uses a μVAX III running the Q data acquisition system to interface to the CAMAC electronics through a microprogrammable branch driver. The system is substantially the same as that used by the PV elastic electron-carbon scattering experiments performed in the North Hall at Bates [57], [58]. The data acquisition system records every electronics channel for every beam pulse, and puts the data from approximately a third of the beam pulses in online histograms available in real time. The signals recorded include the charge of the pulse at several locations, the position, the halo monitors and all the Cerenkov detector signals. Additional information, including the type of event and the helicity of the beam pulse is also recorded for each pulse. The online histograms are used to monitor beam quality while the recorded data are replayed later to determine the physics asymmetry.

Each channel of electronics is pre-conditioned, integrated, post-conditioned and digitized. The pre-conditioning is necessary because the 16 bit analog to digital converters require a voltage between 0 and positive 5 V. Raw signals from the devices are amplified and inverted as needed to put the integrated signal in the appropriate range on the ADC. The integrator integrates the signal over a 50 μs window that includes the 25 μs beam pulse with a wide margin on either side. The post-conditioning includes adding an offset to signals which could be either positive or negative, and adding the DAC noise to the signal. The DAC noise is part of an anti-aliasing technique described below.

2.7.1 DAC Noise

The ADCs used to digitize the integrated signal suffer from differential non-linearity which could disturb the asymmetry measurements. The slope at any given point on the ADC's range may be different from the average slope of the ADC. The difference reported between voltages which should be only one channel apart can be as large as 50 channels. This non-linearity in the ADCs can magnify the asymmetry measurement,

depending on where the averages for the two helicity states fall on the range of the ADCs. If the individual members of a pulse pair lie on either side of an edge, the asymmetry can be greatly magnified. The effect on the average is lessened if the individual measurements have a large variance, because the effects of the non-linearity are averaged out. The expectation value of the false asymmetry is less than [58]

$$\delta A < \frac{SA}{\sigma} \tag{2.10}$$

where A is the size asymmetry, S is the difference between adjacent channels and σ is the width of the signal in ADC channels.

The DAC noise system reduces the effect of the ADC differential non-linearity by spreading the signal out over many channels on the ADC. This is accomplished using a digital to analog converter (DAC) to add a known, pseudo-randomly chosen voltage between 0 and 0.5 V to each electronics channel. The added DAC voltage is subtracted from the measured value of the electronics channel in software; this allows the false asymmetry from the differential non-linearity to be reduced without increasing the width of the signal. The differential non-linearities can be as large as 50 channels, but the DAC voltage spreads out the signal over 6000 or more channels. This limits the false asymmetry due to the ADC non-linearity to less than 1% of the measured asymmetry in the worst case.

2.8 Pulse Counting

The pulse counting system uses scintillation detectors behind the mirrors to determine how much of the signal in the Cerenkov detectors comes from the scattered electrons. The scintillation detectors detect charged particles and electrons dominate the signal. When the detector is run in pulse counting mode, the current is reduced by a factor of approximately 1000 so that the coincidences between the scintillation detector and Cerenkov detector can be seen. These coincidences are used to determine how much

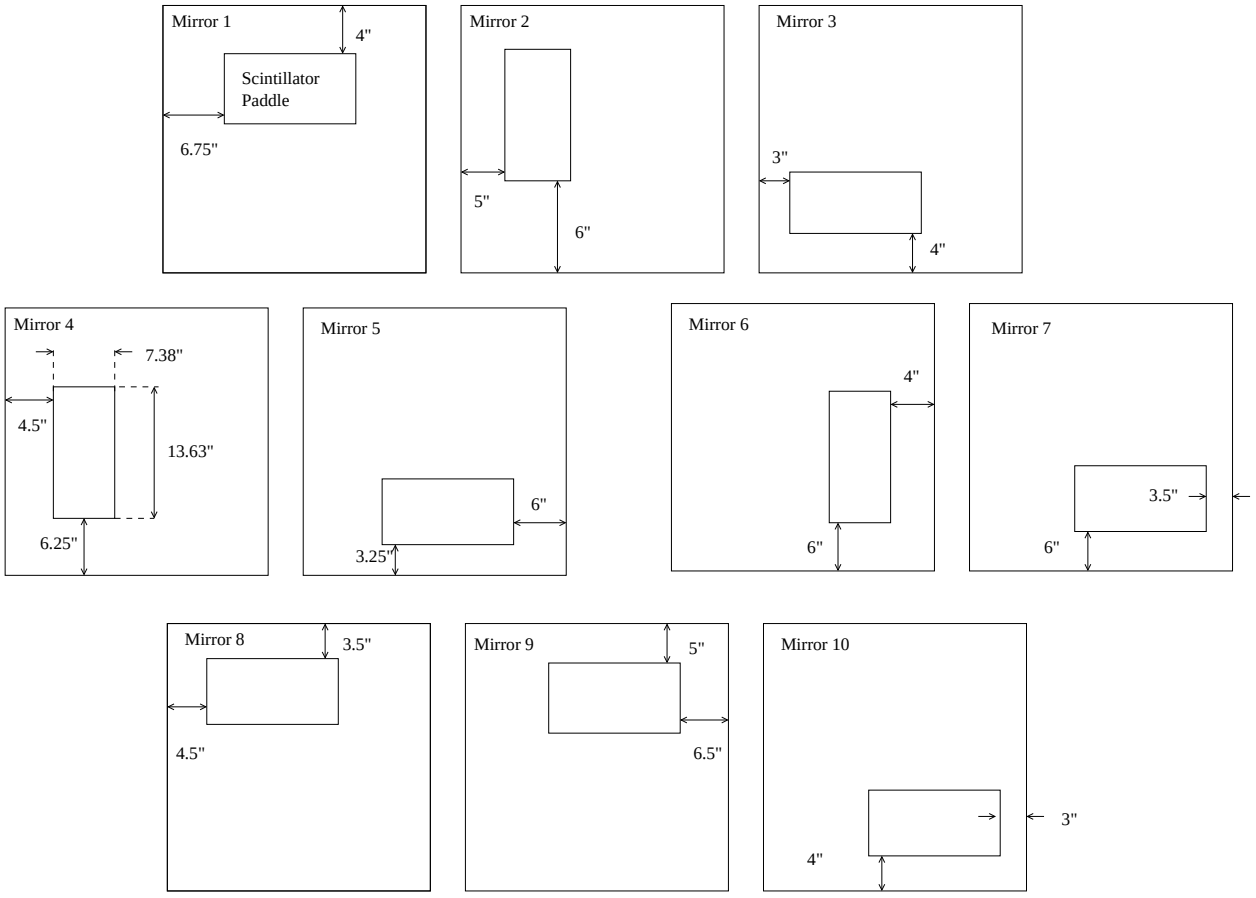

Figure 2.7: Scintillator placement. The locations of the scintillators paddles behind the Cerenkov detectors mirrors is shown.

of signal in the Cerenkov detector comes from electrons emitting Cerenkov light. In addition to the quasi-elastically scattered electrons, electrons can come from pion decays. The electrons from pion decay have enough energy to cause Cerenkov light, allowing them to contribute to the Cerenkov signal determined from pulse counting. The analysis of the pulse counting data and the separation of the pion contribution is discussed in Section 3.2.

The scintillation detectors are paddles are of plastic scintillator $13\frac{5}{8}'' \times 7\frac{3}{8}'' \times \frac{1}{4}''$ optically coupled to 2" phototubes. The detectors are placed behind the mirrors as shown in figure 2.7. The scintillator paddles are all placed far enough away from the edge of the mirrors the all of the Cerenkov light from an electron which hits a scintillator paddle will be reflected to the Cerenkov phototube.

The electronics is set up to record individual events from the detector system using standard NIM and CAMAC electronics read out by a Q system similar to the integration mode system. Analog discriminators can trigger the system to record when either the Cerenkov detector exceeds a certain threshold or both the Cerenkov detector and scintillator detectors exceed their thresholds simultaneously. The former triggers a "singles" event while the latter triggers a "coincidence" event.

The number of singles events triggered is reduced by a scaler so that a comparable number of singles and coincidence events are recorded. This is necessary because the Cerenkov acceptance much larger than the scintillator acceptance. Coincidence events are triggered when the Cerenkov and scintillator events fire within 100 ns of each other. When either kind of event is triggered, the system records all the analog signals. These include the pulse heights in the scintillator and Cerenkov detectors, the time relative to the start of the beam pulse is recorded, and the relative time between the Cerenkov and scintillator pulses. The time between the Cerenkov and scintillator pulses is used to eliminate accidental coincidences from noise while the time relative to the start of the beam pulses is used identify the contribution from electrons resulting from pion decay. In addition to the singles and coincidence triggers, a random trigger is used to generate pedestal events for scintillator and Cerenkov detectors. All of the triggers are gated by the same 50 μs window used to gate the integrators in integration mode, and only one trigger is allowed for each beam pulse. The data recorded by the pulse counting system are summarized in table 2.4.

Scalers are used to keep track of the amount of charge delivered by the beam. A Berkeley Instruments Corporation (BIC) integrator integrates the signal from one of the charge monitors. The output of the BIC integrator is a train of pulses whose frequency is proportional to the beam current. There are two charge scalers, both a gated scaler and an ungated scaler. The gated scaler counts only charge collected while the data acquisition system is ready to be triggered. The ungated scaler counts

Table 2.4: Data recored by pulse counting system.

The analog signals are recorded each time a singles, coincidence or pedestal event is triggered. The scalers are read out periodically.

Name	Description	Type
ceradc	integrated Cerenkov pulse	analog
scinadc1	integrated scintillator pulse	analog
scinadc2	integrated scintillator pulse attenuated by a factor of 3	analog
scinadc3	integrated scintillator pulse attenuated by a factor of 10	analog
evtime	time within the 50 μs beam gate	analog
certdc	time between the triggering of the Cerenkov and scintillator discriminators in a coincidence event	analog
EVENT	triggered singles and coincidence events	scaler
GEVENT	same EVENT but gated by computer live time	scaler
SCINT	scintillator discriminator firings	scaler
SING	Cerenkov discriminator firings	scaler
PSING	pre-scaled Cerenkov discriminator firings	scaler
COIN	coincidence events	scaler
BIC	proportional to total beam charge in beam windows	scaler
GBIC	same as BIC but gated by computer live time	scaler

all of the charge collected in the 50 μs beam gate. Additional scalers count the coincidence and singles event, both gated and ungated.

Chapter 3

Analysis

In an idealized experiment the analysis of the data would be fairly simple. With 100% longitudinal polarization, no helicity correlated beam changes and no background the physics asymmetry would be the same as the measured asymmetry,

$$A_{phys} = A_{meas} = \frac{Y_e^+ - Y_e^-}{Y_e^+ + Y_e^-} \tag{3.1}$$

where $Y_e^{+(-)}$ is the yield due to positive(negative) helicity electrons. In the actual experiment, dilution factors reduce the measured asymmetry by adding a component to the Cerenkov signal that is not correlated with helicity (e.g. backgrounds). Asymmetries in processes other than $e^- - d$ scattering may also contribute to the measured asymmetry.

This chapter discusses the determination of the measured asymmetry and the corrections needed to calculate the physics asymmetry. The physics asymmetry is defined as the asymmetry due to electrons scattered from the deuteron, through quasi-elastic, elastic or inelastic processes. The separation of the quasi-elastic part of the physics asymmetry is discussed in Chapter 4. All of the corrections are determined and applied to the individual mirror segments.

Dilution factors include backgrounds, polarization and electromagnetic radiative effects. There are several types of background that can reduce the measured asym-

metry. These processes which contribute to the total yield in the Cerenkov detector include pion photoproduction, low-energy x-ray scintillation in air, neutron photoproduction and direct low-energy x-ray interaction with the Cerenkov phototubes. The background reduces the asymmetry by about a third, and is discussed in Section 3.2. Radiative effects reduce the energy and polarization of the incident electrons through EM interactions are discussed in Section 3.3. The radiative corrections will be represented in this section by R_c. The beam polarization, P_b, which is just above a third, also reduces the measured asymmetry (see Section 2.4.1). With the addition of these dilution factors, equation 3.1 becomes

$$A_{phys} = \frac{P_b R_c}{f_l f_c (1 - f_\pi)} \times A_{meas} \tag{3.2}$$

where f_l is the fraction of the signal generated by visible light in the detector, f_c is the fraction of f_l that comes from Cerenkov light, and f_π is the fraction of the Cerenkov light which comes from photoproduced pions.

Other processes may add or subtract from the measured asymmetry, including helicity correlated differences in the beam properties. Corrections for helicity correlated beam differences are examined in Section 3.5. A transverse component of the beam polarization — as was present in the first half of the experiment — can generate a parity conserving asymmetry. The magnitude of this parity conserving asymmetry is discussed in Section 3.4. Asymmetries in the photoproduction of pions and neutrons are also discussed in Section 3.2. All of these contributions to the asymmetry are found to be small compared to the statistical uncertainty in the measurement.

3.1 The Measured Asymmetry

This section describes the treatment and selection of the data used for the result. While the experiment is running, all 40 ADCs are read after every beam pulse. One beam pulse and the corresponding set of 40 ADC values are referred to as an event.

Each channel is integrated over the beam pulse and read out by the ADC; the yield measured in a single event in one Cerenkov detector segment includes several thousand scattered electrons from the beam pulse. The data is broken up into files of approximately 2 millions events, collected in approximately an hour of running. Each file is referred to as a "run". The runs are corrected for helicity correlated beam differences individually, and the average asymmetry for each detector segment over a run is a simple average. The average over the experiment is a weighted average of the included runs. For the most part, data that were excluded were associated with identifiable equipment malfunctions.

The relevant data for the analysis of the included runs comprises the ADC values from the ten detector segments and the monitors used for helicity correlated corrections. A small amount of processing is necessary for each channel. The random voltage added to counter the effects of the ADC differential non-linearity is removed. The pedestal, or electronic offset, is also subtracted. A running average is kept for each timeslot over the last twenty pedestal events, or approximately fives seconds. It is this average of the recent pedestal values which is subtracted.

The SLAC-style BPM and the Cerenkov detector signals are proportional to charge in a beam pulse; therefore they are normalized to the charge in the beam in that beam pulse. The BPMs and the Cerenkov detector are normalized with the closest charge monitor. The BPMs NNH1X and NNH1Y are both normalized to the signal in charge monitor STS6. The BPMs NNH2X and NNH2Y, as well as all ten segments of the Cerenkov detector are normalized to the average of the signals in the charge monitors TTG1 and TTG2.

The asymmetries for each channel are calculated for each pair of pulses, and averaged over each run. The average over the run m is simply the sum of the asymmetries divided by the number of asymmetries.

$$\langle A(m) \rangle = \frac{1}{N} \sum_{i=1}^{N} A_i \tag{3.3}$$

where A is the asymmetry in one of the detectors or beam monitors and N is the total number of events in a run. The statistical uncertainty given by the usual formula

$$\sigma_A(m) = \sqrt{\frac{\langle A^2 \rangle - < A >^2}{N}}. \tag{3.4}$$

Because the position and energy monitors can have negative values, a difference rather than an asymmetry is calculated for those monitors; the averages and uncertainties are calculated in the same way. Only data taken under good running conditions is used to calculate the average over the experiment.

The good data are essentially all the data that was taken while all the feedback systems are working properly and the beam is at the correct position and size at the target. The feedback systems implemented at Bates keep the beam stable enough that few cuts are necessary in the data. For the most part the entire run in which a malfunction occurred is excluded. The most common reason for excluding a run is the phase of a transmitter in the linear accelerator drifting far enough that the energy feedback system is not able to compensate for the change. Typically, these runs would be noted at the time of the data taking. Similarly, the intensity asymmetry occasionally exceeds the range of the PITA feedback system, resulting in the exclusion of that run.

The position and size of the beam can also make the background unstable enough that runs must be excluded. The size of the electron beam beam can too large at the target or the centroid can drift near an aperture. When this happens, the background in the Cerenkov detector becomes very sensitive to position changes, which makes the width of the asymmetry distribution larger. In most instances where this occurs, it is noted at the time and the beam is adjusted to fix the problem. A few runs are excluded simply because of anomalously large asymmetry distribution widths, under the assumption that the beam was in the wrong position or too large. Within runs, data is excluded only for dramatic problems with transmission, energy or position.

The average over all of the good runs in the experiment is calculated using the

uncertainty for each run as the weight for each run. The average over the experiment for a single detector segment is given by

$$\langle A \rangle = \frac{\sum_m^{good\ runs} \frac{\langle A(m) \rangle}{\sigma_A^2(m)}}{\sum_m^{good\ runs} \frac{1}{\sigma_A^2(m)}} \tag{3.5}$$

and the uncertainty is given by

$$\sigma_A^2 = \sum_m^{good\ runs} \frac{1}{\sigma_A^2(m)}. \tag{3.6}$$

The combination, of the detector segments to get a single asymmetry for the calculation of $G_A^e(T=1)$ and G_M^s is done after all the corrections are performed for each mirror. The combined physics asymmetry is the average of physics asymmetries for the ten segments with each segment weighted by its statistical uncertainty,

$$A_{phys} = \frac{\sum_i^{10} \frac{A_{phys}^i}{\sigma_{A_{phys}^i}}}{\sum_i^{10} \frac{1}{\sigma_{A_{phys}^i}}} \tag{3.7}$$

with statistical uncertainty

$$\sigma_{A_{phys}}^2 = \left(\sum_i^{10} \frac{1}{\sigma_{A_{phys}^i}} \right)^{-1} \tag{3.8}$$

3.2 Background

Since the Cerenkov detector signal is integrated, separate experiments are needed to determine the fraction of the signal that comes from elastically scattered electrons. When the shutters are closed all of the signal is coming from background processes, and this part of the signal is called the dark signal. The dark signal consists of neutrons and x-rays interacting directly with the phototubes. The remaining part of the total signal, called the light signal consists of the Cerenkov light from scattered electrons, scintillation light from x-rays interacting with the air and Cerenkov light generated from pion decay. The dark background is discussed in Section 3.2.1. Two

different techniques are used to determine how much of the light signal comes from elastically scattered electrons. The first (Section 3.2.2) uses the isotropy of the scintillation light and the detector geometry to determine the elastic fraction of the light from data taken in integration mode. The other method (Section 3.2.3) uses a lower current beam and additional scintillator paddles in order to separate elastic and background contributions by measuring individual events. Problems with the low current charge measurements make the integration method the preferred method for determining f_c, but the method is still useful in the determination of f_π. Measurements and simulations of the pion contribution are discussed in Section 3.2.4

3.2.1 Dark Background

The dark background is the signal in the Cerenkov detector when the shutters are closed. In the deuterium data, it consists of low energy x-rays and neutrons. The neutron signal is the major component of this dark background. Every fourth run is taken with the shutters closed in order to determine the dilution factor from the dark background. The light fraction, f_l, is the dilution factor associated with the dark background; it is defined by

$$f_l \equiv \frac{Y_O - Y_C}{Y_O} \tag{3.9}$$

where Y_O is the yield in a detector segment when the shutter are open and Y_C is the yield in the same detector segment with the shutter closed.

The neutron component can be estimated by comparing the light fractions from the deuterium experiment to the light fraction from the hydrogen experiment. Because of the higher cross section and number density for deuterium, the signal of scattered electrons should be 40 % higher [10]. The electromagnetic background, which comes mainly from backscattered bremsstrahlung, should be very similar for hydrogen and deuterium. If only the EM radiation were considered, the deuterium light fraction would be higher than that for hydrogen. However, even after the neu-

tron shielding was added, the light fraction was significantly lower in the deuterium experiment. The size of the drop in the light fraction indicates that a dominant portion of the dark background is coming from photoproduced neutrons. The parity-violating asymmetry in the photoproduction of neutrons from deuterium has been calculated to be less than 1.5% of the diluted asymmetry we measure; it is small enough to be ignored safely [59]. The asymmetry measured during the closed runs is also consistent with zero.

3.2.2 Cerenkov Fraction of the Light from Integration Data

This method of determining the Cerenkov fraction of the light recorded in our detector depends on the spatial distribution of the origins of the Cerenkov and scintillation light. The scattered electrons are detected by their Cerenkov light, emitted in a narrow cone around the electron's path. Because the electron scattering events takes place only in the target, the origin of all Cerenkov light can be taken to be in the target. The only path which will allow signal from electrons scattered from the target to get into the a detector phototube is reflection off of the associated mirror. The same argument holds for electrons generated from the pion background, which are generated in or near the target and contribute through Cerenkov radiation.

In contrast, the scintillation component of the light originates from points distributed about throughout the detector hut. X-rays excite molecules in the air, which emit scintillation light isotropically. Scintillation light is reflected into each phototube from all ten mirrors, as well as reaching phototubes without reflecting off of any mirror. When one mirror is covered, the signal is entirely eliminated in the associated detector segment, but only a portion of the background is eliminated. In order to estimate the signal to background ratio, only the ratio of this blocked portion to the unblocked portion must be simulated.

Using this framework, the light in detector i is given by

$$L_i^{total} = L_i^{Cerenkov,i} + \sum_{j=1}^{10} L_i^{scint,j} + L_i^{scint,direct} \tag{3.10}$$

where $L_i^{Cerenkov,i}$ is the Cerenkov light reflected from mirror i to detector phototube i, $L_i^{scint,j}$ is the scintillation light reflected off of mirror j into detector phototube i, and $L_i^{scint,direct}$ is the scintillation light which intersects detector phototube i without reflecting off of any surface. By blocking off mirror i, the Cerenkov light, $L_i^{Cerenkov,i}$, and scintillation light reflected from mirror i, $L_i^{scint,i}$, are eliminated, but everything else remains unchanged. This remaining the light in detector segment i when mirror i is covered is given by

$$L_i^{covered} = \sum_{j=1,j\neq i}^{10} L_i^{scint,j} + L_i^{scint,direct} \tag{3.11}$$

The direct scintillation light ,$L_i^{scint,direct}$, can be measured by covering all the mirrors simultaneously.

Then, in principle, the Cerenkov fraction of the signal in mirror i is given by

$$f_{c,i} = \frac{L_i^{total} - L_{i,sim}^{scint,i} - L_i^{covered}}{L_i^{total}} \tag{3.12}$$

where $L_{i,sim}^{scint,i}$ is the scintillation light reflected by mirror i into its own phototube. Since the reflected Cerenkov light and the reflected scintillation light cannot be separated in measurements, $L_{i,sim}^{scint,i}$ must be determined by simulation. It is only necessary to simulate the ratio of light reflected from the different mirrors, since the reflected scintillation light from the other mirrors, L_i^{other}, can be measured.

Covered Mirror Measurements

In practice, it is too time consuming to cover one mirror at a time, so groups of mirrors are covered simultaneously, as shown in Figure 3.1. With this approach, the ratio of scintillation light reflected into a given phototube by the simultaneously covered

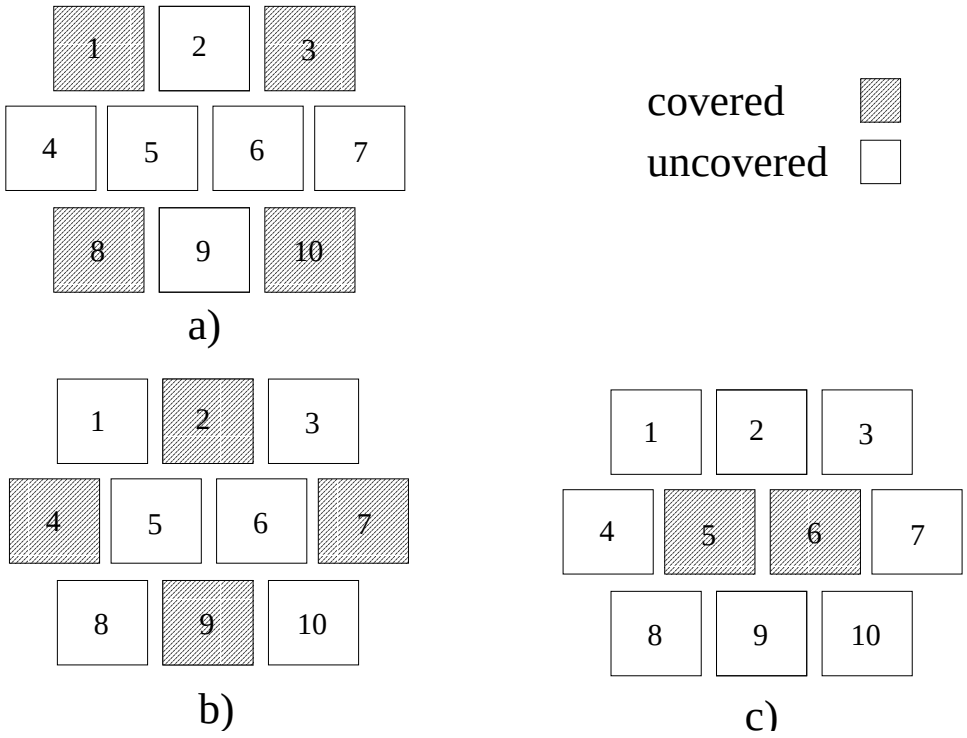

Figure 3.1: Mirror cover configurations. The groups shown are covered simultaneously for the determination of the Cerenkov fraction of the light. Set a) contains mirrors 1,3,8 and 10. Set b) contains mirrors 2,4,7 and 9. Set c) contains mirrors 5 and 6.

mirrors to that reflected by the other mirrors must be determined by simulation. The definition of a detector segment's own light is expanded to include the contribution from all the mirrors in its own set,

$$L_i^{own} = L_i^{Cerenkov} + L_i^{scintillation} \tag{3.13}$$

where $L^{Cerenkov}$ is the contribution from Cerenkov light and $L^{scintillation}$ is scintillation light from all of the members of the segment's own set. L_i^{own} is measured by taking the difference between the light signal in phototube i when all mirrors are uncovered and when the mirrors in segment i's set are covered. The light reflected by mirrors outside the detector's own set is called L_i^{other}, and it is measured by taking the difference in phototube i's signal when all the mirrors are covered as opposed to only the mirrors in i's set. For example, L_1^{own} is measured by taking the difference between the signal in phototube 1 when all mirrors are uncovered and mirrors 1,3,8, and 10 are covered. L_1^{other} is the difference in the signal when mirrors 1,3,8 and 10 are covered and when all mirrors are covered.

The elastic fraction for detector segment i is given by

$$f_{c,i} = \frac{L_i^{own} - \alpha_i L_i^{other}}{L_i^{total}} \tag{3.14}$$

where L_i^{total} is the total light signal in a tube with all mirror uncovered and α_i is the ratio of $L_i^{scintillation}$ to L_i^{other}

In order to calculate the the ratio of the own scintillation light to the other scintillation light, a simple ray tracing program is used in combination with GEANT output. The GEANT simulation gives the position of energy deposition in air. The ray tracing program generates scintillation isotropically from those points and tabulates how much scintillation light is reflected from each mirror onto the phototube.

The GEANT simulation is the same one used for generating the background estimates for the 120 MeV proposal [60]. The simulation starts with an electron beam incident on the target. The electrons emit bremsstrahlung radiation in the target,

which is Compton scattered back into the detector volume. The backscattered photons are propagated into the air in the detector hut where the position and magnitude of energy deposition in air are recorded.

The ray tracing program uses the position and energies recorded by GEANT to generate scintillation light. The scattering chamber surrounding the detector, the mirrors, the phototubes and their lead shielding are the only elements included in the ray tracing program. The mirror surfaces are given by the Eq. 2.9 and Table 2.2. The estimate of the uncertainty comes from assuming the calculation of the own scintillation light could be off by as much as the other scintillation light. The results of the mirror cover studies are shown in Table 3.1.

3.2.3 Cerenkov Fraction of the Light from Pulse Counting

This approach to determining the elastic fraction of the signal uses a lower beam current and additional detector elements. The additional detector elements are scintillator paddles placed behind each mirror. The scintillator paddles detect charged particles, and a coincidence between the Cerenkov and scintillation detectors indicates an electron or a positron caused the event (as opposed to a photon or a neutron). By comparing the coincidence and singles spectra of the Cerenkov detector, the elastic fraction can be determined. The traditional counting experiment tasks of determining the acceptance and dead-time must be performed. As in the mirror cover method, the pion contribution is not separated from the electron scattering contribution in the determination of the Cerenkov fraction. The next section deals with separating the pions.

At the normal current for the experiment the counting rate during a beam pulse is approximately 100 MHz, far too fast for the detectors to distinguish individual electron scattering or x-ray scintillation events. In order to perform the counting experiment, the current is lowered by factor of a 1000. This is done by misaligning

Table 3.1: Results of mirror cover study.

α is the ratio of scintillation light reflected by members of a detector segments own set to L^{other}. L^{own} is all the light reflected into a segment's phototube by mirrors in its set, including the Cerenkov light. L^{other} is the light reflected into a phototube by mirrors outside its set. L^{direct} is the scintillation light hitting a phototube when all the mirrors are covered. f_c is the fraction of the light due to Cerenkov light, including the pion contribution.

Mirror	α	L^{own}	L^{other}	L^{direct}	f_c
1	2.7	360	7	10	0.905 ± 0.02
2	0.84	259	8	15	0.895 ± 0.03
3	2.7	278	7	12	0.872 ± 0.03
4	1.3	310	10	8	0.895 ± 0.03
5	.114	216	5	8	0.941 ± 0.02
6	.114	176	4	8	0.929 ± 0.02
7	1.3	268	8	10	0.901 ± 0.03
8	2.7	260	7	14	0.858 ± 0.03
9	0.84	295	10	20	0.882 ± 0.03
10	2.7	388	7	15	0.900 ± 0.02

the linear polarizer after the shutter Pockels cell so that the desired current for the pulse counting measurement is coming from the electron gun when the shutter is in the "off" position. This low current beam is too small to be accurately measured by the beam line instrumentation. In order to monitor the accelerator tune in real time, the shutter is switched to its "on" position for one out of every ten beam pulses; this provides "tracer bullets" to monitor the beam tune. The laser intensity is set so that the current in the tracer bullets is approximately 25 times larger than the pulse counting beam pulses. This current is low enough that the beam loading effects are minimal in the tracer bullets, as they are in the pulse counting beam pulses. These pulses are vetoed by the pulse counting system, but are included in the online integration mode monitoring system.

The pulse counting experiment can be broken down in to several tasks. Coincidences between the Cerenkov detector and scintillator paddle must be identified, and accidental coincidences must be subtracted. The singles spectrum must be formed and corrected for dark processes, including dark background and phototube noise. Finally the singles and coincidence spectra must be normalized to each other, and their ratio determined.

Coincidence events are events in which the scintillator and Cerenkov detector fire close together in time. The pulse heights for the two tubes and the time between their firing, the coincidence time, are recorded. This is important for eliminating accidental coincidences. The real coincidence events have approximately the same coincidence time, but the accidental coincidence events are evenly distributed in coincidence time. By selecting events near the peak of the coincidence time histogram to make the Cerenkov pulse height spectra, most of the accidental coincidences can be excluded. The remaining contribution from accidental coincidences is removed by subtracting a Cerenkov pulse height spectra for the accidental coincidences, which are also identified by their coincidence times.

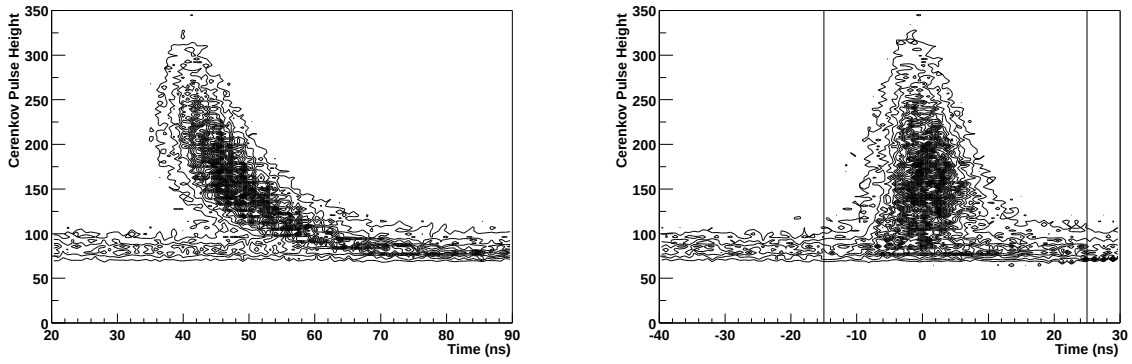

a) b)

Figure 3.2: Coincidence and pulse height. a) Uncorrected plot of Cerenkov pulse height vs. coincidence time. The curved dense region of points shows the skewing of the coincidence time by the effect of the pulse height on the discriminators. The accidental coincidences are spread around the base of the plot. b) The corrected plot of Cerenkov pulse height vs coincidence time.The selection for accidental coincidences is between the dashed lines and the selection for coincidences is between the solid lines.

This process is complicated by the constant height discriminators used to determining the timing of the Cerenkov events. Events with a high number of photoelectrons are recorded sooner, because of the steeper slope of the pulse (the "walk" of the leading edge discriminator). This can be seen in Figure 3.2a. In order to obtain a cleaner spectrum, the coincidence time is corrected for the effects the Cerenkov pulse height. The two dimensional histogram in Figure 3.2.a is divided into many one dimensional time histograms, and the peaks of those histograms are fit to a polynomial. The events for the coincidence and accidental coincidence Cerenkov pulse height spectra are selected from their corrected coincidence time.

The singles Cerenkov spectrum is formed by making a histogram of the Cerenkov pulse heights when only the Cerenkov discriminator was triggered. The sources of signal for the open shutter Cerenkov singles spectra are Cerenkov light, scintillation light, dark background and phototube noise. Before the singles and coincidence spectra are compared to get the light fraction, a shutter closed singles spectrum is subtracted from the shutter open spectrum. This removes the effect of the dark background processes, allowing the determination of the Cerenkov fraction of the light.

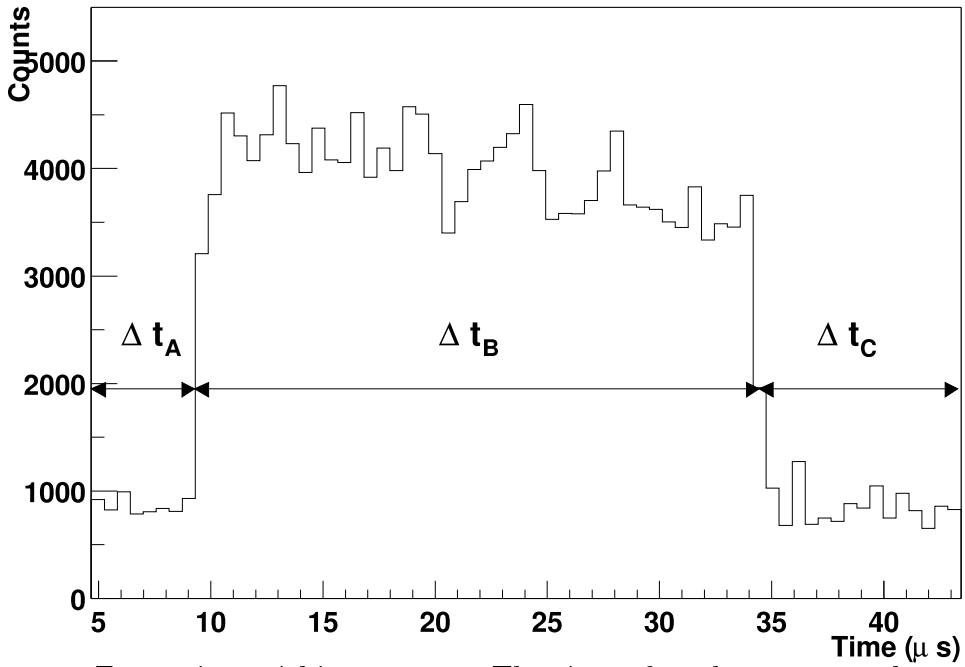

Figure 3.3: Event time within run gate. The time after the run gate that an event occurs. Both coincidence and singles events are shown. The time indicated by Δt_A is the time before the beam turns on, Δt_B is the time the beam is on and Δt_C is the time after the beam turns off and before the run gate is off.

This would also properly account for the phototube noise, except for the effect of the detector dead time.

The dead time is an issue because of the way events are recorded. During each 50 μs run gate only the first event is recorded. Therefore, if events occurred at a constant rate the number of events would drop off exponentially as the time from the beginning of the run gate increased. An example of the beam structure within the run gate can be seen in Figure 3.3. Events in region A are all phototube noise. The singles spectra is formed from events in regions B and C. The rate at which phototube noise events contribute to the singles spectrum is suppressed in region B by the dead time. To calculate the suppression, the integral of the live time over the region of interest is calculated and divided by the total time of the region of interest [61]. The contribution to the dead time from times when the beam is off is negligible; only the decay rate of the live time during the time the beam is on is needed. This decay rate, λ, can be obtained satisfactorily from the number of recorded events. The

normalization for the noise spectrum is given by

$$\frac{\Delta t_A}{\Delta t_B + \Delta t_C}\left(\int_0^{\Delta t_B} e^{-\lambda t} dt + \Delta t_C e^{-\lambda \Delta t_B}\right) \tag{3.15}$$

where Δt_B is the total time that beam is on and $\Delta t_{A(C)}$ is the time the before(after) the beam gate is on. With this normalization, the phototube noise spectrum can be subtracted from the singles spectrum.

Data is taken with the phototube shutter open and closed, in order to be able to determine how much of the signal is coming from light. In principle, this also allows a comparison between the light fraction as measured by the pulse counting experiment and the light fraction measured by the integration mode experiment. The spectra must be normalized by the beam charge during the run before the subtraction. Unfortunately the charge monitor was apparently not accurate enough at the low currents used for the pulse counting experiment. The integrator used for measuring the charge has an offset which drifts with time at the levels which can be significant to the pulse counting measurement.

The combination of the singles and coincidence spectra requires one more scaling, since the acceptance of the scintillator does not match the acceptance of Cerenkov detector. The acceptance for coincidence events is smaller because the scintillator paddle is smaller than that of the mirror. In addition, the coincidence spectrum is missing some low photoelectron events because only events in which the electron strikes the scintillator are counted. This is to be contrasted with the singles spectrum where events with the electron just missing the mirror contribute the low photoelectron events to the Cerenkov signal. This effect is called the mirror edge effect.

The scaling to account for the size difference between the detectors is done by using the region from 4 to 10 photoelectrons in the Cerenkov pulse height spectra. The high PE events come from Cerenkov events. Ignoring the small mirror edge effect, this region should be the same for both the coincidence and singles spectra. A typical result of the scaling is shown in Figure 3.4.

The Cerenkov fraction of the light is given by

$$f_c = \frac{\sum_i PE_i^c \, N_i^c}{\sum_i PE_i^s \, N_i^s} \tag{3.16}$$

where $PE_i^{c(s)}$ is the number of photoelectrons for bin i of the coincidence(singles) histogram and $N_i^{c(s)}$ is the number of counts.

The mirror edge effect is addressed with a simulation of the Cerenkov light and the phototube response. In this simulation, cones of Cerenkov photons are generated with a uniform distribution over an area larger than the mirror. Spectra including all the Cerenkov photons which strike the mirror and spectra including only the photons from electrons which struck the mirror are generated. The simulated spectra with the edge effect closely match the coincidence spectra. Based on the comparison of the total number of photoelectrons in the spectra with the edge effect to spectra without the edge effect, a correction factor of 1.05 is applied to the pulse counting result [62]. The results, multiplied by the edge effect are shown in Table 3.2

The systematic error in this method of measuring the Cerenkov fraction of the light can be estimated by comparing the measurements of the light fraction from the pulse counting data to the integration mode light fraction measurements. In the pulse counting data, the light fraction is given by

$$f_{light}^{PC} = 1 - \frac{PE_i^{s,closed} \, N_i}{PE_i^{s,open} \, N_i} \tag{3.17}$$

where $PE_i^{s,closed(open)}$ is the number of photoelectrons in a bin of closed (open) singles Cerenkov pulse height spectra. The main sources of potential error in this measurement come from differences between the low current beam and the high current beam and difficulties in charge normalization. Both of these problems would be evident in the measurement of the light ratio. Because of the degree of disagreement between the light fraction from the pulse counting and integration modes, the systematic error in the determination of f_c may be as large as fifteen percent. Because of this large

Table 3.2: Results of pulse counting studies.

f_c is the fraction of the light that comes from Cerenkov radiation, including the pion background (see Section 3.2.4). $f_{light}^{PC(integration)}$ is the fraction of the total yield in the Cerenkov detector coming from light as measured in the pulse counting(integration) mode. The uncertainties for f_c and f_{light}^{PC} are statistical only. The disparity between the pulse counting and integration mode light fractions for many detector segments is the reason integration mode method of determining f_c is preferred.

Mirror	f_c	f_{light}^{PC}	$f_{light}^{integration}$
1	0.85 ± 0.04	0.93 ± 0.04	0.74
2	0.86 ± 0.04	0.75 ± 0.03	0.61
3	0.95 ± 0.04	0.84 ± 0.02	0.74
4	0.88 ± 0.03	0.95 ± 0.02	0.74
5	0.79 ± 0.07	0.58 ± 0.04	0.47
6	0.83 ± 0.10	0.66 ± 0.07	0.47
7	0.52 ± 0.04	1.22 ± 0.06	0.72
8	0.79 ± 0.06	0.97 ± 0.06	0.73
9	0.76 ± 0.05	0.81 ± 0.05	0.63
10	0.87 ± 0.06	1.02 ± 0.05	0.74

systematic error, the integration mode method of determining the Cerenkov fraction is used for calculating the results. However, the pulse counting data and much of the work of the analysis can be used in the determination of part of the pion contribution.

3.2.4 Pions

A 200 MeV electron has enough energy to produce pions in the target through electroproduction and photoproduction, and their contribution to the background must be determined. The pions ultimately produce a signal in the Cerenkov detector which

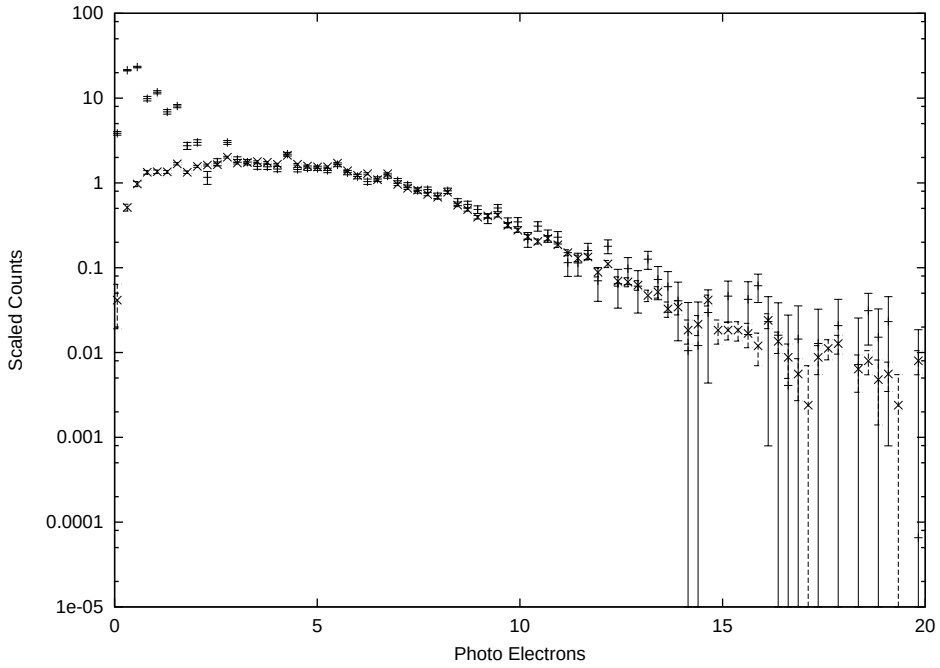

Figure 3.4: Scaled singles and coincidence Cerenkov pulse height spectra. The ratio of the number of photoelectrons in the coincidence spectra ($\times$) to the singles spectra ($+$) give the elastic fraction. The region between 4 and 10 photoelectrons is used to scale the spectra.

looks much like the scattered electron signal. The π^+,π^0 and π^- are all made in $e^- - d$ scattering. Each pion channel makes electrons above the 20 MeV Cerenkov threshold, but in different ways. The decay pathways are illustrated in Figure 3.5. The π^+ contribution can be measured because it proceeds by the relatively slow decay of the μ, which allows this contribution to be found in the time after the beam has turned off. The π^0 and π^- contributions are indistinguishable from the quasi-elastically scattered electrons in our apparatus and must be simulated.

π^+ Measurement

All of the pion channels produce electrons with energies above the Cerenkov threshold and a spatial distribution similar to the quasi-elastically scattered electrons. The π^+ channel is distinguishable in experiment because the μ^+ has a mean lifetime of 2.2 μs, which is slow enough that the exponential decay of the signal can be seen

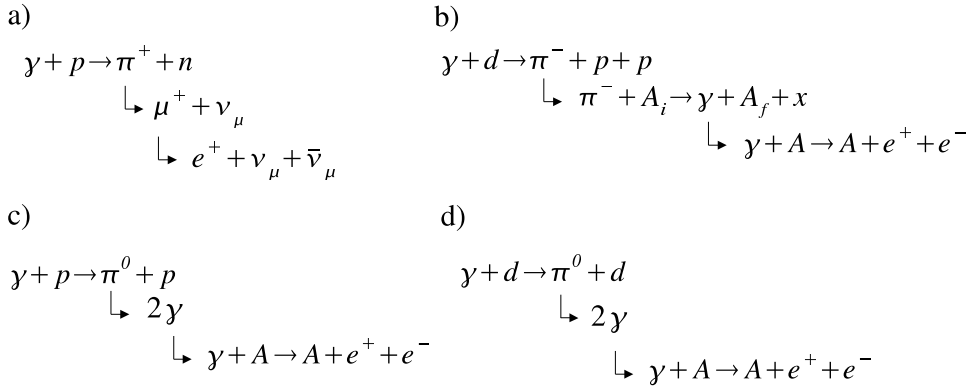

Figure 3.5: Pion contribution paths. a) Photoproduction of the π^+ on the proton, which contributes through the decay of the μ^+ to a positron. b) Photoproduction of π^- on the neutron, which contributes through pair conversion of the γ from radiative capture of the π^- on a nucleus (A). c) and d) The π^0 channels contribute through the pair conversion of the decay photons.

at the end of an electron beam pulse. As shown in Figure 3.5a, the π^+ decays overwhelmingly to a muon and a neutrino. The positrons produced in the μ^+ decay have a maximum energy of 53 MeV and make Cerenkov radiation seen by the detector. The muons decay in or close to the target which makes the spatial distribution of the electrons produced from the pions similar to the distribution of quasi-elastically scattered electrons.

The pulse counting data is used to fit the exponential decay of the π^+ signal after the beam pulse ends. Coincidence events are plotted as a function of EVTIME, the time the event occurred within the beam gate. Accidental coincidences are reduced by cutting on the corrected time between Cerenkov and scintillator triggers, CERTDC and the scintillator pulse height, SCINADC. The cut on CERTDC is the same as the cut shown in figure 3.2. The cut on the scintillator pulse height reduces accidental coincidences from the noise on the scintillator phototube.

The EVTIME histogram without the contribution of π^+ events would have a sharp rise at the start of the beam pulse and a sharp fall at the end. Because of dead time, the high rate period while the beam is on exhibits a shallow exponential decay. The contribution from pions is seen in the small exponentially decreasing tail after the

sharp drop at the end of the beam pulse. This tail is fit to the expression

$$r(t) = A \times \exp^{-t/\tau} + B \tag{3.18}$$

where t is the time after the electron beam pulse ended, A is the steady state rate of pion events, B is the accidental rate and τ is the mean lifetime of the muon, 2.2 μs. The parameters A and B are determined by fitting the region with $t > 0$. The fractional π^+ rate is given by the ratio of A to the steady state rate during the beam pulse. Only the last several microseconds of the beam pulse are used for the comparison because of the dead time issue. The average result for the ten mirrors is a rate of $r_{\pi^+} = 1.8 \pm 0.2 \pm 0.2\%$, where the first uncertainty is statistical and the second error is systematic. The systematic uncertainty comes from the estimated accuracy of the identification of the end of the beam pulse. Figure 3.6 shows the data for a single mirror and the corresponding fit. In order to determine the contribution of the pions to the Cerenkov signal, the ratio of the average number of photoelectrons per pion event to the average number of pions per scattering event must be determined. In the runs with the smallest accidental rate, the average number of photoelectrons per pion event is between 0.5 and 0.8 the average in the scattering events. The small number of pion events makes this ratio difficult to measure, and its uncertainty dominates the uncertainty in the experimental determination of the π^+ contribution, which is given by $f_{\pi^+} = 1.2 \pm 0.3\%$.

Simulation

The contributions from the π^0 and π^- channels are indistinguishable with our apparatus because there is no slow step in the process that leading to electron or positron creation. These contributions must be simulated. The π^+ contribution is also simulated as a cross-check.

The simulation uses GEANT 3 to calculate the contribution of pions, with additional code added to account for production of pions on deuterium and described

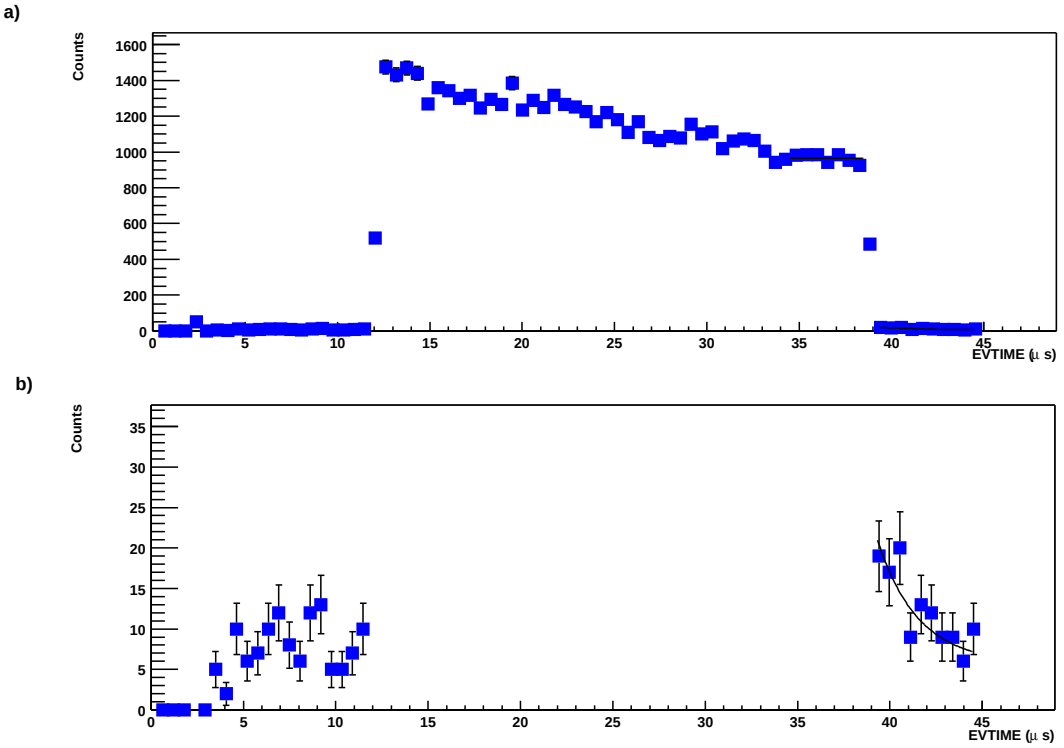

Figure 3.6: Data from a single run for detector segment nine. a) The EVTIME histogram for the coincidence events. b) The same data with an expanded scale. The solid line is the fit to the pion decay plus accidental background.

further below [63]. In the simulation photons with momenta along the electron beam direction interact with deuterons in the target. The electroproduction is handled at the same time as photoproduction through the inclusion of virtual photons. When the photon interacts with a nucleon within the deuteron, a random momentum is assigned to the nucleon according to a y-scaling model. The electrons which ultimately result are tracked, and their contribution is weighted according to their Cerenkov production efficiency. The fraction of the Cerenkov light that comes from pions is calculated by comparing the pion contribution to the sum of the pion, quasi-elastic, threshold disintegration and elastic scattering contributions.

Data is available for the photoproduction of the π^+ on the deuteron and the π^0 on the deuteron and proton from Bergstrom *et al.*[64][65][66]. Their cross sections are used in the GEANT simulation to generate the π^+ and π^0 events. The π^+ is followed through its decay pathway to a positrons through a μ^+. The π^0's decay into a pair of gamma rays, which can pair convert to electrons and positrons in the target and surrounding material.

The cross section for the photoproduction of the π^- on a neutron is calculated, and its contribution proceeds through a different path. The calculation done with MAID2000, a unitary isobar model for pion production [67]. The calculation is necessary because there is not sufficient appropriate data for π^- photoproduction on neutrons. The π^- can decay to a muon and a neutrino, but the cross section for capture of the π^- on nuclei is so high that the decay to a muon does not contribute significantly. It is the radiative capture which ultimately contributes to the Cerenkov signal. When a π^- is radiatively captured, a γ with the energy of the pion is emitted. The capture can occur in the deuteron target, the aluminum target cell, the scattering chamber or the lead shielding surrounding the scattering chamber. Most of the π^-'s stop in the the cell, the scattering chamber or the lead shield. The branching ratio for radiative capture on these heavier nuclei is .02. A small fraction of the π^-'s stop

in the deuteron target, where the branching ratio is much higher, 25% [68]. In either case, the γ can pair convert near the target.

Results

The results from the simulation are used to determine the dilution of the physics asymmetry from pions. The contribution from each pion channel is summed to get the total contribution. Table 3.3 lists the pion contributions by mirror type and pion channel, as well as the dilution factor. The net effect is an eight percent reduction in the measured asymmetry compared to the physics asymmetry. The uncertainty in the pion dilution factor is estimated to be 2% because of the lack of data for the π^0 channel.

In addition to the dilution effect, a PV asymmetry in pion production would introduce a contaminating asymmetry. Calculations of asymmetries in pion photoproduction and electroproduction on the proton indicate that this false asymmetry will not be significant [69][70]. The asymmetry in both electroproduction and photoproduction is found to be less than $2.5 \times 10^{-}7$ at the kinematics relevant to SAMPLE. Asymmetries in the other pion production channels are not expected expected to be larger. Assuming this is the case, the relatively small contribution from pion production makes the contaminating asymmetry negligible.

3.3 Radiative Corrections

The radiative corrections are necessary to account for electromagnetic interactions between the electrons and the target nuclei. Bremsstrahlung radiation from the electron before the the electron is scattered into the detector reduces the incident energy, through the emission of real or virtual photons. Additionally, the electromagnetic interactions can flip the polarization of the incident electron, causing a net depolar-

Table 3.3: Pion dilution factors.

The simulated contributions of the three pion channels to the signal in the Cerenkov detector is broken down by the mirror groups. The pion fractions f_{π^+},f_{π^0} and f_{π^-} are the ratios of the π^+,π^0 and π^- to the total Cerenkov contribution. The total pion fraction of the Cerenkov signal is given by f_π. The dilution factor is given by $\frac{1}{1-f_\pi}$.

Mirrors	f_{π^+}	f_{π^0}	f_{π^-}	f_π	$\frac{1}{1-f_\pi}$
1,3,8,10	.0124	.0552	.0109	.0785	1.085
2,9	.0089	.0526	.0146	.0761	1.082
4,7	.0119	.0489	.0087	.0694	1.075
5,6	.0073	.0446	.0067	.0670	1.072

ization.

The calculation of the effect of electromagnetic radiative corrections on the measured deuteron asymmetry is based on a simulation by D. Spayde to calculate the same effects for the hydrogen experiment [48]. The simulation was modified to account for additional processes in scattering from the deuteron. These included cross sections and asymmetries for quasi-elastic scattering, threshold breakup and elastic scattering [63]. The calculated asymmetry for electrons scattered from the deuteron includes the asymmetry from three processes

$$A_d = \frac{A_{QE}\sigma_{QE} + A_{TD}\sigma_{TD} + A_E\sigma_E}{\sigma_{QE} + \sigma_{TD} + \sigma_E} \tag{3.19}$$

where A_{QE}, A_{TD} and A_E respectively represent the asymmetry in quasi-elastic scattering, threshold disintegration, and elastic scattering; and σ_{QE}, σ_{TD}, and σ_E represent the cross section for the same process. The full nuclear calculations used in Section 4.1 to extract the single nucleon form factors are not used in the radiative corrections; here the QE and threshold breakup processes are handled separately. The radiative correction is the ratio of the calculated deuteron asymmetry with the

Table 3.4: Electromagnetic radiative corrections.

The radiative correction, R_c, is the ratio of the asymmetry from the deuteron calculated with the electromagnetic corrections (e.g. bremsstrahlung) to the asymmetry calculated without radiative corrections.

Mirrors	R_c
1,3,8,10	1.116
2,9	1.092
4,7	1.158
5,6	1.068

electromagnetic corrections turned included to the calculated asymmetry with the electromagnetic corrections turned off. The radiative correction is calculated for each type of mirror. Table 3.4 shows the results.

3.4 Transverse Polarization

A transverse polarization component can lead to a parity-conserving (PC) asymmetry in electrons scattered from the target. This azimuthal asymmetry from transverse beam polarization will can cause an asymmetry in individual detector segments, but will average out in symmetric pairs of detectors. The asymmetry is similar to the Mott asymmetry, which describes the asymmetry when transversely polarized electrons are scattered from a spin zero nucleus. In the rest frame of an incident electron, the current due to the charge of a nucleus will generate a magnetic field. The left-right parity-conserving asymmetry arises from the interaction of the transverse spin of the electron with this magnetic field; when the electron energy is large the asymmetry is given by [71]

$$A_{Mott} = -\frac{4Z\alpha\beta}{\gamma}\frac{\csc\theta\ln(csc\theta/2)}{\cos^2\theta/2} \tag{3.20}$$

where Z is the charge of the nucleus, α is the electromagnetic fine structure constant, β and γ are used in the usual sense of relativistic kinematics, and θ is the scattering angle in the lab frame. In the SAMPLE experiment, quasi-elastic scattering from the proton and neutron in the deuteron dominate and the interaction of the spin of the electron with the spin of the nucleon will also contribute to the asymmetry. Because calculations of this "spin-$\frac{1}{2}$ Mott asymmetry" are not available, the calculation of the size of the effect on the SAMPLE result is based on a measurement of the magnitude of the asymmetry which is combined with estimates of the angular dependence of the asymmetry and the degree of symmetry in the detector.

The degree to which the spin-$\frac{1}{2}$ Mott asymmetry affects the results is proportional to the magnitude of the transverse polarization. Approximately half way though the run, a significant transverse polarization was discovered and corrected. The net rotation of the spin by the solenoids before the Møller polarimeter, ϕ, was found to be 34.7° at run 2284. From equation 2.4, the transverse component is found to be $\frac{|P_T|}{|P_B|} = 0.170 \pm 0.019$, where P_T is the polarization in the transverse direction and P_B is the magnitude of the polarization. The solenoid settings were corrected for runs after 2284, and ϕ was confirmed to be close to zero at the end of the runs. Approximately half the data were taken before the solenoid settings were corrected.

The mean value of the spin-$\frac{1}{2}$ Mott asymmetry over the acceptance of the detector was measured for scattering from the deuteron. Sixteen hours of data were taken with the Wien filter set to 106.57° and ϕ set to zero, which makes the the beam polarization transverse and in the horizontal plane at the target. The asymmetry seen in each detector segment is expected to vary sinusoidally with the azimuthal angle of the detector segment. The magnitude of the asymmetry is determined by fitting the individual mirror asymmetries to the function

$$A(\phi_D) = A_{Mott} \sin(\phi_D + \epsilon) \tag{3.21}$$

where ϕ_D is the azimuthal angle of a detector segment. The magnitude of the asym-

metry, A_{Mott}, and the phase, ϵ, are determined by the fit. The result of the fit is $A_{Mott} = 10.5 \pm 8.9$ ppm, where the uncertainty is statistical. This procedure is similar to that used in the measurement of the same PC asymmetry from a proton target, performed with the SAMPLE apparatus to investigate the double photon exchange amplitudes in 1998 [72]. This PC asymmetry in $e^- - p$ scattering was found to be 15.4 ± 5.4 ppm.

The degree to which the PC asymmetry contributes to the measured asymmetry from the detector as a whole depends on both the angular dependence of the PC asymmetry and the degree of symmetry in the detector. The variation of PC asymmetry in scattering from the deuteron with the scattering angle θ cannot be measured with our detector in a reasonable amount of time, and the dependence on the scattering angle is not known theoretically. The angular dependence is estimated by changing the Mott cross section in the denominator of equation 3.20 to the Rosenbluth formula for scattering from the proton or neutron. The extent to which the PC asymmetry is reflected in the average from a symmetric pair of segments depends on how different the average scattering angle is for the two mirrors. Considering the overall construction tolerances — including a possible five percent difference in reflectivity across the mirror surface — the average scattering angle symmetric mirror pairs should differ by less than half a degree. Given the angular dependence of the PC asymmetry described above and the scattering angles the SAMPLE detector covers, the average of a "symmetric" pair of mirrors would fail to cancel no more than two percent of the PC asymmetry due to the transverse beam polarization.

The combination of the measurement of the PC asymmetry, the transverse polarization and the estimate of the degree to which the PC asymmetry will be reflected in the detector as whole indicates that the false asymmetry from the transverse component of the beam polarization will be much smaller than the statistical error. The

magnitude of the false asymmetry is given by

$$|A_{false}| = A_{Mott} \times \frac{|P_T|}{|P_B|} \times D \approx 0.1 ppm \tag{3.22}$$

when $A_{Mott} = 19.4$ ppm, one standard deviation larger than the value measured in the completely transverse running; $\frac{|P_T|}{|P_B|} = 0.170$, the value measured half way through the experiment; and D is the amount of the PC asymmetry not canceled in symmetric pairs, estimated above as $D = 0.02$. The magnitude of this asymmetry is small enough that it should not significantly affect our result.

3.5 Helicity Correlated Beam Difference Corrections

It is possible for the polarized beam to have helicity-correlated beam properties as discussed in section 3.1. For example, differences in the linear polarization of the laser light, originating in the HPC, can lead to charge differences which, in turn, via beam loading in the accelerator and chromatic effects in the transport optics can lead to helicity-correlated energy and position differences, respectively. A linear model of the response of the detector to beam differences is used to correct for these small helicity correlated differences. Whereas these helicity-correlated effects could be very difficult to deal with, in this measurement they are quite small; the correction and its uncertainty are comparable in size to the systematic error from the signal to background determination and the absolute polarization measurement.

The slope of the detector yield with each parameter is determined for each run through the use of multiple linear regression. Position, angle and beam charge at the target, as well as the beam energy are included in the corrections. Two methods are used to determine the response of the detector to variations in correction parameters. One method uses the variation in the yield of the Cerenkov detector with the

parameter changes to determine the parameter slopes, this method will be called the yield method; it was the method used to determine the corrections in [73]. Another method, the asymmetry method, uses the variation of the asymmetry in the Cerenkov detector with helicity correlated parameter changes.

If the detector response were described completely by a linear function of perfectly measured correction parameters, both methods would be identical. Under actual experimental conditions, the two methods give different results. The differences come from different sensitivities to sources of error in the determination of the parameter slopes.

3.5.1 Determining Correction Slopes from the Yield

The detector response is modeled by the equation

$$Y_{corr,k} = Y_{meas,k} - \sum_{i=1,6} \left(P_{i,k} - \langle P_i \rangle\right) \frac{\partial Y}{\partial P_i} \tag{3.23}$$

where $Y_{corr(meas),k}$ is the corrected(measured) Cerenkov detector yield for beam pulse k and $P_{i,k}$ is the measured value of parameter i for that pulse. The slopes are determined by measuring the correlation coefficients between the yield and beam parameters. The relationship between the slopes and the correlation coefficients is expressed in the matrix equation

$$\begin{pmatrix} \langle \delta Y \delta P_1 \rangle \\ \langle \delta Y \delta P_2 \rangle \\ \langle \delta Y \delta P_3 \rangle \\ \langle \delta Y \delta P_4 \rangle \\ \langle \delta Y \delta P_5 \rangle \\ \langle \delta Y \delta P_6 \rangle \end{pmatrix} = \begin{pmatrix} \langle \delta P_1 \delta P_1 \rangle & \langle \delta P_1 \delta P_2 \rangle & \cdots & \langle \delta P_1 \delta P_6 \rangle \\ \langle \delta P_2 \delta P_2 \rangle & \langle \delta P_1 \delta P_2 \rangle & \cdots & \langle \delta P_2 \delta P_6 \rangle \\ \langle \delta P_3 \delta P_3 \rangle & \langle \delta P_1 \delta P_2 \rangle & \cdots & \langle \delta P_3 \delta P_6 \rangle \\ \langle \delta P_4 \delta P_4 \rangle & \langle \delta P_1 \delta P_2 \rangle & \cdots & \langle \delta P_4 \delta P_6 \rangle \\ \langle \delta P_5 \delta P_5 \rangle & \langle \delta P_1 \delta P_2 \rangle & \cdots & \langle \delta P_5 \delta P_6 \rangle \\ \langle \delta P_6 \delta P_6 \rangle & \langle \delta P_1 \delta P_2 \rangle & \cdots & \langle \delta P_6 \delta P_6 \rangle \end{pmatrix} \begin{pmatrix} \frac{\partial Y}{\partial P_1} \\ \frac{\partial Y}{\partial P_2} \\ \frac{\partial Y}{\partial P_3} \\ \frac{\partial Y}{\partial P_4} \\ \frac{\partial Y}{\partial P_5} \\ \frac{\partial Y}{\partial P_6} \end{pmatrix} \tag{3.24}$$

where $\delta Y \equiv Y - \langle Y \rangle$ is the difference between the yield in a given beam pulse and the average yield over an entire run. Similarly, $\delta P_i \equiv P_i - \langle P_i \rangle$ is the difference between

parameter i for a pulse and the average value of that parameter over a run. The correlation vector between the yield and the parameters , $V_i^Y = \langle \delta Y \delta P_i \rangle$, and the correlation matrix of the parameters, $M_{i,j}^Y = \langle \delta P_i \delta P_j \rangle$, are calculated for a one hour run in the first pass of the analysis software.

The slopes of the detector yield with respect to parameter variation, $\frac{\partial Y}{\partial P_i}$, are found at the end of the run by solving the matrix equation. The corrections are applied to each pulse, and the corrected asymmetry is given by

$$A_{corr}^Y = \frac{Y_{corr}^+ - Y_{corr}^-}{Y_{corr}^+ + Y_{corr}^-} \tag{3.25}$$

Correcting each pulse allows for the statistical examination of the corrected data.

3.5.2 Determining Correction Slopes from the Asymmetry

This method uses the same model of the linear dependence of the Cerenkov detector yield on the parameters, but measures the slope by comparing different asymmetry measurements rather than different yield measurements. Here the slope of the asymmetry to the parameter difference is measured. The corrected asymmetry is given by

$$A_{corr}^A = A - \sum_{i=1,6} A_i^P \frac{\partial A}{\partial A_i^P} \tag{3.26}$$

where $A \equiv (Y^+ - Y^-) \div (Y^+ + Y^-)$ is the asymmetry; $A_i^P \equiv P_i^+ - P_i^-$ is the helicity correlated parameter difference (HCPD) for position, angle, energy and charge. With these definitions, the slopes of Cerenkov detector asymmetry with respect to the parameter differences and asymmetries is determined by solving the following matrix

equation:

$$\begin{pmatrix} \langle \delta A \delta A_1^P \rangle \\ \langle \delta A \delta A_2^P \rangle \\ \langle \delta A \delta A_3^P \rangle \\ \langle \delta A \delta A_4^P \rangle \\ \langle \delta A \delta A_5^P \rangle \\ \langle \delta A \delta A_6^P \rangle \end{pmatrix} = \begin{pmatrix} \langle \delta A_1^P \delta A_1^P \rangle & \langle \delta A_1^P \delta A_2^P \rangle & \cdots & \langle \delta A_1^P \delta A_6^P \rangle \\ \langle \delta A_2^P \delta A_1^P \rangle & \langle \delta A_1^P \delta A_2^P \rangle & \cdots & \langle \delta A_2^P \delta A_6^P \rangle \\ \langle \delta A_3^P \delta A_1^P \rangle & \langle \delta A_1^P \delta A_2^P \rangle & \cdots & \langle \delta A_3^P \delta A_6^P \rangle \\ \langle \delta A_4^P \delta A_1^P \rangle & \langle \delta A_1^P \delta A_2^P \rangle & \cdots & \langle \delta A_4^P \delta A_6^P \rangle \\ \langle \delta A_5^P \delta A_1^P \rangle & \langle \delta A_1^P \delta A_2^P \rangle & \cdots & \langle \delta A_5^P \delta A_6^P \rangle \\ \langle \delta A_6^P \delta A_1^P \rangle & \langle \delta A_1^P \delta A_2^P \rangle & \cdots & \langle \delta A_6^P \delta A_6^P \rangle \end{pmatrix} \begin{pmatrix} \frac{\partial A}{\partial A_1^P} \\ \frac{\partial A}{\partial A_2^P} \\ \frac{\partial A}{\partial A_3^P} \\ \frac{\partial A}{\partial A_4^P} \\ \frac{\partial A}{\partial A_5^P} \\ \frac{\partial A}{\partial A_6^P} \end{pmatrix} \tag{3.27}$$

where $\delta A \equiv A - \langle A \rangle$, the difference between the asymmetry for one pulse pair and the average asymmetry for a run and $\delta A_i^P \equiv A_i^P - \langle A_i^P \rangle$, is the difference between the HCPD for one pulse pair and the average HCPD for a run. As with the previous method, $V_i^a \equiv \langle \delta A \delta A_i^P \rangle$ the covariance vector between the Cerenkov asymmetry and the parameter asymmetry and $M_{i,j}^a \equiv \langle \delta A_i^P \delta A_j^P \rangle$ the covariance between parameter asymmetries are calculated for each run in a first pass of the analysis code. If the linear model of the detector yield was a complete description and there were no instrumental errors in the parameter measurements, the asymmetry and yield slopes would be related by

$$\frac{\partial A}{\partial A_i^P} = \frac{1}{2\langle Y \rangle} \frac{\partial Y}{\partial P_i} \tag{3.28}$$

As with the yield method, the corrections are performed on each pulse pair in the second pass of the analysis code.

3.5.3 Evaluating the corrections

Both methods of measuring the parameter slopes can give erroneous results when applied to the experimental data. Noise on the parameter measurements can affect the diagonal elements of the parameter covariance matrix, leading to errors in the calculation of the slope. Unmeasured parameters which affect the yield and are correlated with one of the correction parameters would also cause errors in calculation of the slopes. For both methods the error in the determination of the slope can be

significant compared to the size of true slopes. Checks on the internal consistency of the corrections agree with the expectations from the sources of error considered, as demonstrated below.

Instrumental Error in Parameter Measurements

The error caused by instrumental uncertainty affects any attempt at multiple linear regression. An examination of the elements $M^A_{i,j}$ reveals the problem. If there is a random error, ϵ_i, in the measurement of the HCPD in parameter i with a Gaussian distribution of width σ_{ϵ_i}, then the measured value of $M^A_{i,j}$ becomes

$$\begin{aligned} M^A_{i,j} &= \langle(\delta A^P_i + \epsilon_i)(\delta A^P_j + \epsilon_j)\rangle \\ &= \langle \delta A^P_i \delta A^P_j \rangle + \langle \delta A^P_i \epsilon_j \rangle + \langle \epsilon_i \delta A^P_j \epsilon_i \rangle + \langle \epsilon_i \epsilon_j \rangle \end{aligned}$$

where $\sigma_{A^P_i}$ is the width of the parameter asymmetry distribution. Assuming the random instrumental error is not correlated with the value of the measurements, $\langle \delta A^P_i \epsilon_j \rangle$ vanishes for all matrix elements. Further, assuming the random instrumental errors on the parameter measurements are not correlated with each other, $\langle \epsilon_i \epsilon_j \rangle$ vanishes for the off-diagonal matrix elements. Under these assumptions, it is only the diagonal elements of $M^A_{i,i}$ which are affected by random instrumental errors:

$$\begin{aligned} M^A_{i,i} &= \langle(\delta A^P_i + \epsilon_i)(\delta A^P_i + \epsilon_i)\rangle \\ &= \langle(\delta A^P_i)^2\rangle + \langle(\epsilon_i)^2\rangle \\ M^A_{i,i} &= (\sigma_{A^P_i})^2 + (\sigma_{\epsilon_i})^2 \end{aligned} \tag{3.29}$$

When the width of the parameter asymmetry distribution becomes too small, the random instrumental error can cause significant deviation from the true slopes.

The asymmetry method is most sensitive to the effects of the random instrumental error because the variance of the HCPD is smaller than the variance of the parameters. Further, we find that the noise on the charge monitors is large enough to affect the

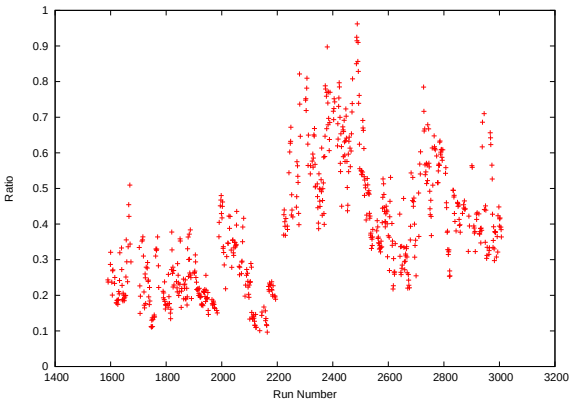

Figure 3.7: The ratio of the estimated random instrumental error on the charge monitor asymmetry, σ_{ϵ_I}, to the width of the charge asymmetry is shown. The square of this ratio gives the modification to the variance of the charge asymmetry in the covariance matrix used to determine the slopes for correcting helicity correlated beam differences.

slope determination; estimates of the width of the random instrumental error on the charge monitors (σ_{ϵ_I}) and the resulting effect on the corrections procedure are described below. Because the two charge monitors closest to the target have no apertures between them, they should report the same charge asymmetry for each pulse pair. Assuming the random instrumental error on these charge monitors is identical, Gaussian and uncorrelated, the width of the random instrumental error on one charge monitor can be obtained by dividing standard deviation of the difference between the charge asymmetries reported by the two monitors by the square root of two.

$$\sigma_{\epsilon_I} = \frac{1}{\sqrt{2}}\sqrt{\sum_k^N \frac{1}{N}(\Delta A^P_{I,k} - \langle \Delta A^P_I \rangle)^2} \tag{3.30}$$

$$\Delta A^P_{I,k} \equiv A^P_{I_1,k} - A^P_{I_2,k} \tag{3.31}$$

where σ_{ϵ_I} is the width of the random instrumental error in the charge asymmetry measurement and $A^P_{I_{1,2}}$ are the asymmetries measured by the two charge monitors closest to the target. Figure 3.7 shows the ratio of the estimate for σ_{ϵ_I} to the measured width of $A^P_{I_2}$.

In many runs the relative size of the random instrumental error on the charge

distribution is large enough to affect the corrections procedure. The size of the effect on the corrections procedure is estimated by inserting a larger value of $M^A_{I,I}$ into the covariance matrix when the slopes are determined. Introducing an inflated value of $M^A_{I,I}$ into runs with relatively small amounts of noise changed the correction to individual runs by approximately fifty percent of the typical value of the correction. The magnitude of the slopes of the Cerenkov asymmetry with respect to the energy and the beam charge were consistently larger with the simulated noise.

For the yield method of determining the slopes, the width of the parameter distribution is large enough that the effects of random instrumental error on the yield corrections are less important. The width of the parameter difference distribution can be used to estimate an upper bound on the random instrumental error. For example, the width of the position difference distribution is at least a factor of $\sqrt{2}$ wider than the instrumental error on the position measurement. The factor of $\sqrt{2}$ is included because the random instrumental errors on the positive and negative helicity measurements add in quadrature to give the random instrumental error on the parameter difference. In the runs with the narrowest parameter distributions, the diagonal elements of $M^Y_{i,i}$ would be affected by less than ten percent.

Unmeasured Additional Parameters

Not all of the parameters which affect the yield in the Cerenkov detectors are measured. Unmeasured parameters correlated with correction parameters will cause errors in the slope determination, though not necessarily in the raw asymmetry. Both the unmeasured parameters and the correction parameters drift slowly with time, making spurious correlations likely. Because the change in yield caused by unmeasured parameters can be much greater than the change caused by the correction parameters, the yield method is significantly affected by unmeasured parameters. This discussion will focus on the Cerenkov phototube gain as the unmeasured pa-

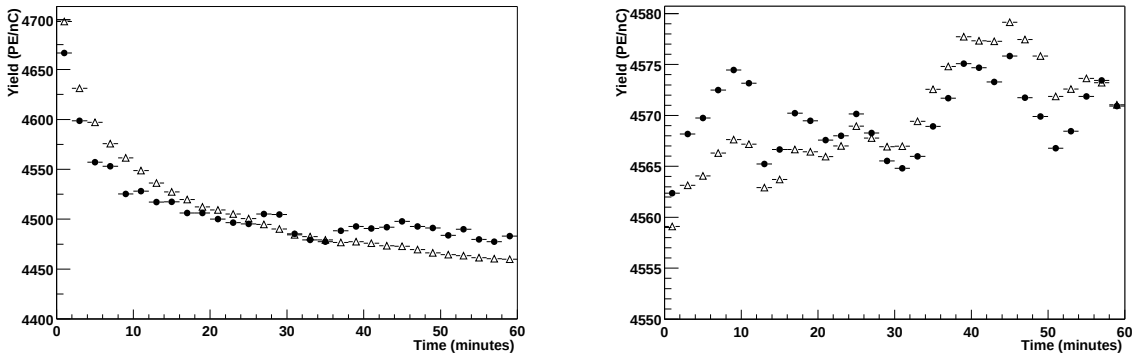

a) b)

Figure 3.8: The sum of the yields of the ten detector segments as a function of time during two different runs. The unfilled triangles show the uncorrected yield and the filled circles show the corrected yield. a) Data is shown from run 2448. The detector was turned on immediately before the run began; the smooth decrease in the uncorrected detector signal with increasing time results from decreasing gain as the phototube and preamplifier warm up. As a result of spurious correlations between the gain and corrections parameters, the slopes for the correction parameters are not accurate and the corrected yield is more erratic than the uncorrected yield. b) Run 2407 is a more typical run. While the variation with time is less dramatic, it is still clear that much of the variation in the yield is not accounted for by the correction parameters.

rameter, though other unmeasured parameters may contribute. The changing gain is clearly present in data recorded after the detector phototubes are turned on as shown in Figure 3.8a). Because slow drifts average out of the asymmetry and the HCPD, the unmeasured parameters discussed in this section will affect neither the raw asymmetry nor the asymmetry method.

In order for an unmeasured parameter to affect the corrections procedure it must be correlated with both the detector yield and at least one of the corrections parameters. This is easily demonstrated in a two dimensional case; consider the measured variable x1 and the unmeasured variable x2. If some function $Y(x_1, x_2)$ depends linearly on random variables x_1 and x_2 with Gaussian distributions symmetric about

zero, the slopes $\frac{\partial Y}{\partial x_1}$ and $\frac{\partial Y}{\partial x_2}$ can be determined from measurements of Y, x_1 and x_2.

$$\begin{pmatrix} \langle Y x_1 \rangle \\ \langle Y x_2 \rangle \end{pmatrix} = \begin{pmatrix} \langle x_1^2 \rangle & \langle x_1 x_2 \rangle \\ \langle x_1 x_2 \rangle & \langle x_2^2 \rangle \end{pmatrix} \begin{pmatrix} \frac{\partial Y}{\partial x_1} \\ \frac{\partial Y}{\partial x_2} \end{pmatrix} \tag{3.32}$$

The solution for $\frac{\partial f}{\partial x}$ is

$$\frac{\partial f}{\partial x} = \frac{\langle Y x_1 \rangle \langle x_2^2 \rangle - \langle Y x_2 \rangle \langle x_1 x_2 \rangle}{\langle x_1^2 \rangle \langle x_2^2 \rangle - \langle x_1 x_2 \rangle^2}. \tag{3.33}$$

If x_1 and x_2 are not correlated or x_2 is not correlated with Y, the previous equation reduces to

$$\frac{\partial f}{\partial x_1} = \frac{\langle f x_1 \rangle}{\langle x_1^2 \rangle}, \tag{3.34}$$

which can be found without measuring x_2.

In runs taken while the detector is still warming up, simple calculations suggest the determining the correction slopes with the yield method will be unreliable. The correlation between gain and yield is so much stronger than the correlation between any of the measured parameters and yield that a small correlation between a parameter and the gain dramatically disturbs the slope measurement. The run shown in Figure 3.8a) demonstrates this problem. When Y is taken to be the yield in the detector, x_1 to be any of the correction parameters and x_2 to be time (time standing in for the unmeasured gain), the second term in the numerator of equation 3.33 is larger than the first regardless of which corrections parameter is used. This suggests that the error in the slope determination may be as large as the slope.

The gain change as the phototubes warm up is the most extreme example of an unmeasured parameter, but other unmeasured parameters may significantly affect the yield correction method. A plot of the corrected Cerenkov yield as a function of time shows variation that is not explained by the correction parameters in all of the runs. Figure 3.8b) shows a typical run. Because the variation in the yield and the correction parameters both have long time scales, correlations between the unmeasured parameters and the correction parameters are likely. While the correction

in individual runs may be disturbed by the effect of unmeasured parameters, this effect is unlikely to cause a systematic error. Because the correlations that cause this effect come from slow drifts in gain and correction parameters, the sign and size of the error in the correction can be expected to vary.

Internal Consistency

The average asymmetry of data which is given a correction of one unit should lie one unit away from the the average asymmetry of the data given no correction, therefore the graph of the raw asymmetry versus the correction should be a line with slope negative one. The graph of A vs. $A_{corr} - A$ will be referred to as the "correction graph", and the slope of a linear fit to this graph will be referred to as the "correction slope". Deviations of the correction graph from a line with slope negative one can provide information about the kind of errors made in the corrections.

Different types of errors in data correction procedures produce different effects on the correction graph. When the magnitude of the corrections is too small by a constant factor, the points on the correction graph are bunched more tightly along the correction axis and the correction slope becomes steeper than negative one. Conversely, when the magnitude of the corrections is too large by a constant factor, the correction slopes becomes shallower. Finally, random errors in the correction spread the points in the correction graph out along the horizontal axis, reducing the correction slopes. These errors are illustrated in Figure 3.9.

This check for internal consistency is not a definitive indicator of accuracy in the corrections. For corrections of one parameter, it is possible that the effects of corrections too small by a constant factor and random errors in the correction balance each other. In this circumstance the correction slope would be negative one, but the average correction would be too small. It is also possible that random errors can make the correction slope shallower than negative one when the average correction is

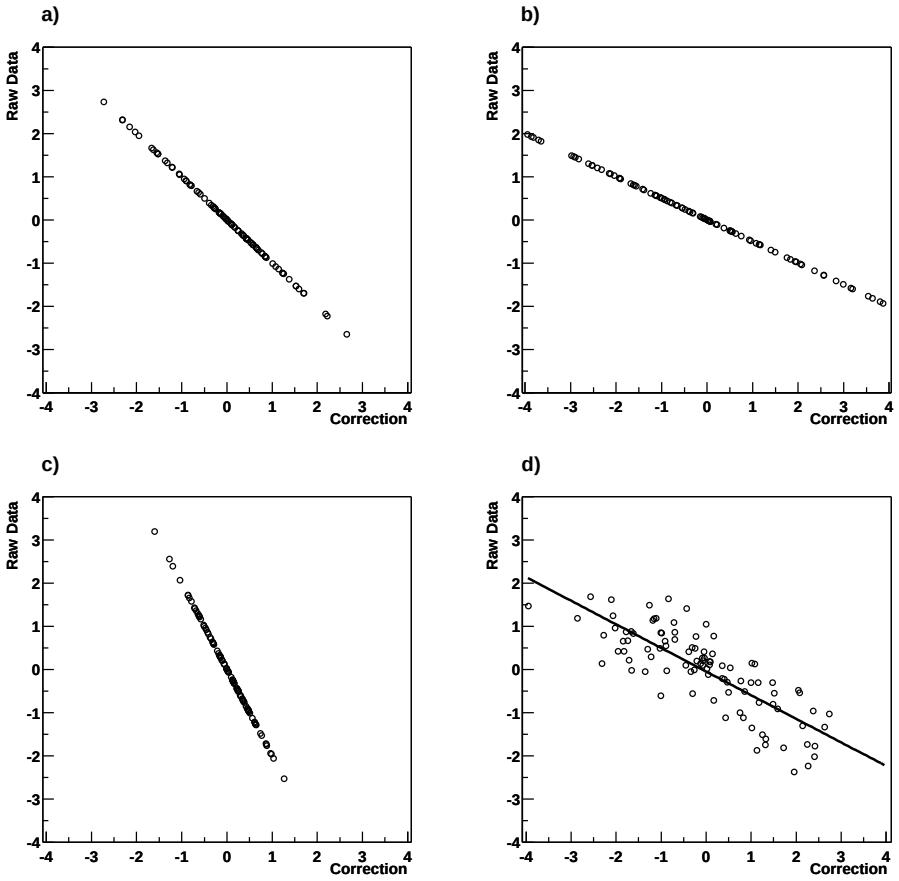

Figure 3.9: The data shown in this figure come from a Monte Carlo simulation of measurements of a hypothetical constant quantity which has a linear dependence on a single confounding variable with a Gaussian distribution of width one unit. a) If the slope of the confounding variable is measured correctly and its effects are removed, the correction slope is negative one. b) If the slope used to correct for the confounding variable is too large, the corrections are too large, and the correction slope is too shallow. c) If the corrections are too small, the correction slope is too steep. Here the corrections are too small by a factor of two. d) Random errors in the correction spread out the data in the correction graph along the correction axis, making the slope shallower. Here the random error added to the correction is drawn from a Gaussian distribution with the same width as the correction. The solid line is a linear fit to the points.

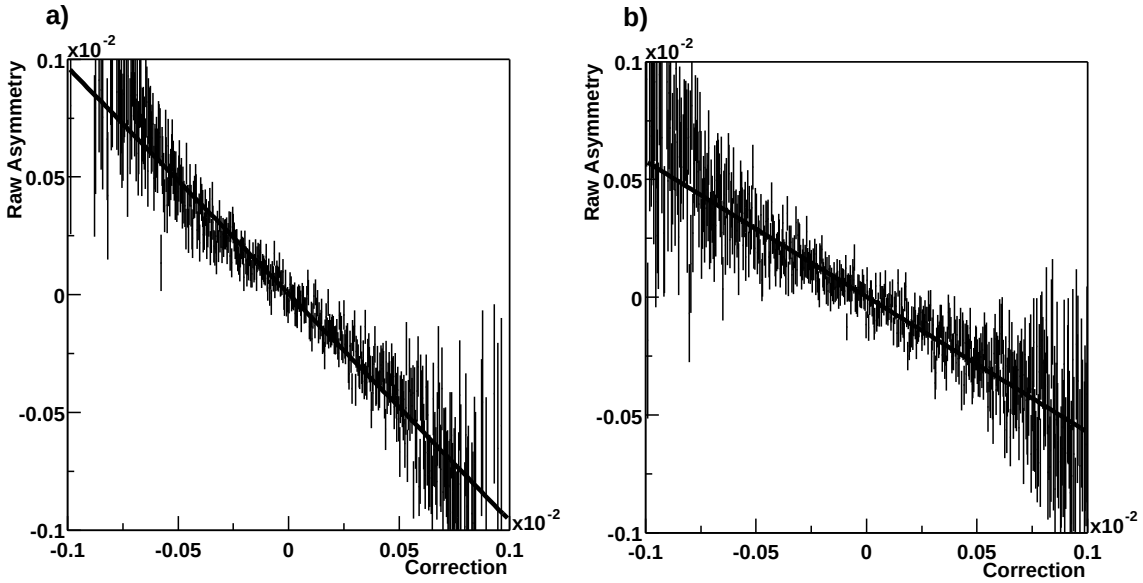

Figure 3.10: The correction graphs for the pulse pair asymmetries within run 1640, the solid line is a linear fit to the correction graph. a) The correction graph for the asymmetry method corrections. b) The correction graph for the yield method corrections.

correct.

When several variables are corrected simultaneously, the effects of making corrections too small for one variable and too large for another can also cancel out in the correction slope. This cancellation is limited to parameters which have distributions of corrections that are of similar width; if the distribution of corrections for one parameter is much wider than the others, the parameter with the wide correction distribution dominates the determination of the correction slope. This domination stems from the larger lever arm of the wider distribution in the correction graph.

The correction graphs for both the yield and asymmetry methods are constructed for the corrections to individual asymmetry measurements within a run; Figure 3.10 shows the correction graphs for run 1640. A line is fit to each correction graph to determine the correction slope for each run, and the results of these fits are shown in Figure 3.11.

Despite the ambiguity in the interpretation of correction graphs, correction slopes from the data are consistent with the hypothesis that the instrumental error in the

charge monitor is the primary cause of errors in the asymmetry method. The runs with relatively large instrumental errors on the charge monitors have correction slopes significantly different from negative one. This can be seen by comparing Figure 3.7 to Figure 3.11a. Further, artificially inflating $M_{I,I}^{A}$ in runs with small instrumental error produces correction slopes consistent with the runs that have larger instrumental error.

The correction slopes for the yield method confirm that the unmeasured gain can disturb the correction procedure. Runs taken immediately after the Cerenkov phototubes were turned on have correction slopes near zero. For these runs, the correction appears to be entirely random. This is consistent with the estimate for the effect of the unmeasured gain on these runs. However, the phototube warm-up accounts for at most a few dozen runs with bad (far from negative one) correction slopes. Changes in gain not associated with the warm-up or slow changes in background may account for the majority of runs with bad correction slopes.

A simpler consistency check can be applied to the yield method as well. When the corrections are working properly, it is expected that they will reduce the width of the asymmetry distribution. In approximately one third of the runs the yield corrections fail to reduce the width of the asymmetry distribution (σ_A), and it is the runs with correction slopes shallower than -0.5 which fail to reduce σ_A. The typical magnitude of the yield method corrections for runs in which the yield method fairs poorly on the checks for internal consistency is approximately twice the size of the yield corrections for the other runs.

3.5.4 Conclusions

The efforts described in Chapter 2 to improve the stability of the beam and minimize the effects instabilities on the measured asymmetry in the Cerenkov detector have been largely successful. It is this success which makes the correction for helicity

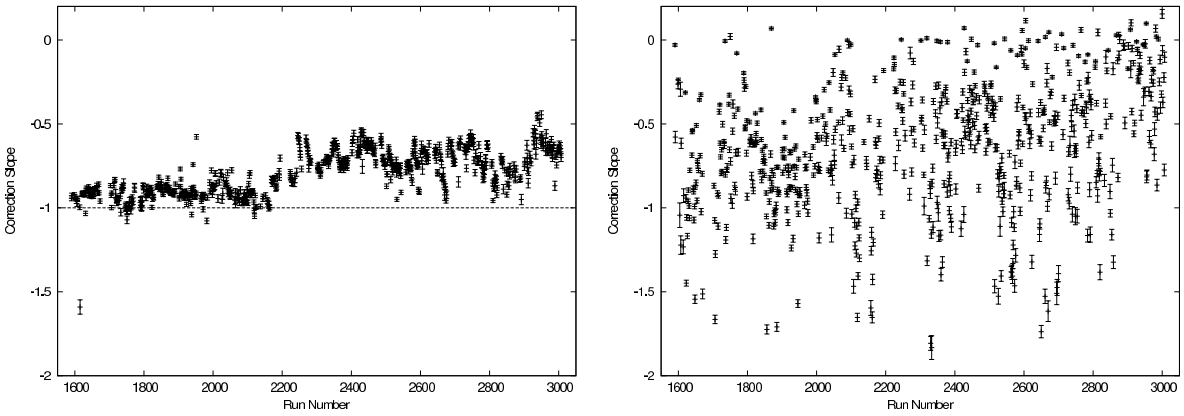

a) b)

Figure 3.11: The slopes from correction graphs for each run. a) The correction slopes for the asymmetry method corrections. b) The correction slopes for the yield method corrections.

correlated changes difficult. For the yield method, the difficulty appears to be that the effects of helicity correlated beam changes are not large enough that the slope can be measured reliably. If the sensitivity to the correction parameters were larger, the relative importance of the unmeasured parameters would be smaller and the slope of the yield with respect to parameter changes would be determined more accurately. For the asymmetry method, it is the stability of the beam which makes the slope determination difficult. The corrected asymmetry for each detector segment is given in Table 3.5.

The results from the asymmetry method will be used in the rest of this work. The preference for the asymmetry method comes from the consistency check provided by the correction graphs, and the estimated sizes of the sources of error for the two methods. While the correction graphs are not definitive, the asymmetry method is generally closer to negative one for the asymmetry method. Using the asymmetry method to determine the parameter slopes gives a correction of 0.23 ppm to the physics asymmetry of approximately negative eight parts per million, while the yield method gives a correction of 0.36 ppm. Based on the estimate of the size of error introduced by unmeasured parameters, an uncertainty of 100% is assigned to the

Table 3.5: Summary of dilution factors and the corrected measured asymmetry
The measured asymmetry, A^A_{corr}, corrected for helicity correlated parameter differences with the asymmetry method is listed for each mirror. The dilution factors associated with the backgrounds (f_l, f_c and $\frac{1}{1-f_\pi}$ discussed in Section 3.2) and the dilution factor for the radiative corrections (R_c discussed in section 3.3) are collected here for convenience.

Mirror	f_l	f_c	$\frac{1}{1-f_\pi}$	R_c	A^A_{corr}
1	0.740 ± 0.002	0.905	1.085	1.116	-1.6899 ± 0.3861
2	0.610 ± 0.004	0.895	1.082	1.092	-1.7142 ± 0.4405
3	0.740 ± 0.001	0.872	1.085	1.116	-1.7567 ± 0.3892
4	0.740 ± 0.002	0.895	1.075	1.158	-0.3938 ± 0.3698
5	0.470 ± 0.002	0.941	1.072	1.068	-0.9011 ± 0.4590
6	0.470 ± 0.002	0.929	1.072	1.068	-0.5243 ± 0.4546
7	0.720 ± 0.001	0.901	1.075	1.158	-1.9495 ± 0.3723
8	0.730 ± 0.002	0.858	1.085	1.116	-1.0053 ± 0.3949
9	0.630 ± 0.002	0.882	1.082	1.092	-1.6382 ± 0.4061
10	0.740 ± 0.002	0.900	1.085	1.116	-1.8843 ± 0.3829

yield correction. For the asymmetry method, the correction and the relative size of its estimated error are both smaller for individual runs. However, the error in the parameter slopes is likely to be in the same direction for each run. To be conservative, the systematic uncertainty of 0.36 ppm is retained for the asymmetry method as well.

3.6 Physics Asymmetry

Collecting all of the effects discussed in this chapter gives the physics asymmetry along with its associated statistical and systematic uncertainty. The dilution factors and

measured asymmetries in Table 3.5 combined with the measured beam polarization of 35.7% according to equation 3.2 give the physics asymmetries for each mirror. Combining asymmetry for each mirror according to equation 3.7 give the measured physics asymmetry for the detector as a whole. The systematic uncertainty is the combination in quadrature of all of the systematic uncertainties considered in this chapter. The combined physics asymmetry is $A_{phys} = -7.74 \pm 0.71 \pm 0.60$ ppm where the first uncertainty is statistical and the second is systematic.

The difference between the value reported here and that used in reference [73] comes primarily from changes to the pion fraction [73]. Previous work had estimated the pion contribution to be only two percent. In particular, the π^- production is much larger than had been expected. The integration mode method of determining the Cerenkov fraction described in Section 3.2.2, has also been improved. Previously, it was assumed that the ratio of own scintillation light to other scintillation light was one for all mirror types. The radiative corrections discussed in Section 3.3 have also been modified; the primary difference is the inclusion of the full detector geometry. The previous calculation had only addressed the central angle for each detector segment. Previous work also used the yield correction method rather than the asymmetry method. This change is the least significant. The differences are summarized in Table 3.6.

Table 3.6: Differences from the previously published results

Most of the analyses used to determine A_{phys} have been improved since the publication of reference [73]. With the exception of the helicity correlated position difference correction, the updated analyses increased the size of the physics asymmetry.

Analysis	Change (%)
Pion fraction	6
Cerenkov fraction	2
Radiative corrections	2
Hel. Corr. Beam Diff.	1

Chapter 4

Results and Conclusions

4.1 Determining $G_A^e(T=1)$ and G_M^s

The experimental determination of the asymmetry in electron deuteron scattering includes effects of QE and elastic scattering from the deuteron. The expression for the deuteron asymmetry is given by

$$A_d = \frac{A_{QE}\sigma_{QE} + A_E\sigma_E}{\sigma_{QE} + \sigma_E} \tag{4.1}$$

As discussed in Section 1.5, a calculation of the dependence of the $e^- - d$ PV asymmetry in terms of $G_A^e(T=1)$ and G_M^s based on the work in reference [45] is used to determine the deuteron asymmetry dependence on single nucleon form factors. Because the SAMPLE detector has limited energy resolution, the contribution from the QE asymmetry is a convolution of the QE asymmetry, cross section and detector acceptance over a range of energy loss. This convolution, as well as the convolution of the elastic asymmetry with the detector acceptance is done with Monte Carlo simulation.

An expression for the deuteron asymmetry is calculated in terms of the single nucleon form factors,

$$A_d = A_0 + A_2 G_A^e(T=1) + A_3 G_M^s \tag{4.2}$$

where $A_{0,2,3}$ are determined by a GEANT simulation similar to the one described in Section 3.3 with inputs from the calculations for the QE and elastic processes. Rocco Schiavilla provided calculations of the QE asymmetry in terms of $G_A^e(T=1)$ and G_M^s at the central scattering angles for each type of mirror at several energies. Interpolation from those values is used to determine the QE cross section and asymmetries for events in the simulation. The elastic asymmetry is given by the equation 1.48. The resulting coefficients are averaged over the ten detector segments using the same weights used to combine the experimental asymmetries. The combined expression for the deuteron asymmetry is

$$A_d = -7.061 + 1.664 G_A^e(T=1) + 0.772 G_M^s \; ppm \tag{4.3}$$

which can be compared directly to the experimental asymmetry, $A_d = -7.74 \pm 0.71 \pm 0.60$ *ppm* from the previous chapter. A similar procedure is used to determine the theoretical asymmetry for the proton measurement:

$$A_p = -5.562 + 1.541 G_A^e(T=1) + 3.367 G_M^s \; ppm \tag{4.4}$$

The calculation for the proton asymmetry is simpler because there are no nuclear structure effects to take into account; only the detector geometry, the energy loss in the target and the expression for the $e-p$ asymmetry given in equation 1.39 are needed.

The measured value of the proton asymmetry, is $A_p = -5.61 \pm 0.67 \pm 0.88$ ppm where the first uncertainty is statistical and the second asymmetry is systematic[48]. The larger systematic uncertainty in A_p comes from the background asymmetry in the hydrogen measurement. The χ^2 value of a constant fit to the background asymmetry from the ten detector segments in the hydrogen measurement had a likelihood of approximately one percent. The theoretical expression for A_p given above is slightly different from that used in reference [48]; the expression used here takes the full detector geometry into account while the previous work used only the central angle

of the mirrors.

The combination of the theoretical expressions with the physics asymmetries allows the determination of the weak vector axial form factor and the strange contribution to the magnetic form factor of the nucleon at a momentum transfer of 0.1 $(GeV/c)^2$:

$$G_M^s = 0.22 \pm 0.35 \pm 0.39 \pm 0.03 \; n.m. \tag{4.5}$$

$$G_A^e(T=1) = 0.51 \pm 0.55 \pm 0.48 \pm 0.12 \; n.m. \tag{4.6}$$

where the first uncertainty is statistical, the second is the systematic uncertainty from the experiments and the third is the uncertainty resulting from the extraction described in this section. The uncertainty in the extraction is dominated by the uncertainty in the EM form factors and in the isoscalar axial form factor. The separate and combined constraints on G_M^s and $G_A^e(T=1)$ from the measurements of the proton and deuteron asymmetries are shown in Figure 4.1.

While the major focus of the SAMPLE collaboration is the determination of these two form factors, the contributions from all three light quarks can be determined from equations 1.29 – 1.31. The net contributions to the magnetic form factor of the proton from the up and down quarks are given by

$$G_M^u = 2.60 \pm 0.35 \pm 0.39 \pm 0.03 \; n.m. \tag{4.7}$$

$$G_M^d = -1.01 \pm 0.35 \pm 0.39 \pm 0.03 \; n.m. \tag{4.8}$$

4.2 Comparison to Theory

The results from the experiment can be compared with the predictions for the weak isovector axial form factor and the strange contribution to the magnetic moment. In both cases, there is some uncertainty in extrapolating the experimental results to zero momentum transfer. However, the uncertainty in Q^2 dependence is small enough that comparisons are still reasonable.

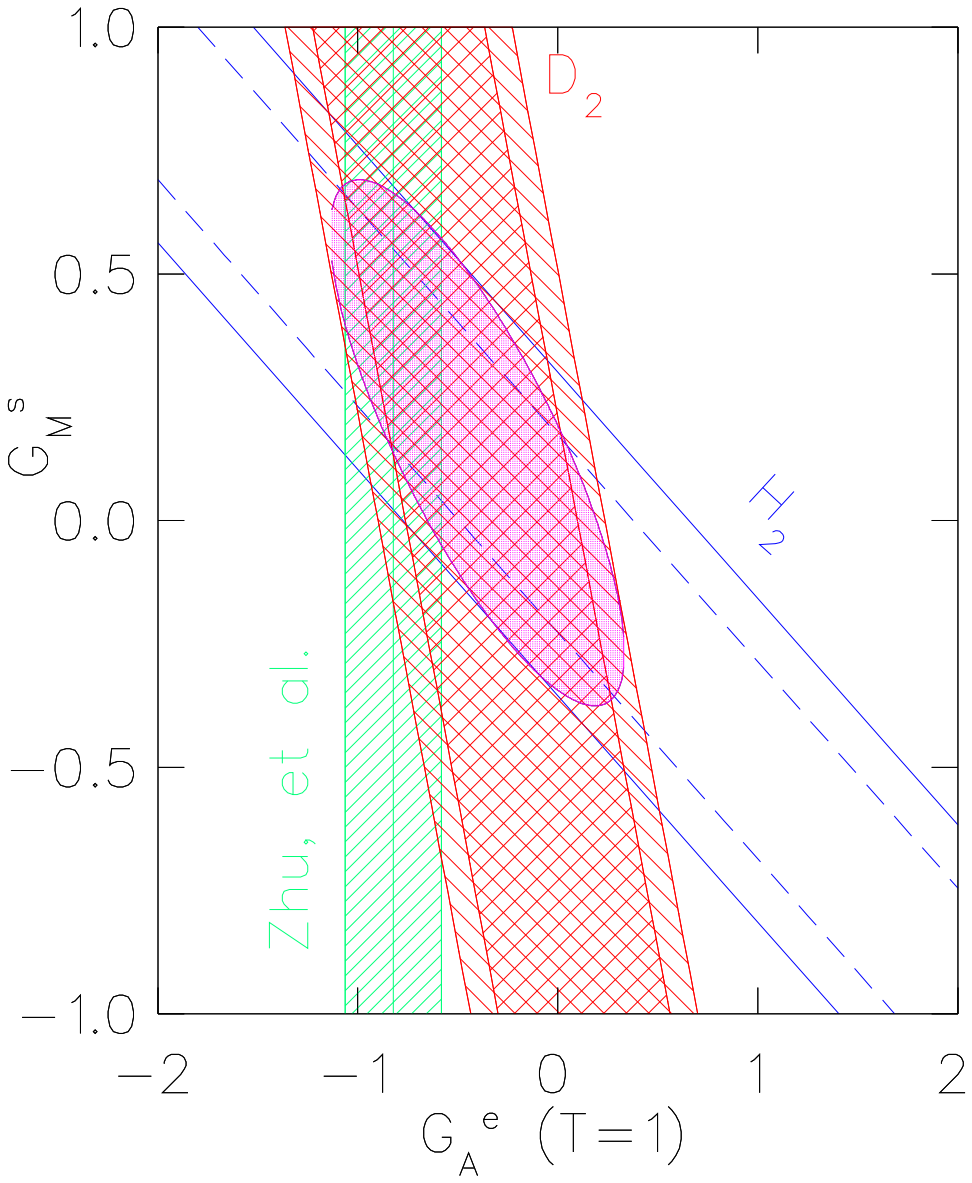

Figure 4.1: The allowed region in the two dimensional space of G_M^s and $G_A^e(T=1)$ is shown for each of the two measurements. The unfilled band is the constraint from the hydrogen measurement with the dashed lines representing the statistical uncertainty and the outer solid lines representing the systematic and statistical error added in quadrature. The crosshatched band represents the constraint from the deuterium measurement, with the inner region representing the statistical uncertainty and the outer region representing the statistical and systematic uncertainties added in quadrature. The ellipse shows the one standard deviation allowed region for G_M^s and $G_A^e(T=1)$ at $Q^2 = 0.1$ $(GeV/c)^2$. The prediction for $G_A^e(T=1)$ by Zhu *et al.* is represented by the vertical band.

For the axial form factor, the calculation of the anapole contributions by Zhu *et al.* is for zero momentum transfer [18]. In order to compare the corrections to G_A^e with experiment, they must be evolved to the momentum transfer of the experiment. Particularly in the case of the anapole contributions, where the interaction is a contact interaction, deviation from the dipole form factor might be expected. The Q^2 evolution of the anapole contributions has been examined by Maekewa *et al.* in chiral perturbation theory to next to leading order [24]. For the natural ranges of the coupling constants, a change of approximately twenty percent is found for the momentum transfer at the SAMPLE experiment. This change is small compared to both the theoretical uncertainty in the anapole contributions and the uncertainty in the measurement. The prediction of $G_A^e(T=1) = 0.83 \pm 0.26$ is consistent with the measured value.

All but one of the predictions for the strange quark form factor are for the zero momentum transfer limit. In order to compare the experiment at $Q^2 = 0.1\ (GeV/c)^2$ to the theory, some knowledge of the Q^2 dependence of G_M^s is necessary. A model independent prediction based on the leading order contribution in heavy baryon chiral perturbation theory has been made [74][75]. However, Hammer *et al.* found that higher order terms could contribute significantly, possibly dominating over the leading order term[76]. Further, the higher order terms involve unknown couplings in the effective field theory whose size must be estimated, ruining the model independence. The authors' estimates for the size of these coupling constants indicates that the extrapolation from SAMPLE's measured value of $G_M^s(Q^2 = 0.1)$ to μ_s could involve a change of 0.2 n.m. or larger in either direction. Provided the Q^2 dependence is not considerably larger than this, the measured value of $G_M^s(Q^2 = 0.1)$ is consistent with the predictions for μ_s listed in Table 1.3.

4.3 Related and Future Work

As discussed in Section 1.2.3, the quark components of both the magnetic and electric form factors can be measured with PV lepton scattering. Experiments sensitive to a combination of these form factors have been completed by the HAPPEX collaboration, and more are planned. The G0 collaboration will soon begin data for a series of experiments that will ultimately allow the determination of G_M^s, G_E^s and $G_A^e(T = 1)$ at several values of momentum transfer. The SAMPLE collaboration has also conducted a further investigation into the isovector axial form factor of the proton.

The HAPPEX collaboration measures the asymmetry PV $e^- - p$ scattering at forward scattering angles in an experiment run at Jefferson Lab. At forward angles, the variation in momentum transfer with scattering angle is much larger than at backwards angles; detectors with a relatively small angular acceptance are required to limit the range of momentum transfers to acceptable levels. Fortunately, the higher cross section at forward angles compensates for the smaller detector acceptance. The HAPPEX experiment uses a spectrometer to separate the elastically and inelastically scattered electrons and a lead scintillator run in integration mode to detect the elastically scattered electrons.

Because HAPPEX measures the asymmetry in forward scattered electrons, their experiment is relatively insensitive to the axial form factor. This can be seen by examining the angular dependence of the terms containing G_M^s, G_E^s, and G_A^e in equation 1.39. The first HAPPEX experiment was performed with an average scattering angle of 12.3° in the lab frame and a momentum transfer of momentum transfer of 0.447 $(GeV/c)^2$. This measurement constrains a linear combination of the strange electric and magnetic form factor:

$$G_E^s + 0.392 G_M^s = 0.025 \pm .020 \tag{4.9}$$

where the first uncertainty is statistical and the second is systematic [77]. An additional experiment is planned for an average scattering angle of 6° with a momentum transfer of 0.1 $(GeV/c)^2$, the results of which will be directly comparable to the SAMPLE experiment.

The G0 collaboration plans to measure G_M^s, G_E^s and G_A^e at Jefferson Lab over a range of momentum transfers between 0.1 and 1.0 $(GeV/c)^2$. The separation of all three form factors will be accomplished by measuring the asymmetry at both forward and backward angles in $e^- - p$ scattering as well as the asymmetry at backwards angles for $e^- - d$ scattering. The G0 experiment uses a superconducting toroidal magnet to separate elastic and inelastic events. Plastic scintillators run in pulse counting mode are used to record individual events.

The SAMPLE collaboration has taken additional data on the PV asymmetry in $e^- - d$ scattering at a lower energy of 125 MeV. The primary purpose of this investigation is to further constrain the isovector part of the axial form factor. The interest in $G_A^e(T=1)$ was partly motivated by the SAMPLE collaboration's initial publication of the data presented in this work [73]; without the benefit of data providing angular distribution of pion production on deuterium the correction to the axial form factor appeared to be near 100%. The 125 MeV SAMPLE experiment measures a smaller asymmetry, but with a similar figure of merit to the 200 MeV experiment. The lower energy reduces the size of the asymmetry, but this reduction is compensated by an increased cross section. Preliminary results from the 125 MeV experiment are consistent with the prediction of $G_A^e(T=1)$ by Zhu *et al.*, as are the updated results for the higher energy presented here [78][1]

[1]Reference [78] uses the yield method, presented in Section 3.5, for correcting the helicity correlated beam differences.

4.4 Conclusions

Parity-violating lepton scattering can be used to probe the low energy degrees of freedom in QCD. By measuring the PV cross section asymmetries in electron scattering from the deuteron and the proton at a momentum transfer and average scattering angle of 0.1 $(GeV/c)^2$ and 145°, the SAMPLE collaboration is able to determine both the contribution from the strange $q\bar{q}$ sea to the nucleon magnetic form factor, and the isovector axial form factor for electron-nucleon scattering. The asymmetries measured with the SAMPLE apparatus are:

$$A_p = -5.61 \pm 0.67 \pm 0.88 \; ppm \tag{4.10}$$

$$A_d = -7.74 \pm 0.71 \pm 0.60 \; ppm \tag{4.11}$$

where A_p is the asymmetry in longitudinally polarized electrons elastically scattered from the proton [48] and A_d is the asymmetry for electrons scattered from the deuteron. The strange quark contribution to the nucleon magnetic form factor and the isovector portion of axial form factor can be determined from the proton and deuteron asymmetries:

$$G_M^s = 0.22 \pm 0.35 \pm 0.39 \pm 0.03 \; n.m. \tag{4.12}$$

$$G_A^e(T=1) = 0.51 \pm 0.55 \pm 0.48 \pm 0.12 \; n.m. \tag{4.13}$$

The inclusion of recent data on pion production and an improved model of background acceptance are responsible for the difference between this result and that reported in [73] and [48]. These results are consistent with the predictions for the isovector axial form factor and the predictions for the strange magnetic moment listed in Table 1.3. While the current measurement is not able to distinguish between models, it provides an important constraint on QCD in the non-perturbative regime.

Appendix A

High Polarization Electron Source

This appendix describes a high polarization electron source using a strained GaAs crystal at the Bates Linear Accelerator Center. The goal was the creation of a source suitable for use in the 125 MeV SAMPLE experiment described in Section 4.3. The requirements for the electron beam in the SAMPLE experiments are an average current of 40 μA with average charge asymmetries less than 1 ppm, where the charge asymmetry is defined as the difference between the charge in the two helicity states divided by the sum. Ultimately, the charge asymmetry could not be reduced to the required level in the time available, and the strained GaAs source was not used for the 125 MeV SAMPLE experiment.

While the polarization achievable with strained GaAs crystals (greater then 70%) makes them attractive, there are two primary difficulties in using the strained crystal. First, the quantum efficiencies of the strained crystal are much lower than the quantum efficiencies of the bulk crystals. Second, the strain gives the crystal an analyzing power for linearly polarized light. This analyzing power acts like a greatly enhanced version of the PITA effect described in Section 2.1. Strained and bulk GaAs crystals are discussed in Section A.1. The optics are described in Section A.2, and the efforts to control the residual linear polarization of the light are described in Section A.3.

A.1 GaAs Photocathodes

The central idea in both bulk and strained GaAs photocathodes is to use circularly polarized light to excite electrons of one spin state from the valence band to the conduction band. The electrons in the conduction band migrate to the surface which is treated to have a negative electron affinity (NEA). The energy in the conduction band is higher than the energy level of the vacuum, so the electrons can be emitted from the surface. The surface must be maintained in high vacuum and periodically cleaned and retreated to maintain the NEA [49].

A degeneracy in the valence band limits the polarization in bulk GaAs. The conduction band has an S-type symmetry and the valence band has a P-type symmetry [79]. The spin-orbit coupling splits the $P_{3/2}$ states from the $P_{1/2}$ states. The desired transitions come from the $P_{3/2}$ with $m_j = \pm 3/2$, but these states are degenerate with the $P_{3/2}$, $m_j = \pm 1/2$ states. When photons with energy greater than the band gap but not as large as the band gap plus the spin orbit coupling are incident on the crystal, only electrons from the $P_{3/2}$ state can be excited to the conduction band. If the light is circularly polarized with positive helicity, only transitions with $\Delta m_j = \pm 1$ are allowed, and the transitions from the $P_{3/2}$, $m_j = -3/2$ states result in electrons in the $S_{1/2}$, $m_j = -1/2$ state in the conduction band. However, electrons in the degenerate $P_{3/2}$, $m_j = -1/2$ state can be excited to the opposite polarization state in the conduction band, $S_{1/2}$, $m_j = \pm 1/2$. Clebsch-Gordon coefficients give the relative strength of the two transitions; the transition from the $P_{3/2}$, $m_j = -3/2$ state is three times more likely. Therefore, the maximum theoretical polarization from the unstrained crystal is

$$P = \frac{3-1}{3+1} = 0.5 \tag{A.1}$$

The electron polarization is typically reduced to 30-40% during transport to the surface.

Growing a thin layer of GaAs on top of a crystal with a different lattice constant strains the crystal and breaks the quadruple degeneracy of the $P_{3/2}$ states [80]. The substrate used is a layer of $GaAs_{1-x}P_x$, whose lattice constant can be changed by varying the amount phosphorous. In the strained crystals the $P_{3/2}$ states with $m_j = \pm 3/2$ are closer to the conduction band than the $P_{3/2}$ states with $m_j = \pm 1/2$. By illuminating the crystal with photons whose energy is not high enough to excite the $P_{3/2}$ states with $m_j = \pm 1/2$ to the conduction band, the electrons excited to the conduction band can be completely polarized. Practically, polarizations in excess of 70% can be achieved. Yuri Mamaev at the State Polytechnical Instute in St. Petersburg, Russia grew the strained crystals used at Bates.

However, the higher polarization comes at a cost. The quantum efficiencies are lower, and an analyzing power for linearly polarized light is introduced [79]. Linearly polarized light shining along the preferred axis can have a quantum efficiency as much as 10% higher than light polarized in the perpendicular direction. Due to the large analyzing power, the direction of the residual linear polarization of the light is important.

A.2 Laser and Optics

A fiber-coupled diode laser was chosen as the light source for the high polarization source. The model chosen provides 60 W of light at 808 nm, thought to be the correct wavelength for achieving maximum polarization for the strained crystal[1]. In this laser system the light from several lasers is collected by a bundle of multi-mode optical fibers. The chief advantages of this laser are its high power and ease of operation. However, the light is not polarized and is emitted with a divergence of 30 mr. Half of the power is lost in polarizing the light, and the high divergence drove many of the

[1]The laser is a Spectra Physics, model number BFA1500-808-60-01

design decisions.

One of constraints imposed by the high divergence of the laser is the proximity of the laser to the crystal. Because of the difficulty of transporting a high divergence light beam, the laser is located as close as possible to the crystal; therefore laser light comes in from the side rather than along the beam pipe as it does in the bulk GaAs system. The light is incident on the crystal at an angle of approximately $\theta_i = 40°$ from perpendicular. This angle of incidence creates an additional analyzing power for linearly polarized light.

It is straightforward to determine the analyzing power due the incident angle. The angle of the transmitted light is given by

$$\sin\theta_t = \frac{1}{n}\sin\theta_i$$

where $n = 3.6$ is the index of refraction for 808 nm light in GaAs [81]. The transmittance for light polarized in the plane of the crystal surface is given by

$$T_{\|} = 1 - \frac{\tan^2(\theta_i - \theta_t)}{\tan^2(\theta_i + \theta_t)} \tag{A.2}$$

while the transmittance for light with a perpendicular polarization is given by

$$T_{\perp} = 1 - \frac{\sin^2(\theta_i - \theta_t)}{\sin^2(\theta_i + \theta_t)} \tag{A.3}$$

The analyzing power is given by

$$\epsilon = \frac{T_{\|} - T_{\perp}}{T_{\|} - T_{\perp}} \simeq 0.15 \tag{A.4}$$

which is larger than the intrinsic analyzing power of the crystal.

The elements in the optical system are shown in Figure A.1. The position feedback device and the CPC are those described in Section 2.1. The intensity is controlled by the current supplied to the laser; the shutter and rotatable half wave plate between linear polarizers used to control the intensity in the bulk GaAs laser system are not needed. Because the performance of a Pockels cell degrades dramatically for light

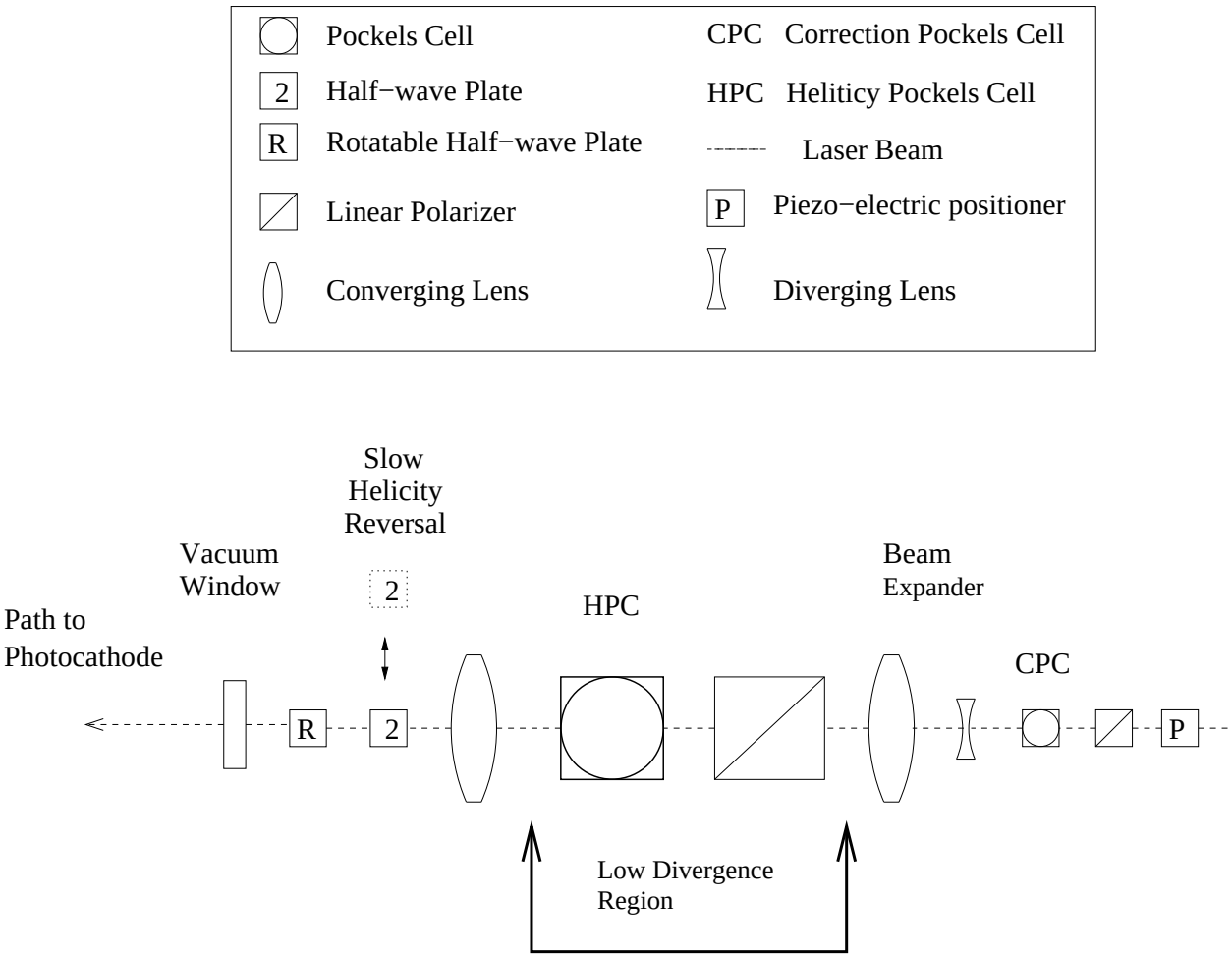

Figure A.1: High polarization optical elements. The light incident on the strained GaAs photocathode (not shown) is at an angle of approximately 40° from the perpendicular. The vacuum window may exhibit some birefringence.

not traveling parallel to the optical axis, the HPC used has a clear aperture of 80 mm and is placed in a region of expanded beam [82]. Unfortunately, the performance also drops off with size; the circular polarization achieved is approximately 95%. As in the bulk system, a half-wave plate is used to reverse the helicity of the laser light independent of the electronics. An additional half-wave plate is used to rotate the direction of residual linear polarization, as described below.

A.3 Residual Linear Polarization

By controlling the direction of residual linearly polarization, the charge asymmetry resulting from the analyzing power of the crystal and angle of incidence can be dramatically reduced. The preferred axis of the crystal is defined to be the direction along which linearly polarized light has the maximum quantum efficiency, taking into account both the intrinsic analyzing power and the angle of the incident light. The residual polarization is generally in different directions for the two helicity states, resulting in a charge asymmetry in the electron beam. Based on the degree of circular polarization and the sizes of the analyzing powers, the size of the charge asymmetry may be as large as one percent. However, if the component of the linear polarization along the preferred axis of the crystal is the same for both the positive helicity state and the negative helicity state there will be no charge asymmetry.

The rotatable half-wave plate is used to align the residual linear components of the polarization as described above. Figure A.2 shows the charge asymmetry as a function of the half-wave plate angle. Different sources of residual linear polarization have different angular dependences, resulting in the charge asymmetry having a dependence on the half-wave plate angle given by

$$A_I(\theta_{\lambda/2}) = \alpha * \sin(4\theta_{\lambda/2} + \phi_1) + \beta \sin(2\theta_{\lambda/2} + \phi_2) + \gamma \qquad \text{(A.5)}$$

where $\theta_{\lambda/2}$ is the orientation of the half-wave plate [83]. The first term comes from

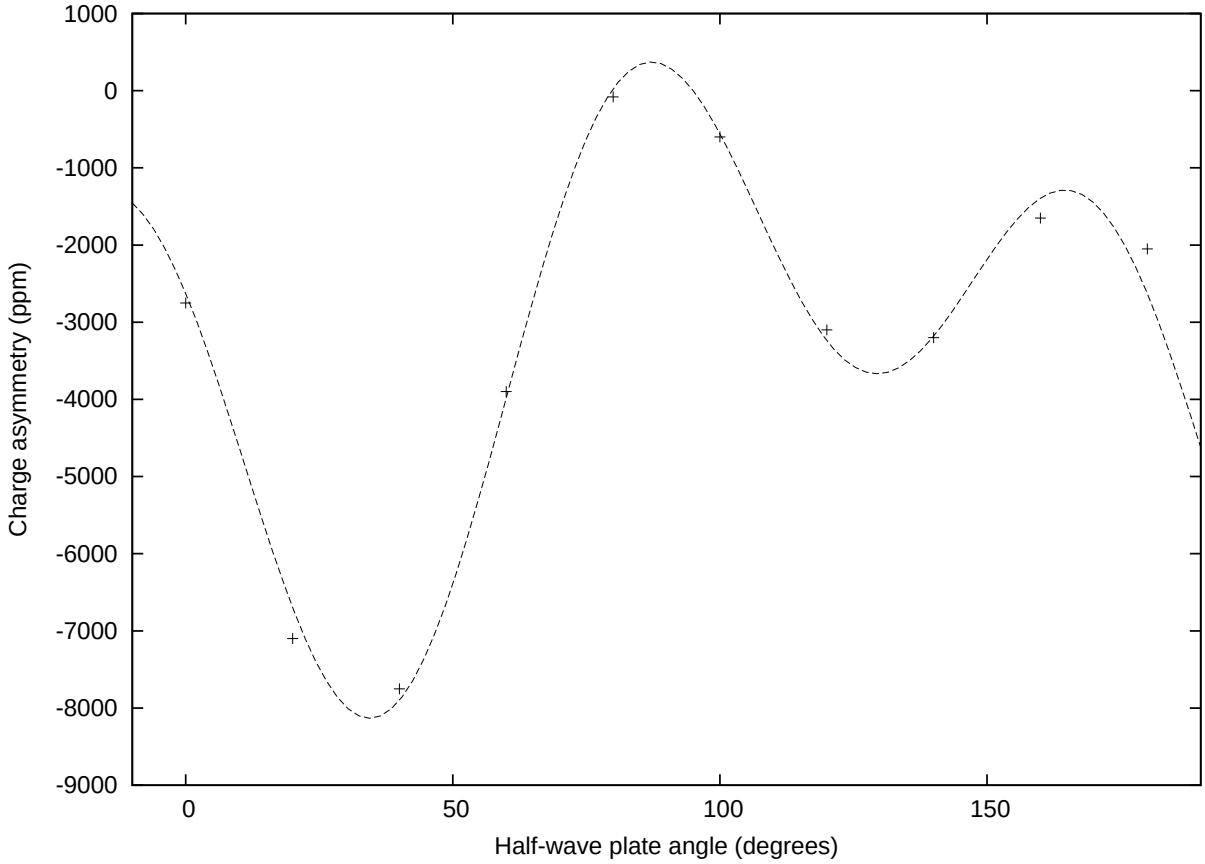

Figure A.2: Charge asymmetry as a function of half-wave plate angle. The dashed line is a fit to the points. The form of the fitting function is given by the different dependences of the sources of residual linear polarization to the half-wave plate orientation. A linear polarization component can come from residual linear polarization from the Pockels cell, a retardation error in the rotatable half-wave plate and birefringence in optical elements after the rotatable half-wave plate.

the rotation of the residual linear polarization from the HPC, and its magnitude, α, depends on the analyzing power and the amount of residual linear polarization. The angular dependence of this term can be explained by considering the symmetries of the half-wave plate and the preferred axis of the crystal. A 2π rotation of the half-wave plate rotates the direction of polarization for linearly polarized light by 4π. Because the charge only depends on the magnitude of the projection of the linear polarization along the preferred axis, a 4π rotation causes 8 zero crossings for the asymmetry. The second term arises from the retardation errors in the half-wave plate, and its magnitude, β, depends on the deviation of the retardation from π. The retardation error introduces a linearly polarized component which rotates with the half-wave plate, giving the second term a frequency half that of the first. The phases of the first two terms , ϕ_1 and ϕ_2, are related to the relative orientation of the defects and the preferred axis. Finally, birefringence in elements after the rotatable half-wave plate and retardation errors in the removable half-wave plate introduce a linearly polarized component which does not rotate. Careful adjustment of the half-wave plate allows the charge asymmetry to be reduced to approximately 200 ppm, which is within the range of the PITA feedback system.

A.4 Results

The strained GaAs source described here was capable of delivering 40 μA of electrons polarized at approximately 55%, but was not suitable for use in the 125 MeV SAMPLE experiment. The lower than expected polarization is the result of a mismatch between the particular crystal and the laser wavelength. The strained GaAs crystal used in these tests was designed for use with a longer wavelength laser; other strained crystals supplied by the same group achieved polarizations above 70%.

Despite the successful reduction of the charge asymmetry to within the range of

the PITA feedback system, the charge asymmetry was too unstable to be corrected with the feedback system. At times the charge asymmetry changed by several hundred ppm within 10 minutes. This is far too fast for the PITA feedback system to correct accurately. This instability was intermittent, and its source was not positively identified. It is suspected that one of the high-voltage power supplies use to drive the HPC was not stable at the quarter-wave voltage for the larger HPC. Given sufficient time, this problem should be relatively easy to correct.

However, there could be helicity correlated shape changes in the electron beam coming from variation in the residual polarization across the laser beam profile interacting with the preferred axis of the strained crystal. Shape changes would be difficult to correct; if they were significant, the approach of using a high divergence fiber-coupled laser with a large aperture Pockels cell would not be suitable for use in PV scattering experiments like SAMPLE.

References

[1] I. Esterman and O. Stern. *Z. Phys* **85** 17 (1933).

[2] Frisch and O. Stern. *Z. Phys* **85** 5 (1933).

[3] J. Gasser, H. Leutwyler, and M. Saino. *Phys. Lett.* **B253** 260 (1991).

[4] W. Gibbs. *Mod. Phys. Lett.* **A18** 1171 (2003).

[5] B. Filippone and X. Ji. *Adv. Nucl. Phys* **26** 1 (2001).

[6] G. Hoehler. *Nuc. Phys.* **B114** 505 (1976).

[7] D. Kaplan and A. Manohar. *Nuc. Phys.* **B310** 527 (1988).

[8] R. McKeown. *Phys. Lett.* **B219** 140 (1989).

[9] D. Beck. *Phys. Rev.* **D39** 3248 (1989).

[10] M. Pitt, E. Beise, et al. Proposal the MIT-Bates Linear Accelerator Center (1992).

[11] M. Musolf et al. *Phys. Rep.* **239** 1 (1994).

[12] G. Miller. *Phys. Rev.* **C57** 1492 (1997).

[13] D. Kaplan and A. Manohar. *Phys. Let.* **B310** 527 (1988).

[14] R. McKeown. *Phys. Let.* **B310** 140 (1989).

[15] D. Kaplan and A. Manohar. *Phys. Rev.* **D39** 3248 (1989).

[16] W. Marciano and J. Rosner. *Phys. Rev. Lett* **65** 2963 (1990).

[17] D. Kaplan and A. Manohar. *Nucl. Phys.* **B310** 527 (1988).

[18] S.-L. Zhu, S. Puglia, B. Holstein, and M. Ramsey-Musolf. *Phys. Rev.* **D62** 033008 (2000).

[19] E. Beise. Private communication (2000).

[20] I. Zeldovich. *Sov. Phys. JETP* **6** 1184 (1957).

[21] C. Wood et al. *Science* **275** 1759 (1997).

[22] C. Bouchiat and C. Piketty. *Z. Phys.* **C49** 91 (1991).

[23] V. Flambaum and I. Khriplovich. *Sov. Phys. JETP* **52** 825 (1980).

[24] C. Maekawa, J. Veiga, and U. van Kolck. *Phys. Lett.* **B488** 167 (2000).

[25] W. Koepf, E. Henley, and S. Pollock. *Phys. Lett.* **B288** 11 (1992).

[26] M. Musolf and M. Burkardt. *Zeit. Phys.* **C61** 433 (1994).

[27] M. Ramsey-Musolf and H. Ito. *Phys. Rev.* **C55** 3066 (1997).

[28] P. Geiger and N. Isgur. *Phys. Rev.* **D55** 299 (1997).

[29] P. Jain et al. *Phys. Rev.* **D37** 3252 (1988).

[30] R. Jaffe. *Phys. Lett.* **B229** 275 (1989).

[31] H. Hammer, U. Meissner, and D. Drechsel. *Phys. Lett.* **B367** 323 (1996).

[32] P. Mergell, U. Meissner, and D. Drechsel. *Nuc. Phys.* **A596** 367 (1996).

[33] H. Forkel. *Phys. Rev.* **C56** 510 (1997).

[34] S. Dong, K. Liu, and A. Williams. *Phys. Rev.* **D58** 074504 (1998).

[35] D. Leinweber and A. Thomas. *Phys. Rev.* **D62** 074505 (2000).

[36] R. Lewis, W. Wilcox, and R. Woloshyn. *Phys. Rev.* **D67** 013003 (2003).

[37] M. Malheiro and W. Melnitchouk. *Phys. Rev.* **C56** R2373 (1997).

[38] N. Park, J. Schechter, and H. Wiegel. *Phys. Rev.* **D43** 869 (1991).

[39] S. Hong and B. Park. *Nuc. Phys.* **A561** 525 (1993).

[40] S. Hong, B. Park, and D. Min. *Phys. Lett.* **B424** 229 (1997).

[41] S. Patak and S. Sahu. *Phys. Lett.* **B321** 11 (1994).

[42] H. Weigel et al. *Phys. Lett.* **B353** 20 (1995).

[43] E. Hadjimichael, G. Poulis, and T. Donnely. *Phys. Rev.* **C45** 2666 (1992).

[44] L. Diconescu, R. Schiavilla, and U. van Kolck. *Phys. Rev.* **C63** 044007 (2001).

[45] R. Schiavilla, J. Carlson, and M. Paris. *Phys. Rev.* **C67** 032501 (2003).

[46] S. Pollock. *Phys. Rev.* **D42** 3010 (1990).

[47] T. Forest. Ph.D. thesis, University of Illinois at Urbana-Champaign (1998).

[48] D. Spayde. Ph.D. thesis, University of Maryland (2001).

[49] M. Farkondeh et al. In *Applications of Accelerators in Research and Industry: Proceedings of the Fifteenth International Conference*, J. Duggan and I. Morgan, editors (1998).

[50] E. Hecht. 2nd edition (Addison-Wesley, Reading, MA, 1987).

[51] T. Averret et al. *Nucl. Inst. and Meth.* **A438** 246 (1999).

[52] D. Barkhuff et al. *Nucl. Instrum and Meth* **A450** 187 (2000).

[53] C. Møller. *Ann. Phys.* **14** 531 (1932).

[54] J. Arrington et al. *Nucl. Inst. and Meth.* **A311** 39 (1992).

[55] E. Beise et al. *Nucl. Inst. and Meth.* **A378** 383 (1996).

[56] B. Meuller. Ph.D. thesis, California Institute of Technology (1997).

[57] K. Kumar. Ph.D. thesis, Syracuse University (1990).

[58] R. Michaels. Ph.D. thesis, Yale University (1988).

[59] T. Oka. *Phys. Rev.* **D27** 523 (1982).

[60] T. Ito et al. Proposal the MIT-Bates Linear Accelerator Center (2000).

[61] T. Ito. SAMPLE, Internal Report (1999).

[62] T. Averett. SAMPLE, Internal Report (1998).

[63] E. Beise. SAMPLE, Internal Report (2003).

[64] J. Bergstrom. *Phys. Rev.* **C58** 2574 (1998).

[65] J. Bergstrom et al. *Phys. Rev.* **C57** 3203 (1998).

[66] J. Bergstrom, R. Igarashi, and J. Vogt. *Phys. Rev.* **C55** 2016 (1997).

[67] D. Drechsel et al. *Nucl. Phys.* **A645** 145–174 (1999).

[68] H. Baer, K. Crow, and P.Truol. *Adv. Nuc. Phys.* **9** (1977).

[69] J. Chen and X. Ji. *Phys. Rev. Let.* **86** 4239–4242 (2001).

[70] J. Chen and X. Ji. *Phys. Let.* **B501** 209 (2001).

[71] N. Mott. *Proc. Roy. Soc* **A135** 429 (1932).

[72] S. Wells. *Phys. Rev. Lett.* **63** 064001 (2001).

[73] R. Hasty et al. *Science* **290** 2117 (2000).

[74] T. Hemmert, U. Meissner, and S. Steininger. *Phys. Lett.* **B437** 184 (1998).

[75] T. Hemmert, B. Kubis, and U. Meissner. *Phys. Rev.* **C60** 045501 (1999).

[76] H. Hammer, M. R.-M. S. Puglia, and S. Zhu. *Phys. Lett.* **B562** 208 (2003).

[77] K. Aniol, T. A. D. Armstron, et al. *Phys. Lett.* **B509** 211 (2001).

[78] T. Ito et al. to be published.

[79] R. Alley et al. *Nucl. Instrum and Meth* **A365** 1 (1995).

[80] T. Maryuyama et al. *Phys. Rev.* **B46** 4261 (1992).

[81] H. Burkhard, H. Dinges, and E. Kuphal. *J. Appl. Phys* **A450** 655 (1982).

[82] W. Adams. "Pockels cells: Theory, test procedures, chracteristics." Clearinghouse for Federal Scientific and Technical Information (1968).

[83] B. Humensky. "Control of charge and position asymmetries in a spin-polarized electron beam for parity violation studies." Unpublished report (1999).

Vita

Richard Hasty grew up in Austin, Texas, where he attended high school at the Lyndon B. Johnson Science Academy. After graduating from high school, he studied physics at Centenary College in Shreveport, Louisiana where he received a B.S.. While an undergraduate he used the National Science Foundation's Research Experience for Undergraduates program to explore biophysics at Notre Dame and nuclear physics at the University of Illinois at Urbana-Champaign. For his graduate studies, he returned to the University of Illinois to continue his work in nuclear physics.

Publications:

Parity Violation in Elastic Electron-Proton Scattering and the Proton's Strange Magnetic Form Factor, D. Spayde *et al.*, Phys. Rev. Lett. **84**,1106 (2000)

Strange Magnetism and the Anapole Structure of the Proton, Science **290**, 2117 (2000)

Measurement of the Vector Analyzing Power in Elastic Electron-Eroton Scattering as a Probe of the Double Virtual Compton Amplitude, S. Wells *et al.*, Phys. Rev. **C63**, 064001 (2001)